

## TABLE OF CONTENTS

|   |    |
|---|----|
| INTRODUCTION .....  | 1  |
| CHAPTER 1      REVIEW OF LITERATURE.....  | 5  |
| 1.1      Aerosol particles .....  | 5  |
| 1.2      Exposure to aerosol particles and health effects .....                   | 6  |
| 1.3      Aerosol dispersion, deposition and agglomeration.....                    | 8  |
| 1.4      Ventilation systems .....  | 9  |
| 1.5      Modeling the aerosol dispersion .....                                    | 10 |
| 1.6      Code-Saturne software.....   | 14 |
| CHAPTER 2      MATHEMATICAL MODEL AND METHODOLOGY .....                           | 15 |
| 2.1      Problem definition .....   | 15 |
| 2.1.1      Duct ventilation system .....  | 15 |
| 2.1.2      Geometry and mesh .....  | 16 |
| 2.1.3      Boundary conditions .....  | 18 |
| 2.1.4      Ventilation scenarios .....  | 21 |
| 2.2      Mathematical and numerical methods .....                                 | 22 |
| 2.2.1      Air flow simulation .....  | 22 |
| 2.2.2      Particles simulation.....  | 24 |
| 2.2.2.1      Eulerian-Lagrangian approach.....                                    | 25 |
| 2.2.2.2      Equation of motion .....   | 26 |
| 2.2.3      Numerical method.....  | 30 |
| 2.3      Ventilation efficiency .....   | 31 |
| 2.4      Prediction of airflow pattern and particle deposition in 2D channel..... | 31 |
| 2.4.1      Prediction of airflow pattern in 2D channel .....                      | 32 |
| 2.4.1.1      Velocity profile .....   | 32 |
| 2.4.1.2      Entrance length .....  | 34 |
| 2.4.1.3      Friction factor .....  | 34 |
| 2.4.2      Prediction of particle deposition in 2D turbulent channel flow .....   | 35 |
| 2.4.2.1      Particle deposition velocity.....                                    | 35 |
| 2.4.2.2      Particle deposition.....   | 37 |
| 2.4.2.2.1      Gravitational Settling.....  | 37 |
| 2.4.2.2.2      Diffusional deposition.....  | 40 |
| 2.5      Summary .....  | 41 |
| CHAPTER 3      CODE-SATURNE VALIDATION.....                                       | 43 |
| 3.1      Geometry and mesh .....  | 43 |
| 3.2      Fluid and particles properties.....                                      | 46 |
| 3.3      Boundary conditions.....   | 46 |

|  |   |    |
|--|---|----|
| 3.4  | Airflow pattern.....  | 46 |
| 3.4.1  | Laminar channel flow .....  | 47 |
| 3.4.2  | Turbulent channel flow .....  | 49 |
| 3.4.3  | Turbulent 3D duct flow .....  | 53 |
| 3.5  | Particle deposition .....   | 54 |
| 3.5.1  | Particle deposition velocity.....   | 54 |
| 3.5.2  | Particle deposition .....   | 57 |
| 3.6  | Summary.....  | 58 |
| CHAPTER 4 RESULTS AND DISCUSSION.....  |   | 59 |
| 4.1  | The effect of the number of cells (mesh size) on the simulation accuracy..... | 59 |
| 4.2  | Air flow pattern in the duct ventilation system .....                         | 61 |
| 4.3  | Aerosol distribution .....  | 64 |
| 4.3.1  | Particles concentration.....  | 65 |
| 4.3.2  | Particles velocity.....   | 67 |
| 4.4  | Ventilation effectiveness .....   | 70 |
| 4.4.1  | Deposition mechanisms .....   | 74 |
| 4.4.2  | The effect of the particle diameter on the particle deposition .....          | 76 |
| 4.4.3  | The effect of the Reynolds number on the particle deposition .....            | 78 |
| 4.4.4  | The effect of the duct geometry on the particle deposition .....              | 80 |
| 4.5  | Summary.....  | 82 |
| CONCLUSION.....  |   | 83 |
| APPENDIX I FULLY DEVELOPED INLET VELOCITY PROFILES FOR 3D<br>TURBULENT DUCT FLOW ..... |   | 85 |
| LIST OF REFERENCES .....   |   | 89 |

## LIST OF TABLES

|           |   |    |
|-----------|---|----|
| Table 2.1 | Airflow mean velocity (m/s) for different Reynolds numbers and duct aspect ratios .....   | 19 |
| Table 2.2 | Inlet particle volumetric concentration ( $\text{m}^3/\text{m}^3$ ) for different Reynolds numbers and duct aspect ratios ( $d_p = 1 \text{ }\mu\text{m}$ ).....  | 20 |
| Table 2.3 | Inlet particle volumetric concentration ( $\text{m}^3/\text{m}^3$ ) for different Reynolds numbers and duct aspect ratios ( $d_p = 5 \text{ }\mu\text{m}$ ).....  | 20 |
| Table 2.4 | Inlet particle volumetric concentration ( $\text{m}^3/\text{m}^3$ ) for different Reynolds numbers and duct aspect ratios ( $d_p = 10 \text{ }\mu\text{m}$ )..... | 20 |
| Table 2.5 | Selected ventilation scenarios with different levels of duct aspect ratios, airflow Reynolds numbers and particle diameters .....                                 | 21 |
| Table 2.6 | Drag coefficient-Reynolds number relationship (Morsi and Alexander 1972).....   | 27 |
| Table 3.1 | Calculated amount of non-dimensional particle relaxation time $\tau^+$ for each particle diameter in the range of 0.1 to 10 $\mu\text{m}$ .....                   | 55 |
| Table 4.1 | Simulations for the mesh study.....   | 60 |
| Table 4.2 | Particle deposition (%) of duct with the aspect ratio of 1 .....  | 73 |
| Table 4.3 | Particle deposition (%) of duct with the aspect ratio of 2.....   | 73 |
| Table 4.4 | Particle deposition (%) of duct with the aspect ratio of 4.....   | 74 |



## LIST OF FIGURES

|            |  |    |
|------------|--|----|
| Figure 2.1 | Ventilation duct geometry with aspect ratio of 1 (a), 2 (b) and 4 (c) .....  | 17 |
| Figure 2.2 | Simplified representation of the mesh for duct ventilation with the aspect ratio of 1 .....  | 18 |
| Figure 3.1 | Schematic view of the channel geometry .....   | 45 |
| Figure 3.2 | Simplified representation of the mesh for the turbulent channel flow .....   | 45 |
| Figure 3.3 | Normalized velocity profile obtained by CFD simulation with moderately dense mesh and theoretical equation along the dimensionless channel width for laminar airflow ..... | 47 |
| Figure 3.4 | Velocity profile obtained by CFD simulation along the length of the channel at the middle of the channel for laminar airflow .....   | 48 |
| Figure 3.5 | Normalized turbulent velocity profile in the vicinity of the wall obtained by three mesh sizes.....  | 49 |
| Figure 3.6 | Normalized turbulent velocity profile obtained by this study and the results of Tian & Ahmadi in fully developed region versus the dimensionless channel width .....       | 50 |
| Figure 3.7 | Turbulent kinetic energy obtained by this study and the results of Tian & Ahmadi in fully developed region.....  | 51 |
| Figure 3.8 | Turbulence dissipation rate profiles obtained by this study and the results of Tian & Ahmadi in fully developed region .....   | 52 |
| Figure 3.9 | Turbulent velocity profile obtained by CFD simulation along the length of the channel at the middle of the channel .....   | 53 |

|             |  |    |
|-------------|--|----|
| Figure 3.10 | Dimensionless turbulent velocity profile obtained by this study and the results of Yao et al. versus the dimensionless duct width.....   | 54 |
| Figure 3.11 | Non-dimensional particle deposition velocity versus non-dimensional particle relaxation time for particles with a diameter of 0.1 to 10 $\mu\text{m}$ .....  | 56 |
| Figure 3.12 | Percentage of the injected particles deposited on the channel surfaces versus the particle diameter while neglecting the Langvin effect ..   | 57 |
| Figure 4.1  | Particle deposition versus the dimensionless duct length for three different mesh size (duct aspect ratio = 1, $\text{Re} = 7.36 \times 10^3$ and $d_p = 10 \mu\text{m}$ ) .....   | 61 |
| Figure 4.2  | Fully developed airflow velocity profiles for the Reynolds number of $7.36 \times 10^3$ presented as a surface plot (a) and for the Reynolds numbers of $7.36 \times 10^3$ (b), $15.4 \times 10^4$ (c) and $36.3 \times 10^4$ (d) presented as contour plots for the duct with the aspect ratio of 1 ..... | 62 |
| Figure 4.3  | Fully developed airflow velocity profiles for the Reynolds number of $7.36 \times 10^3$ presented as a surface plot (a) and for the Reynolds numbers of $7.36 \times 10^3$ (b), $15.4 \times 10^4$ (c) and $36.3 \times 10^4$ (d) presented as contour plots for the duct with the aspect ratio of 2.....  | 63 |
| Figure 4.4  | Fully developed airflow velocity profiles for the Reynolds number of $7.36 \times 10^3$ presented as a surface plot (a) and for the Reynolds numbers of $7.36 \times 10^3$ (b), $15.4 \times 10^4$ (c) and $36.3 \times 10^4$ (d) presented as contour plots for the duct with the aspect ratio of 4.....  | 64 |
| Figure 4.5  | Particle volume concentrations at a cross section of the duct with the aspect ratio of 1 and Reynolds number of $7.36 \times 10^3$ for particle diameter of 1 $\mu\text{m}$ (a), 5 $\mu\text{m}$ (b) and 10 $\mu\text{m}$ (c) .....  | 66 |
| Figure 4.6  | Particle volume concentrations at a cross section of the duct with the aspect ratio of 2 and Reynolds number of $7.36 \times 10^3$ for particle diameter of 1 $\mu\text{m}$ (a), 5 $\mu\text{m}$ (b) and 10 $\mu\text{m}$ (c) .....  | 66 |

|             |   |    |
|-------------|---|----|
| Figure 4.7  | Particle volume concentrations at a cross section of the duct with the aspect ratio of 4 and Reynolds number of $7.36 \times 10^3$ for particle diameter of 1 $\mu\text{m}$ (a), 5 $\mu\text{m}$ (b) and 10 $\mu\text{m}$ (c).....            | 67 |
| Figure 4.8  | Particle velocity profile at a representative cross section of the duct with the aspect ratio of 1 and Reynolds number of $7.36 \times 10^3$ for particle diameter of 1 $\mu\text{m}$ (a), 5 $\mu\text{m}$ (b) and 10 $\mu\text{m}$ (c) ..... | 69 |
| Figure 4.9  | Particle velocity profile at a representative cross section of the duct with the aspect ratio of 2 and Reynolds number of $7.36 \times 10^3$ for particle diameter of 1 $\mu\text{m}$ (a), 5 $\mu\text{m}$ (b) and 10 $\mu\text{m}$ (c).....  | 69 |
| Figure 4.10 | Particle velocity profile at a representative cross section of the duct with the aspect ratio of 4 and Reynolds number of $7.36 \times 10^3$ for particle diameter of 1 $\mu\text{m}$ (a), 5 $\mu\text{m}$ (b) and 10 $\mu\text{m}$ (c).....  | 70 |
| Figure 4.11 | Particle deposition versus the dimensionless duct length, $\text{Re} = 7.36 \times 10^3$ (duct aspect ratio = 1) .....  | 71 |
| Figure 4.12 | Particle deposition versus the dimensionless duct length, $\text{Re} = 15.4 \times 10^4$ (duct aspect ratio = 1) .....  | 72 |
| Figure 4.13 | Particle deposition versus the dimensionless duct length, $\text{Re} = 36.3 \times 10^4$ (duct aspect ratio = 1) .....  | 72 |
| Figure 4.14 | Percentage of particle deposition versus the Reynolds number for particle diameter of 1 $\mu\text{m}$ (duct aspect ratio = 1).....  | 75 |
| Figure 4.15 | Percentage of particle deposition versus the Reynolds number for particle diameter of 5 $\mu\text{m}$ (duct aspect ratio = 1).....  | 75 |
| Figure 4.16 | Percentage of particle deposition versus the Reynolds number for particle diameter of 10 $\mu\text{m}$ (duct aspect ratio = 1).....   | 76 |

|             |   |    |
|-------------|---|----|
| Figure 4.17 | Particle deposition at the outlet versus the particle diameter<br>for different ducts ( $Re = 7.36 \times 10^3$ ).....              | 77 |
| Figure 4.18 | Particle deposition at the outlet versus the particle diameter<br>for different ducts ( $Re = 15.4 \times 10^4$ ).....              | 78 |
| Figure 4.19 | Particle deposition at the outlet versus the particle diameter<br>for different ducts ( $Re = 36.3 \times 10^4$ ).....              | 78 |
| Figure 4.20 | Particle deposition at the outlet versus the Reynolds number<br>for different ducts ( $d_p = 1 \mu m$ ).....                        | 79 |
| Figure 4.21 | Particle deposition at the outlet versus the Reynolds number<br>for different ducts ( $d_p = 5 \mu m$ ).....                        | 79 |
| Figure 4.22 | Particle deposition at the outlet versus the Reynolds number<br>for different ducts ( $d_p = 10 \mu m$ ).....                       | 80 |
| Figure 4.23 | Particle deposition at the outlet versus the duct aspect ratio<br>for different particle diameter ( $Re = 7.36 \times 10^3$ ) ..... | 81 |
| Figure 4.24 | Particle deposition at the outlet versus the duct aspect ratio<br>for different particle diameter ( $Re = 15.4 \times 10^4$ ) ..... | 81 |
| Figure 4.25 | Particle deposition at the outlet versus the duct aspect ratio<br>for different particle diameter ( $Re = 36.3 \times 10^4$ ) ..... | 82 |



## LIST OF ABBREVIATIONS AND ACRONYMS

|                             |   |   |
|-----------------------------|---|---|
| $A$                         | surface area of the duct cross section  | $m^2$   |
| $a_1, a_2 \text{ and } a_3$ | constants in the drag coefficient equation (Equation (2.18))                            |   |
| $a_p$                       | acceleration of the particle  | $m.s^{-2}$  |
| $a_a$                       | acceleration of the air   | $m.s^{-2}$  |
| $C_c$                       | Cunningham slip correction factor   |   |
| $C_D$                       | drag coefficient  |   |
| $C_f$                       | friction coefficient  |   |
| $\bar{C}_{x=L}$             | averaged volumetric concentration of the particles at x equal to L meter from the inlet | $m^3 \text{ particle.}$<br>$m^{-3} \text{ fluid}$ |
| $\bar{C}_{x=1}$             | averaged volumetric concentration of the particles at x equal to 1 meter from the inlet | $m^3 \text{ particle.}$<br>$m^{-3} \text{ fluid}$ |
| $D$                         | particle diffusion coefficient  | $m^2.s^{-1}$                                      |
| $D_H$                       | Hydraulic diameter  | $m$   |
| $D$                         | inside diameter of the tube   | $m$   |
| $d_p$                       | particle diameter   | $m$   |
| $d_{ij}$                    | deformation tensor  |   |
| $F_{ai}$                    | additional forces applied on the particle   | $N$   |
| $F_{Ba}$                    | Basset force  | $N$   |
| $F_{bi}$                    | Brownian force  | $N$   |
| $F_{drag}$                  | drag force  | $N$   |
| $F_i$                       | external forces applied on the particle in $i$ direction                                | $N$   |
| $F_m$                       | virtual mass force  | $N$   |

|           |  |                            |
|-----------|--|----------------------------|
| $F_P$     | pressure gradient force                                      | N                          |
| $F_{si}$  | Saffman's lift force   | N                          |
| $G_i$     | zero-mean, unit-variance independent Gaussian random numbers |                            |
| $g_i$     | gravitational acceleration in the $i$ direction              | $\text{m.s}^{-2}$          |
| $g_x$     | gravitational acceleration in x direction                    | $\text{m.s}^{-2}$          |
| $g_y$     | gravitational acceleration in y direction                    | $\text{m.s}^{-2}$          |
| $g_z$     | gravitational acceleration in z direction                    | $\text{m.s}^{-2}$          |
| $g^+$     | non-dimensional gravity                                      |                            |
| $H$       | duct height (in z direction)                                 | m                          |
| $K$       | turbulent kinetic energy                                     | J/kg                       |
| $Kn$      | Knudsen number   |                            |
| $L$       | duct length (in x direction)                                 | m                          |
| $L_e$     | entrance length  | m                          |
| MSE       | Mean Squared Error   |                            |
| $P$       | perimeter of the duct cross section                          | m                          |
| $P$       | fluid pressure   | Pa                         |
| $\bar{p}$ | mean value of fluid pressure in turbulent flow               | Pa                         |
| $\dot{p}$ | turbulent flow fluctuations for fluid pressure               | Pa                         |
| $Q$       | volumetric fluid flow  | $\text{m}^3.\text{s}^{-1}$ |
| $Re_{DH}$ | Reynolds number based on hydraulic diameter                  |                            |
| $Re_p$    | particle Reynolds number                                     |                            |
| $S_0$     | spectral intensity   |                            |

|                  |   |            |
|------------------|---|------------|
| $Sc$             | Schmidt number  |            |
| $Sh$             | Sherwood number   |            |
| $T$              | fluid absolute temperature                                    | K          |
| $T$              | Time  | s          |
| $U$              | local fluid velocity in x direction                           | $m.s^{-1}$ |
| $\bar{u}$        | mean value of fluid velocity in x direction in turbulent flow | $m.s^{-1}$ |
| $\acute{u}$      | turbulent flow fluctuations for fluid velocity in x direction | $m.s^{-1}$ |
| $U_0$            | average fluid velocity in duct in x direction                 | $m.s^{-1}$ |
| $u^*$            | friction velocity   | $m.s^{-1}$ |
| $u_d^+$          | non-dimensional deposition velocity                           |            |
| $u_{deposition}$ | deposition velocity of particles                              | $m.s^{-1}$ |
| $u_i$            | fluid velocity in $i$ direction                               | $m.s^{-1}$ |
| $u_{pi}$         | particle velocity in $i$ direction                            | $m.s^{-1}$ |
| $V$              | local fluid velocity in y direction                           | $m.s^{-1}$ |
| $\bar{v}$        | mean value of fluid velocity in y direction in turbulent flow | $m.s^{-1}$ |
| $\acute{v}$      | turbulent flow fluctuations for fluid velocity in x direction | $m.s^{-1}$ |
| $V_{diff}$       | diffusive deposition velocity                                 | $m.s^{-1}$ |
| $V_{ts}$         | terminal settling velocity                                    | $m.s^{-1}$ |
| $W$              | duct width (in y direction)                                   | m          |
| $W$              | local fluid velocity in z direction                           | $m.s^{-1}$ |
| $\bar{w}$        | mean value of fluid velocity in z direction in turbulent flow | $m.s^{-1}$ |
| $\acute{w}$      | turbulent flow fluctuations for fluid velocity in x direction | $m.s^{-1}$ |
| $X$              | distance in flow direction                                    | m          |

|       |                                    |   |
|-------|------------------------------------|---|
| $Y$   | distance in gravity direction      | M |
| $y^+$ | dimensionless wall distance        |   |
| $Z$   | gravitational deposition parameter |   |
| $Z$   | distance in lateral direction      | M |

### Greek letters

|               |  |   |
|---------------|--|---|
| $\Delta$      | Laplace operator = $\frac{\partial^2}{\partial x^2} + \frac{\partial^2}{\partial y^2} + \frac{\partial^2}{\partial z^2}$ |   |
| $\Delta t$    | time step  | S                                       |
| $\Lambda$     | Darcy friction factor at the wall  |   |
| $A$           | duct aspect ratio ( $W/H$ )  |   |
| $\varepsilon$ | turbulence dissipation rate  | $\text{m}^2.\text{s}^{-3}$              |
| $\eta_{diff}$ | transport efficiency for diffusive particle deposition   |   |
| $\eta_{duct}$ | duct efficiency  |   |
| $\eta_{grav}$ | transport efficiency for gravitational deposition  |   |
| $\lambda$     | mean free path   | M                                       |
| $\lambda_r$   | mean free path in air at $T = 293\text{ K}$ and atmospheric pressure   | M                                       |
| $\mu$         | fluid viscosity  | $\text{kg}.\text{m}^{-1}.\text{s}^{-1}$ |
| $N$           | fluid kinematic viscosity  | $\text{m}^2.\text{s}^{-1}$              |
| $P$           | fluid density  | $\text{kg}.\text{m}^{-3}$               |
| $\rho_p$      | particle density   | $\text{kg}.\text{m}^{-3}$               |
| $\Sigma$      | Boltzmann constant ( $1.38 \times 10^{-23}\text{ N. m/ K}$ )   | $\text{N}.\text{m}.\text{K}^{-1}$       |
| $\tau^+$      | non-dimensional particle relaxation time   |   |

|          |                          |                                     |
|----------|--------------------------|-------------------------------------|
| $\tau_p$ | particle relaxation time | s                                   |
| $\tau_w$ | wall shear stress        | kg.m <sup>-1</sup> .s <sup>-2</sup> |



## INTRODUCTION

Many industrial processes such as wood cutting, welding, grinding or polishing generate dust, fume and fibres. These airborne particulates constitute a risk of health issue for workers' exposed to particulates (Hinds 1999). The study of airborne particles aerodynamic behaviour is of particular interest considering the growing concern about the inhalation of aerosol particles and its potential health effects. Studies have focused in recent years on airborne particles motion and their deposition on surfaces (Li and Ahmadi 1992). The level of worker exposure to these aerosol particles could be estimated if models are developed to predict the concentration of airborne particles and the main phenomena affecting their aerodynamic behaviour. Knowing the spatial and temporal behaviour of particles after their release can help in the design of appropriate engineering control system and personal protection equipment (PPE) for the workers. Numerical simulation of airborne particles behaviour is attractive because it gives essential information to develop a more effective control system (Zhang and Li 2008).

Most often, the control system is a local extraction system that removes the contaminated air from the room. The contaminated air is transported to a filtration system through a ventilation duct. In the filtration system, the contamination is removed and the "clean" air is released in the outdoor environment or recirculated in the building (Zhang and Li 2008). As contaminated air passes through the ventilation duct, some particles might deposit on the duct surfaces. Accumulation of particles in the ventilation duct reduces the particle removal efficiency (defined as the ratio of the particles that leave the duct over total particles that enter the duct). Dirty ducts are a good environment for the development of bacteria, dust mites, allergens and moulds. Also, it increases the need for cleaning the ventilation system and can be a potential source of indoor air pollution during the cleaning process (Laatikainen, Pasanen et al. 1992). Therefore, the design of the ventilation system needs to be adjusted to reduce the particle accumulation in the ventilation duct. The aspect ratios of the rectangular duct, the airflow rates, the concentration, size and source of aerosol particles affect the efficiency of the duct ventilation (Farrance and Wilkinson 1990). The knowledge of the

particle deposition on ventilation duct surfaces also helps in determining how regular the ventilation system should be cleaned (Turiel 1985). This master's thesis therefore concentrates on the particles behaviour in the rectangular ventilation ducts. Specifically, the deposition of aerosol particles in the duct flows is studied.

Experimental studies and computational fluid dynamics (CFD) can be used to study the aerodynamic behaviour of aerosol particles and their dispersion (Li and Ahmadi 1992, Tian and Ahmadi 2007, Zhang and Li 2008, Zhao, Chen et al. 2009). CFD simulations are less expensive in both terms of money and time compared to the experimental measurements. CFD can also decrease the costs by reducing the number of experiments required for the design of the system and may provide information that is difficult to obtain through physical experiments. However, CFD simulations of aerosol flow is challenging because of the difficulties in describing the turbulent flow and particle-eddy interaction and validating the simulation results with experimental data (Tang and Guo 2011).

The main goal of this project is to investigate the aerosol particles behaviour and their deposition on the surfaces of ventilation ducts with different aspect ratios considering various Reynolds numbers and particle diameters in order to select the most effective ventilation duct system.

To achieve this goal, the project specifically aimed to:

- 1) Propose a geometrical and a mathematical model together with a numerical method to simulate the airflow and aerosol particle behaviour in a 3D duct flow;
- 2) Validate the 2D simulation results for laminar and turbulent channel flows using empirical correlations and numerical simulations available in the literature;
- 3) For 3D duct flows, investigate the particle deposition on the solid surfaces of the duct and suggest an appropriate duct aspect ratio and Reynolds number to have a more efficient ventilation duct.



To reach the first objective, a literature review was performed to get the information on the available models for the simulation of particle motion and deposition in 3D duct flows. The selected model was then applied to a 2D channel flow for both laminar and turbulent flow regimes. The simulated airflow velocity profile, the Darcy friction factor, the entry length, the particle deposition velocity and the channel efficiency for aerosol particle removal are the quantities used for validation. After validation of the mathematical model for 2D channel flow, the model was used for the simulation of particles dispersion and deposition in a 3D turbulent duct flow. Aerosol particles were injected into the 3D turbulent duct flow. The particle deposition on the solid surfaces of the duct and the efficiency of the duct for different ventilation scenarios with three different aspect ratios, three different Reynolds numbers and three different particle diameters were investigated. The simulation results were then compared to propose an appropriate duct aspect ratio, Reynolds number and particle diameter for an efficient ventilation system.

Chapter 1 is devoted to the literature review of the previous relevant studies. This chapter begins by a discussion of aerosol particles, their health effects and the consequences of exposure to these particles. Then, the dispersion of aerosol particles and the phenomena that affect their physical and chemical properties are presented. After that, the ventilation systems and the strategies used to improve indoor air quality are described. Finally, the methods commonly used for simulating the particle dispersion and the results of some investigations about particle deposition in turbulent flow in order to improve the effectiveness of ventilations such as ducts are mentioned.

In chapter 2, the mathematical model and the numerical method that are used to model the duct flows are described. Then, the geometry of the duct ventilation system, the airflow and particles properties and the boundary conditions used in this work are presented.

Chapter 3 is devoted to the validation of the model and the numerical method that we have used for our simulation. In this chapter, the CFD simulation results of our work are validated for 2D laminar and turbulent channel flow by comparison with empirical correlations and

numerical simulations from the literature for the velocity profile, the Darcy friction factor and the entry length. Then, the results of particle deposition in 2D turbulent channel flows are validated with results from empirical correlations available in literature.

Chapter 4 presents the results of particle deposition in 3D turbulent duct flows in order to find the more efficient duct ventilation system in removing the contaminants. In this chapter first, the results of different mesh sizes are presented to choose the appropriate mesh size. Then, the airflow velocity profiles are shown. Thereafter, the particle concentration and particle velocity distributions in the duct cross section are described to better understand how particles behave in the duct system. Then, the results of particle deposition for different ventilation scenarios are presented and discussed to find the most effective ventilation scenario.

## **CHAPTER 1**

### **REVIEW OF LITERATURE**

The main objective of this chapter is to review the relevant previous works on aerosol dispersion and deposition in ventilation systems. With the literatures, we can better define the problem and the geometrical model. These literatures help us to select an appropriate mathematical model together with a numerical method to find the most effective ventilation scenario for the defined ventilation duct. This chapter begins by a presentation of the aerosol particles, an overview of their health effects and the consequences of exposure to these particles. Then the dispersion of aerosol particles and the phenomena that affect their physical and chemical properties during the dispersion are presented. Thereafter, the ventilation systems and the strategies used to improve indoor air quality are described. In the next section, the methods for simulating the particle dispersion and the results of some investigations about particle deposition in turbulent duct flows in order to improve the effectiveness of duct ventilations are mentioned. Finally, Code-Saturne software, which is used in this study is described.

#### **1.1 Aerosol particles**

Aerosols are two-phase systems containing a suspended solid or liquid phase in a gaseous medium. Aerosols are formed by two ways: decomposition of solids or liquids into finer particles and conversion of gases to particles (Kulkarni, Baron et al. 2011). As examples for aerosol particles, we could refer to atmospheric cloud droplets, smoke from fossil-fuel power generation, cigarette smoke, airborne particles from volcanic eruptions, salt particles from ocean and welding fume (Kulkarni, Baron et al. 2011). Aerosol particles can be subdivided in different categories according to the physical form of the particles and their generation method. In some cases, aerosols may be stable for a year but they usually are stable for a few seconds (Hinds 1999). The properties and behaviour of aerosol particles is affected by their diameter, concentration and density. Liquid droplets are almost in a spherical shape, but most of the solid aerosol particles have complex shapes. However, the particles are considered

spherical to ease the study of their properties. For different shapes of solid particles, an equivalent diameter is used to characterize their size. The equivalent diameter of a non-spherical particle is defined as a spherical particle diameter with the same value of some physical properties as non-spherical particle (Hinds 1999). The sizes of aerosols particles are in the range of about 0.002 to more than 100  $\mu\text{m}$ . Particles with the diameter less than 1  $\mu\text{m}$  are in the range of sub-micrometer aerosols and particles with sizes of 1 to 100  $\mu\text{m}$  are in the range of micrometer aerosols. For example, smokes and fumes are in the sub-micrometer range and pollen and dusts are in the micrometer range (Hinds 1999).

To measure the concentration of aerosol particles, one common way is to use the particle mass concentration. The particle mass concentration is defined as the mass of aerosol particles per unit of volume. The units for particle mass concentration are  $\text{g}/\text{m}^3$ ,  $\text{mg}/\text{m}^3$  or  $\mu\text{g}/\text{m}^3$ . The particle number concentration is another way to measure the aerosol particles concentration. The particle number concentration is defined as the number of aerosol particles per unit volume. The common units are  $\text{number}/\text{m}^3$  or  $\text{number}/\text{cm}^3$  (Hinds 1999).

In the atmosphere, there are two kinds of aerosol particles: aerosols that exist in the absence of any human activities (natural background aerosols) and urban aerosols that are formed by anthropogenic sources (formed by human activities).

## **1.2 Exposure to aerosol particles and health effects**

The importance of atmospheric aerosol particles in environmental policy and associated problems in air quality and climate change policies have caused researchers to pay more attention to the study of aerosol particle properties (Fuzzi, Baltensperger et al. 2015). By increasing the usage of aerosol particles in industrial applications, the number of workers who are exposed to aerosol particles increases. In the university sector and in emerging aerosol particle companies, the number of workers who may be exposed to these particles may be as high as 2000 in the UK (Aitken, Creely et al. 2004). In addition, it has been

reported that more than 1,000,000 workers may be exposed to aerosol particles in the UK via incidental production in processes such as welding and refining (Aitken, Creely et al. 2004).

Both indoor and outdoor exposure to aerosol particles can strongly affect people's health. However, the indoor exposure could be more important because people spend 90% of their time indoors. If indoor aerosol sources create high indoor particle concentration, the contaminants may diffuse outdoor and cause an outdoor exposure as well (Husseina, Wierzbickac et al. 2015).

Exposure to aerosol particles could occur by inhalation, dermal and ingestion routes. Inhalation is the principal route of exposure to aerosol particles in an occupational setting. In the inhalation case, there are four metrics to measure the dose of aerosol particles in the lung: particle mass concentration, particle number concentration, the shape and the surface area of the particles that are deposited. Among these four exposure metrics, surface area seems to be the best metric for the assessment of inhalation exposure to nanoparticles (Tran, Buchanan et al. 2000, Faux, Tran et al. 2003). Dermal exposure has harmful effects that may occur locally within the skin or by absorbing the material through the skin and spreading with the bloodstream. As examples of materials that cause dermal exposure, we can mention carbon tetrachloride as a solvent and methyl parathion as a pesticide (Aitken, Creely et al. 2004). Significant efforts have been done to extend quantitative methods for monitoring skin exposure. In all these techniques, the mass of material that is deposited onto the skin is measured (Schneider, Cherrie et al. 2000). There are very little study and investigation on the ingestion route. One of the materials that cause ingestion exposures is lead. Lead paint removal activity has the capability to generate high ingestion exposures. This exposure is produced by hand-mouth contact and food contamination in the workplace. For example, the workers who are involved in the supply and removal of scaffolding have high levels of lead in their blood. This is due to hand contamination and subsequent ingestion (Sen, Wolfson et al. 2002).

### **1.3 Aerosol dispersion, deposition and agglomeration**

If there is a leak in the aerosol particles production equipment, large amount of particles can be emitted into a workplace environment. As these particles travel through the ambient air, physical and chemical changes will occur due to phenomena such as coagulation, agglomeration and diffusion. In addition, some particles may deposit on the surfaces via different mechanisms (Stanley 2010). By knowing the correct size and concentration of aerosol particles at distances from the leak, the worker exposures can be determined and an appropriate protection can be developed. In addition, optimal design of ventilation systems requires the knowledge of the particles behaviour in the workplace and the ventilation ducts. All these can be achieved by numerical simulation of aerosol particles behaviour and dispersion in the workplace, considering the effective phenomena like Brownian diffusion, advection, coagulation and deposition of particles (Stanley 2010).

If there is a gradient in the particle concentration between two regions in the medium, particles tend to move from the high concentration region to the low concentration region. This displacement is due to the Brownian diffusion. Advection is a transport mechanism in which particles move with the mean fluid flow (Kulkarni, Baron et al. 2011). Brownian motion of aerosol particles (the random motion of particles suspended in a fluid, a liquid or a gas, resulting from their collision with the quick atoms or molecules in the gas or liquid (Mörsters and Peres 2010)) and external forces (such as gravity, electrical forces and aerodynamic effects) lead to plenty of collisions between particles. These collisions cause particles to agglomerate or coagulate and then the particles diameter increases. The speed of agglomeration depends on particle number concentration and particle mobility (Friedlander and Pui 2004). Deposition of particles is the process in which particles deposit on the solid surfaces. Then the particle concentration decreases in the air and increases on the solid surfaces. For particles with a diameter less than 0.5  $\mu\text{m}$ , diffusion is the predominant deposition mechanisms. However, large particles deposit quickly due to the effect of the gravity (Hinds 1999).

## 1.4 Ventilation systems

One way to prevent or mitigate the effects of aerosol particle dispersion in workplace is the use of ventilation systems, which remove the contaminated air from the environment. Ventilation systems also replace the contaminated air with fresh air to improve the indoor air quality and provide thermal comfort. Fresh air enters the room through the ventilation systems and dilutes the contaminated indoor air while contaminated air is removed from indoors. The main goal of the ventilation systems is to provide a high indoor air quality (clean and unpolluted air) for breathing. To ventilate the buildings, three methods can be used: natural, mechanical and hybrid (mixed mode) ventilation. In natural ventilation systems, fresh air enters the room because of the natural forces like wind and thermal buoyancy force (caused due to difference in indoor and outdoor air density). Then, this method of ventilation depends on the climate and building design. The disadvantage of the natural ventilation system is difficult control of the outdoor airflow which enters the room because no fan operates the system (Lakhout 2011).

Mechanical ventilation systems have different elements: one or more fans, a distribution network, dampers, heating and cooling coils and filters. Mechanical ventilation systems consume energy (Lakhout 2011). In mechanical ventilation systems, the fans can be installed in walls, or windows, in air ducts to supply the air into the room or exhaust air from the room. There are three main strategies for mechanical ventilation:

- mixing ventilation;
- displacement ventilation;
- laminar flow ventilation.

In mixing ventilation, fresh air enters the room and dilutes the contaminated indoor air. The fresh air enters with high speed and then mixes with the air inside the room to achieve a uniform concentration of contaminants in indoor air (Méndez, Jose et al. 2008, Lakhout 2011). In displacement ventilation, the air with lower temperature (14-16 °C) than the room air temperature and low speed is introduced near the floor. With the available heat sources,

the air temperature increases and then goes up while it is carrying the contaminants toward the ceiling. With this kind of ventilation, the concentration of contaminants in the bottom side of the room is usually lower than the upper side where the air exits the room. In displacement ventilation, the supply airflow and its temperature should be controlled to have efficient ventilation. Compared to the mixing ventilation, less energy is required in the displacement ventilation (Lakhout 2011). In laminar flow ventilation, the air blown from the inlet goes directly toward the exhaust. The contaminants will be removed directly if the supply and exhaust are in the opposite sides of the room. The laminar flow ventilation is very effective to remove the contaminant from the room but it needs significant blowing surfaces and blowing airflow (Lakhout 2011).

In hybrid ventilation, the natural forces produce the ventilation flow rate. But when the flow rate is very low, the mechanical ventilation is also used to increase the ventilation flow rate. Then when the natural ventilation is not suitable alone, the strategy of hybrid ventilation is to use the exhaust fans where the room air can be exhausted directly to the outdoor environment (Lakhout 2011).

In industrial applications, mechanical ventilation is usually the choice to ensure efficient ventilation and minimized health risks. The contaminated air is removed from the room through a ventilation duct and is then passed through a filtration system to eliminate the contamination. Optimal design of the ventilation duct (duct dimensions, airflow rate, etc.) is essential to control the deposition of the particles (contaminants) in the duct since accumulation of the particles in the ventilation duct reduces the particle removal efficiency and increases the need for cleaning the duct.

## **1.5 Modeling the aerosol dispersion**

Channel flows are present in various applications such as ventilations systems, pneumatic transport, gas and compressed air line, aerosol sampling, filtration and separation (Zhang and Li 2008). Thus, channel flows have been studied extensively. There are two methods to



investigate particle dispersion and deposition in a channel flow: experimental studies and computational fluid dynamics (CFD) model. Compared to experimental studies, CFD studies have the advantage that they do not cause any health risk and they are less expensive. CFD models can provide detailed spatial distribution of air velocity, pressure and contaminant concentration by solving simultaneously the conservation equations of mass, momentum and energy (Zhao, Chen et al. 2009). There are two approaches to solve the two-phase flow problems: Eulerian-Eulerian approach and Eulerian-Lagrangian approach. In both approaches, the gas phase is considered as a continuum phase and Eulerian description is the best way to model the gas phase. In this way, the continuum phase is simulated using different numerical methods such as finite volume, finite element and finite difference that solve the governing equations. The gas phase is modeled by solving Reynolds averaged Navier-Stokes (RANS) equations (Sivier, Loth et al. 2005, Beauchêne, Laudinet et al. 2011). In the Eulerian-Eulerian approach, the particle phase is also considered as a continuum phase similar to the gas phase and conservation equations are developed based on the Eulerian approach. On the other side, in the Eulerian-Lagrangian approach, particles are considered as a discrete phase and are tracked individually. The Lagrangian approach calculates the particle concentration and deposition by studying the statistics of particle trajectories (Zhang and Chen 2007). In this method, individual particles are simulated based on a Probability Distribution Function (PDF) approach. The fluid flow is first modeled with the Eulerian approach. Then, particles are injected into the frozen flow field and particle trajectories are tracked. This one way coupling simulation is valid if the mass concentration of particles is small. With this assumption, particles do not affect the momentum of the fluid but the fluid influences the particle momentum (Sivier, Loth et al. 2005, Dorogan 2012). By integrating the motion equation on the particle in x, y and z coordinates, the particle motion equations can be solved in each direction.

The research objective and the characteristics of a certain problem determine which approach is more appropriate. For example, Murakami et al., (1992); Zhao et al., (2004); Zhao et al., (2005) chose the Eulerian-Eulerian approach which is appropriate to study the concentration distributions of particles in indoor environments (Murakami, Kato et al. 1992, Zhao, Zhang

et al. 2004, Zhao, Zhang et al. 2005). On the other hand, Lu et al., (1996) used the Eulerian-Lagrangian approach to analyze the aerosol particle concentration and airflow patterns in a ventilated two-zone chamber (Lu, Howarth et al. 1996). Zhang and Chen, (2004) used the Eulerian-Lagrangian approach to predict the temporal development of the mean concentration in a room ventilated by an under floor air distribution system (Zhang and Chen 2004). Béghein et al., (2005) used large eddy simulation (LES) to predict three-dimensional and transient turbulent flows and a Lagrangian model to compute particle trajectories in a room (Béghein, Jiang et al. 2005).

To simulate the particle deposition in a channel flow, McLaughlin (1989) used the Eulerian-Lagrangian approach to study the particle deposition in a vertical turbulent channel flow with the dimensionless relaxation time,  $\tau_p$  (the relaxation time of the particle is the time for a particle to reach 63% of its final velocity when an external force like the gravity exerts on a particle (Kulkarni, Baron et al. 2011)), between 2 to 4. In this simulation, the flow field was generated by direct numerical simulation (DNS) and the Reynolds number of the flow was 4000 (McLaughlin 1989). Brooke et al. (1992, 1994) used this method to track the particle trajectories in a DNS-generated flow field in vertical channel flow. They considered only the drag force in the diffusion-impaction regime (particle dimensionless relaxation time is between 1 and 10 and the interactions between the particles and turbulent eddies increase the net particle flux toward the wall) (Brooke, Kontomaris et al. 1992, Brooke, Hanratty et al. 1994, Chiou, Chiu et al. 2001). Wang and Squires (1996a,b) demonstrated the feasibility of particle deposition simulation in a channel flow using Eulerian-Lagrangian method where the flow field was generated by large eddy simulation (LES) (Wang and Squires 1996a, Wang and Squires 1996b). Uijttewaai and Oliemans (1996) used this approach to simulate particle deposition in the inertia-moderated regime in a vertical cylindrical tube. In this study, the flow field is generated by both large eddy simulation and direct numerical simulation (Uijttewaai and Oliemans 1996). Zhang and Ahmadi (2000) also used Eulerian-Lagrangian method to investigate the differences in the deposition of particles between the downward and upward vertical flow by changing the lift force. Results of these Lagrangian simulations were in good agreement with the experimental results (Zhang and Ahmadi 2000). Zhang and

Li (2008) studied the dimensionless deposition velocities of particles ranging from 10 to 200  $\mu\text{m}$  using the Lagrangian approach in the horizontal turbulent duct flow with a fully developed velocity profiles based on RANS (Reynolds-averaged Navier–Stokes) equations to predict the particle deposition (Zhang and Li 2008). Wood (1981) studied the particle deposition on both smooth and rough surfaces in turbulent duct flows. He indicated that, the deposition of particles is extremely sensitive to the surface roughness (Wood 1981). Ounis and Ahmadi (1993) studied the diffusion process of submicron particles and also the effects of particle size on particle dispersion in a simulated turbulent channel flow (Ounis, Ahmadi et al. 1993).

An experimental study was done to determine the smoke particle behaviour considering four Reynolds numbers in the range of  $7.36 \times 10^3$  and  $36.3 \times 10^4$  for ducts of various aspect ratios (Cheong 1997). He found that at a given Reynolds number, the deposition of smoke particles is decreases as the duct aspect ratio increases (Cheong 1997). Zhang and Li (Zhang and Li 2008) simulated the deposition of particles ranging from 10 to 200  $\mu\text{m}$  in a horizontal turbulent duct flow using the Lagrangian approach. They considered fully developed velocity profiles based on RANS equations at three Reynolds numbers of  $2.0 \times 10^4$ ,  $3.3 \times 10^4$  and  $4.5 \times 10^4$ . It was found that the deposition of particles to the floors is higher than that to vertical wall and ceiling surfaces. Particle deposition to the floors decrease with increasing air speed while particle deposition to the wall and ceiling increase with air speed increase (Zhang and Li 2008). The numerical simulation has been done to investigate the airflow behaviour and particle dispersion in the vertical ventilation duct for two scenarios, one with and one without a baffle. For these simulations, the low Reynolds number type k- $\epsilon$  turbulent model was selected. They found that a vertical duct with a baffle increased the particle deposition (Phuong and Ito 2013).

As it is seen from the above review of the previous simulation studies, for the duct and channel flow most works use Eulerian-Lagrangian approach for the simulation of aerosol particle dispersion. Zhang and Chen (Zhang and Chen 2007) also concluded that the Eulerian-Lagrangian method is more capable in predicting the aerosol particle dispersion.

Thus, in this study the Eulerian-Lagrangian method was selected for aerosol particle dynamic behaviour simulation in 3D duct ventilation system in order to investigate the effects of duct geometry, Reynolds number and particle size on the ventilation efficiency.

## **1.6 Code-Saturne software**

Code-Saturne which is an open source CFD software, was developed at Electricité de France (EDF) R&D and distributed under the GNU General Public License (GPL) since 2007. Code-Saturne is a Navier-Stokes equations solver. It can be used in a large range of applications including steady or unsteady, laminar or turbulent, isothermal or non-isothermal and incompressible or weakly dilatable conditions for 2D, 2D-axisymmetric and also 3D flows. Several turbulent models are available in Code-Saturne, from the Reynolds-Averaged models to the Large-Eddy simulation models. Code-Saturne is based on a co-located finite volume approach, which accepts meshes composed by cells of any shape (tetrahedral, hexahedral, polyhedral, etc.) and grid structures of any type (unstructured, hybrid, block structured, etc.) (Saturne 2015).

In this study, Code-Saturne (version 4.0) is used to simulate the airflow and particle dispersion. A Reynolds-Average Navier-Stokes (RANS) turbulence model ( $k-\epsilon$  model) was selected for airflow simulations and the dynamic behaviour of aerosol particles was modeled using the Lagrangian approach.

## **CHAPTER 2**

### **MATHEMATICAL MODEL AND METHODOLOGY**

In this chapter, a methodology for numerical investigation of ventilation ducts will be proposed. The main objective of this chapter is to suggest an appropriate geometrical and mathematical model together with a numerical method to simulate the airflow and aerosol particle behaviour in 3D duct flow. The chapter begins with the problem definition. In this section the duct ventilation system is described briefly and then, the studied geometries and the meshes used for the simulations are described. After that, the applied boundary conditions and the selected ventilation scenarios for simulations are presented. In the next section, the numerical methods and the mathematical model used for airflow and particle simulations are described. Then, the procedure used to analyze the results in order to find the most effective ventilation scenario is defined. Thereafter, it is explained how we validate the Code-Saturne capability to predict the airflow pattern and particle dispersion and deposition into a duct. The chapter is finished by a brief summary.

#### **2.1 Problem definition**

##### **2.1.1 Duct ventilation system**

Accumulation of deposited aerosol particles on the ventilation duct surfaces decreases the efficiency of these systems in removing the contaminants from the room. Then, it is important to study the duct systems in order to reduce the particles deposition and improve their effectiveness (Cheong 1997). The system simulated in this study is a straight duct with a rectangular cross section in which one inlet and one outlet are against each other. The airflow through the duct transports the particles from inlet to outlet, in order to remove the aerosol particles from a space. In this study, the effects of duct aspect ratio, Reynolds number and particle diameter on the particle deposition in the duct were investigated by considering three aspect ratios, three levels of Reynolds number and three particle diameters. The imposed airflow velocity for each aspect ratio was adjusted to obtain three fixed levels of Reynolds number.

### 2.1.2 Geometry and mesh

In this section, first the studied geometry is defined. Then, the mesh properties and the procedure used to study the effect of mesh density on the results are described. The length (L in x direction) of the studied duct is 9 m. The width (W in y direction) and the height (H in z direction) of the studied duct were  $0.3 \text{ m} \times 0.3 \text{ m}$  for the aspect ratio of 1,  $0.6 \text{ m} \times 0.3 \text{ m}$  for the aspect ratio equal to 2 and  $1.2 \text{ m} \times 0.3 \text{ m}$  for the aspect ratio of 4. The duct aspect ratio is defined as  $\alpha = W/H$ . Figure 2.1 shows the studied duct geometries with different aspect ratios.

To investigate the effect of the mesh on the results uncertainty, three meshes with different number of cells were created for the duct geometry with the aspect ratio of 1.

- Coarse mesh with 80000 hexahedral cells;
- Moderately dense mesh with 160000 hexahedral cells;
- Dense mesh with 240000 hexahedral cells.

For all three meshes, there are 20 cells in y direction and 20 cells in z direction. In both directions, element dimensions with a parabolic distribution were used to allow finer elements near the walls. The growth rates are defined by  $((\frac{y}{0.3}) - 0.5)^2$  and  $((\frac{z}{0.3}) - 0.5)^2$ . The value of dimensionless wall distance ( $y^+ = u^*y/\nu$ ,  $\nu$ : fluid kinematic viscosity,  $y$ : distance of the first cell from the wall,  $u^*$  = friction velocity =  $\sqrt{\tau_w/\rho}$ ,  $\tau_w$ : wall shear stress,  $\rho$ : fluid density) was 7.9 for the Reynolds number of  $7.36 \times 10^3$  for all meshes. In stream wise direction, there are 200 cells for coarse mesh, 400 cells for moderately dense mesh and 600 cells for dense mesh. In this direction also element dimensions with a parabolic distribution were used to allow finer elements at entrance. The growth rate is defined by  $((\frac{x}{9}) - 1)^2$ . Figure 2.2 shows the simplified representation of the mesh for duct ventilation with the aspect ratio of 1.

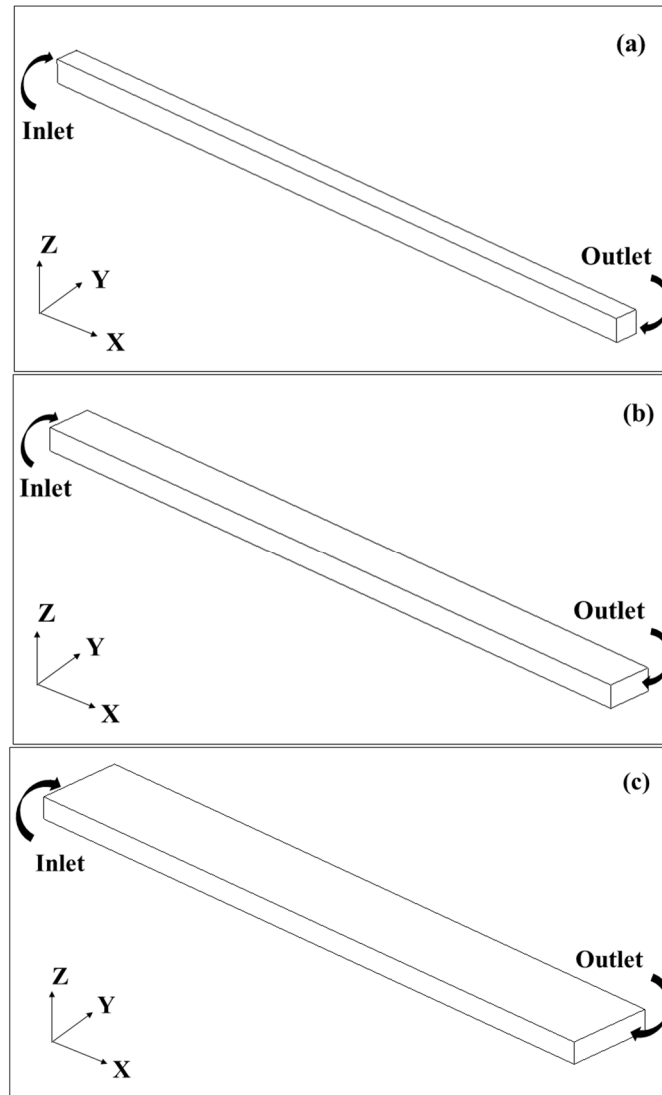


Figure 2.1 Ventilation duct geometry with aspect ratio of 1 (a), 2 (b) and 4 (c)

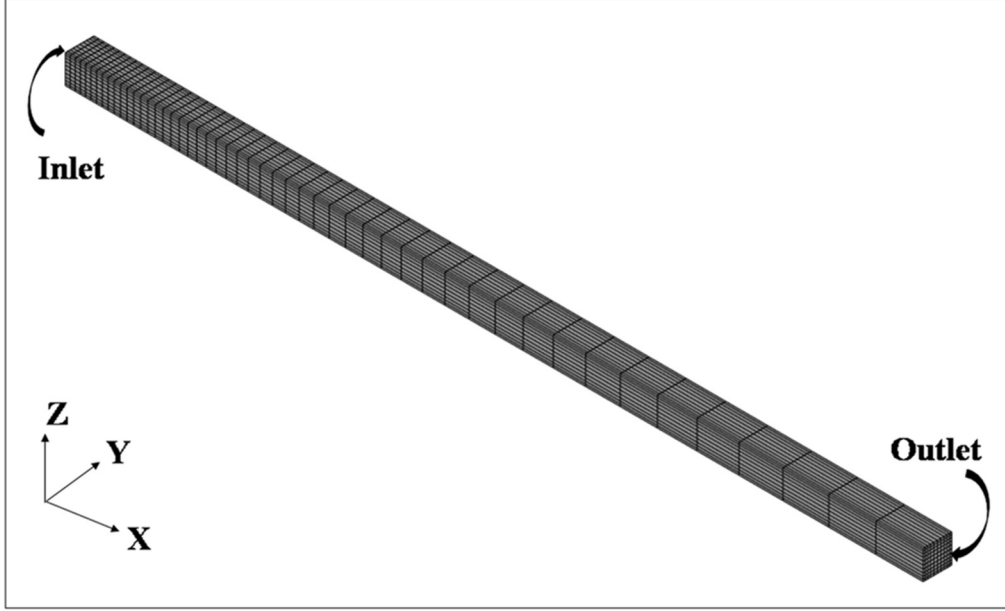


Figure 2.2 Simplified representation of the mesh for duct ventilation with the aspect ratio of 1

### 2.1.3 Boundary conditions

In this study, a fully developed airflow turbulent velocity profile was imposed at the inlet of the ventilation ducts. The airflow was imposed with three levels of Reynolds number ( $7.36 \times 10^3$ ,  $15.4 \times 10^4$  and  $36.3 \times 10^4$ ). The equations for the airflow velocity profiles imposed for each duct and each Reynolds number are presented in appendix I. The Reynolds numbers were calculated based on the inlet hydraulic diameters and the airflow mean velocity:

$$Re_{D_H} = \frac{\rho U_0 D_H}{\mu} \quad (2.1)$$

where  $U_0$  is average fluid velocity,  $\mu$  is fluid viscosity, and  $D_H$  is the hydraulic diameter which is calculated as:

$$D_H = 4A/p \quad (2.2)$$



$A$  and  $P$  are the surface and perimeter of the duct cross section, respectively. The airflow was turbulent for all the simulations because the Reynolds number minimum value for turbulent flow is 4000 (White 2003). Table 2.1 shows the airflow mean velocity for each Reynolds number and aspect ratio.

The airflow was assumed to be isothermal and incompressible. Additionally, for solid walls, no-slip boundary condition was applied. At the outlet, the pressure is the atmospheric pressure and there is no velocity gradient. To simulate the particle deposition behaviour, particles with constant density of  $1000 \text{ kg/m}^3$  were injected from the inlet. In each simulation a constant total number of  $1.4 \times 10^5$  particles were injected from the inlet with the same velocity as the airflow. Since the duct aspect ratio and the inlet airflow velocity are different for each simulation, the inlet particle volumetric concentration (particle volume/fluid volume) is variable from one scenario to another. Tables 2.2, 2.3 and 2.4 show the inlet particle volumetric concentration for different ducts and different Reynolds number. Three different particle diameters,  $d_p$ , (1, 5 and  $10 \text{ }\mu\text{m}$ ) were considered to see the effect of particle diameter on their deposition behaviour.

For each simulation, the system is considered to work continuously for a long time, thus reaching the steady state condition (assessed by no further change in the particle concentration with time).

Table 2.1 Airflow mean velocity (m/s) for different Reynolds numbers and duct aspect ratios

|   | $\alpha = 1$ | $\alpha = 2$ | $\alpha = 4$ |
|---|--------------|--------------|--------------|
| <b>Re = <math>7.36 \times 10^3</math></b> | 0.37         | 0.27         | 0.23         |
| <b>Re = <math>15.4 \times 10^4</math></b> | 7.73         | 5.77         | 4.8          |
| <b>Re = <math>36.3 \times 10^4</math></b> | 18.2         | 13.5         | 11.3         |

Table 2.2 Inlet particle volumetric concentration ( $\text{m}^3/\text{m}^3$ ) for different Reynolds numbers and duct aspect ratios ( $d_p = 1 \mu\text{m}$ )

|   | $\alpha = 1$           | $\alpha = 2$           | $\alpha = 4$           |
|---|------------------------|------------------------|------------------------|
| <b>Re = <math>7.36 \times 10^3</math></b> | $4.84 \times 10^{-15}$ | $2.46 \times 10^{-15}$ | $1.22 \times 10^{-15}$ |
| <b>Re = <math>15.4 \times 10^4</math></b> | $4.63 \times 10^{-15}$ | $2.33 \times 10^{-15}$ | $1.16 \times 10^{-15}$ |
| <b>Re = <math>36.3 \times 10^4</math></b> | $4.63 \times 10^{-15}$ | $2.31 \times 10^{-15}$ | $1.16 \times 10^{-15}$ |

Table 2.3 Inlet particle volumetric concentration ( $\text{m}^3/\text{m}^3$ ) for different Reynolds numbers and duct aspect ratios ( $d_p = 5 \mu\text{m}$ )

|   | $\alpha = 1$           | $\alpha = 2$           | $\alpha = 4$           |
|---|------------------------|------------------------|------------------------|
| <b>Re = <math>7.36 \times 10^3</math></b> | $6.05 \times 10^{-13}$ | $3.08 \times 10^{-13}$ | $1.53 \times 10^{-13}$ |
| <b>Re = <math>15.4 \times 10^4</math></b> | $5.79 \times 10^{-13}$ | $2.91 \times 10^{-13}$ | $1.45 \times 10^{-13}$ |
| <b>Re = <math>36.3 \times 10^4</math></b> | $5.79 \times 10^{-13}$ | $2.89 \times 10^{-13}$ | $1.45 \times 10^{-13}$ |

Table 2.4 Inlet particle volumetric concentration ( $\text{m}^3/\text{m}^3$ ) for different Reynolds numbers and duct aspect ratios ( $d_p = 10\mu\text{m}$ )

|   | $\alpha = 1$           | $\alpha = 2$           | $\alpha = 4$           |
|---|------------------------|------------------------|------------------------|
| <b>Re = <math>7.36 \times 10^3</math></b> | $4.84 \times 10^{-12}$ | $2.46 \times 10^{-12}$ | $1.22 \times 10^{-12}$ |
| <b>Re = <math>15.4 \times 10^4</math></b> | $4.63 \times 10^{-12}$ | $2.33 \times 10^{-12}$ | $1.16 \times 10^{-12}$ |
| <b>Re = <math>36.3 \times 10^4</math></b> | $4.63 \times 10^{-12}$ | $2.31 \times 10^{-12}$ | $1.16 \times 10^{-12}$ |

#### 2.1.4 Ventilation scenarios

According to the literature and based on the work of Cheong (Cheong 1997), 27 scenarios were defined with different levels of duct aspect ratios, airflow Reynolds numbers and particle diameters to study the particle deposition behaviour. The duct aspect ratios (1, 2 and 4), the airflow Reynolds number ( $7.36 \times 10^3$ ,  $15.4 \times 10^4$  and  $36.3 \times 10^4$ ) and the particle diameter (1, 5 and 10  $\mu\text{m}$ ) were selected as common values used by other researcher. Table 2.5 shows the selected ventilation scenarios.

Table 2.5 Selected ventilation scenarios with different levels of duct aspect ratios, airflow Reynolds numbers and particle diameters

| Scenarios   | Aspect ratio | Reynolds number    | Particle diameter ( $\mu\text{m}$ ) |
|-------------|--------------|--------------------|-------------------------------------|
| Scenario 1  | 1            | $7.36 \times 10^3$ | 1                                   |
| Scenario 2  | 1            | $7.36 \times 10^3$ | 5                                   |
| Scenario 3  | 1            | $7.36 \times 10^3$ | 10                                  |
| Scenario 4  | 1            | $15.4 \times 10^4$ | 1                                   |
| Scenario 5  | 1            | $15.4 \times 10^4$ | 5                                   |
| Scenario 6  | 1            | $15.4 \times 10^4$ | 10                                  |
| Scenario 7  | 1            | $36.3 \times 10^4$ | 1                                   |
| Scenario 8  | 1            | $36.3 \times 10^4$ | 5                                   |
| Scenario 9  | 1            | $36.3 \times 10^4$ | 10                                  |
| Scenario 10 | 2            | $7.36 \times 10^3$ | 1                                   |
| Scenario 11 | 2            | $7.36 \times 10^3$ | 5                                   |
| Scenario 12 | 2            | $7.36 \times 10^3$ | 10                                  |
| Scenario 13 | 2            | $15.4 \times 10^4$ | 1                                   |
| Scenario 14 | 2            | $15.4 \times 10^4$ | 5                                   |
| Scenario 15 | 2            | $15.4 \times 10^4$ | 10                                  |
| Scenario 16 | 2            | $36.3 \times 10^4$ | 1                                   |
| Scenario 17 | 2            | $36.3 \times 10^4$ | 5                                   |

Table 2.5 Selected ventilation scenarios with different levels of duct aspect ratios, airflow Reynolds numbers and particle diameters (continued)

| Scenarios   | Aspect ratio | Reynolds number    | Particle diameter (μm) |
|-------------|--------------|--------------------|------------------------|
| Scenario 18 | 2            | $36.3 \times 10^4$ | 10                     |
| Scenario 19 | 4            | $7.36 \times 10^3$ | 1                      |
| Scenario 20 | 4            | $7.36 \times 10^3$ | 5                      |
| Scenario 21 | 4            | $7.36 \times 10^3$ | 10                     |
| Scenario 22 | 4            | $15.4 \times 10^4$ | 1                      |
| Scenario 23 | 4            | $15.4 \times 10^4$ | 5                      |
| Scenario 24 | 4            | $15.4 \times 10^4$ | 10                     |
| Scenario 25 | 4            | $36.3 \times 10^4$ | 1                      |
| Scenario 26 | 4            | $36.3 \times 10^4$ | 5                      |
| Scenario 27 | 4            | $36.3 \times 10^4$ | 10                     |

## 2.2 Mathematical and numerical methods

### 2.2.1 Air flow simulation

Single-phase fluid was simulated based on unstructured co-located finite volume method that solves the governing equations (Beauchêne, Laudinet et al. 2011). Continuity equation for incompressible flow is (White 2003):

$$\frac{\partial u}{\partial x} + \frac{\partial v}{\partial y} + \frac{\partial w}{\partial z} = 0 \quad (2.3)$$

Variables  $u$ ,  $v$  and  $w$  are the air velocity in x, y and z directions respectively. The laminar flow is modeled by incompressible Navier-Stokes equations (White 2003):

$$\rho g_x - \frac{\partial p}{\partial x} + \mu \left( \frac{\partial^2 u}{\partial x^2} + \frac{\partial^2 u}{\partial y^2} + \frac{\partial^2 u}{\partial z^2} \right) = \rho \left( \frac{\partial u}{\partial t} + u \frac{\partial u}{\partial x} + v \frac{\partial u}{\partial y} + w \frac{\partial u}{\partial z} \right) \quad (2.4)$$

$$\rho g_y - \frac{\partial p}{\partial y} + \mu \left( \frac{\partial^2 v}{\partial x^2} + \frac{\partial^2 v}{\partial y^2} + \frac{\partial^2 v}{\partial z^2} \right) = \rho \left( \frac{\partial v}{\partial t} + u \frac{\partial v}{\partial x} + v \frac{\partial v}{\partial y} + w \frac{\partial v}{\partial z} \right) \quad (2.5)$$

$$\rho g_z - \frac{\partial p}{\partial z} + \mu \left( \frac{\partial^2 w}{\partial x^2} + \frac{\partial^2 w}{\partial y^2} + \frac{\partial^2 w}{\partial z^2} \right) = \rho \left( \frac{\partial w}{\partial t} + u \frac{\partial w}{\partial x} + v \frac{\partial w}{\partial y} + w \frac{\partial w}{\partial z} \right) \quad (2.6)$$

where  $p$  is the air pressure and  $g_x, g_y$  and  $g_z$  are the gravitational acceleration in three directions.

For turbulent flow, the mean value of velocities and pressure are represented by  $\bar{u}, \bar{v}, \bar{w}, \bar{p}$ . The turbulent flow fluctuations are represented by  $\acute{u}, \acute{v}, \acute{w}, \acute{p}$ . Then,  $u = \bar{u} + \acute{u}$ ,  $v = \bar{v} + \acute{v}$ ,  $w = \bar{w} + \acute{w}$ , and  $p = \bar{p} + \acute{p}$  are substituted in Equations (2.4), (2.5) and (2.6). The Navier-Stokes equations in turbulent flow are:

$$\begin{aligned} \rho g_x - \frac{\partial(\bar{p} + \acute{p})}{\partial x} + \mu \left( \frac{\partial^2(\bar{u} + \acute{u})}{\partial x^2} + \frac{\partial^2(\bar{u} + \acute{u})}{\partial y^2} + \frac{\partial^2(\bar{u} + \acute{u})}{\partial z^2} \right) = \\ \rho \left( \frac{\partial(\bar{u} + \acute{u})}{\partial t} + (\bar{u} + \acute{u}) \frac{\partial(\bar{u} + \acute{u})}{\partial x} + (\bar{v} + \acute{v}) \frac{\partial(\bar{u} + \acute{u})}{\partial y} + (\bar{w} + \acute{w}) \frac{\partial(\bar{u} + \acute{u})}{\partial z} \right) \end{aligned} \quad (2.7)$$

$$\begin{aligned} \rho g_y - \frac{\partial(\bar{p} + \acute{p})}{\partial y} + \mu \left( \frac{\partial^2(\bar{v} + \acute{v})}{\partial x^2} + \frac{\partial^2(\bar{v} + \acute{v})}{\partial y^2} + \frac{\partial^2(\bar{v} + \acute{v})}{\partial z^2} \right) = \\ \rho \left( \frac{\partial(\bar{v} + \acute{v})}{\partial t} + (\bar{u} + \acute{u}) \frac{\partial(\bar{v} + \acute{v})}{\partial x} + (\bar{v} + \acute{v}) \frac{\partial(\bar{v} + \acute{v})}{\partial y} + (\bar{w} + \acute{w}) \frac{\partial(\bar{v} + \acute{v})}{\partial z} \right) \end{aligned} \quad (2.8)$$

$$\begin{aligned} \rho g_z - \frac{\partial(\bar{p} + \acute{p})}{\partial z} + \mu \left( \frac{\partial^2(\bar{w} + \acute{w})}{\partial x^2} + \frac{\partial^2(\bar{w} + \acute{w})}{\partial y^2} + \frac{\partial^2(\bar{w} + \acute{w})}{\partial z^2} \right) = \\ \rho \left( \frac{\partial(\bar{w} + \acute{w})}{\partial t} + (\bar{u} + \acute{u}) \frac{\partial(\bar{w} + \acute{w})}{\partial x} + (\bar{v} + \acute{v}) \frac{\partial(\bar{w} + \acute{w})}{\partial y} + (\bar{w} + \acute{w}) \frac{\partial(\bar{w} + \acute{w})}{\partial z} \right) \end{aligned} \quad (2.9)$$

By averaging over time, equations will be simplified to obtain the Reynolds-Averaged Navier-Stokes (RANS) equations (White 2003):

$$\rho \left( \frac{\partial \bar{u}}{\partial t} + \bar{u} \frac{\partial \bar{u}}{\partial x} + \bar{v} \frac{\partial \bar{u}}{\partial y} + \bar{w} \frac{\partial \bar{u}}{\partial z} \right) = \rho g_x - \frac{\partial \bar{p}}{\partial x} + \mu \Delta \bar{u} - \rho \left( \frac{\partial \bar{u}\bar{u}}{\partial x} + \frac{\partial \bar{u}\bar{v}}{\partial y} + \frac{\partial \bar{u}\bar{w}}{\partial z} \right) \quad (2.10)$$

$$\rho \left( \frac{\partial \bar{v}}{\partial t} + \bar{u} \frac{\partial \bar{v}}{\partial x} + \bar{v} \frac{\partial \bar{v}}{\partial y} + \bar{w} \frac{\partial \bar{v}}{\partial z} \right) = \rho g_y - \frac{\partial \bar{p}}{\partial y} + \mu \Delta \bar{v} - \rho \left( \frac{\partial \bar{u}\bar{v}}{\partial x} + \frac{\partial \bar{v}\bar{v}}{\partial y} + \frac{\partial \bar{v}\bar{w}}{\partial z} \right) \quad (2.11)$$

$$\rho \left( \frac{\partial \bar{w}}{\partial t} + \bar{u} \frac{\partial \bar{w}}{\partial x} + \bar{v} \frac{\partial \bar{w}}{\partial y} + \bar{w} \frac{\partial \bar{w}}{\partial z} \right) = \rho g_z - \frac{\partial \bar{p}}{\partial z} + \mu \Delta \bar{w} - \rho \left( \frac{\partial \bar{u}\bar{w}}{\partial x} + \frac{\partial \bar{v}\bar{w}}{\partial y} + \frac{\partial \bar{w}\bar{w}}{\partial z} \right) \quad (2.12)$$

or in tensor form:

$$\rho \frac{D \bar{u}_i}{Dt} = \rho g_i - \frac{\partial \bar{p}}{\partial x_i} + \mu \Delta \bar{u}_i - \rho \left( \frac{\partial \bar{u}_i \bar{u}_j}{\partial x_j} \right) \quad (2.13)$$

In this study, the low Reynolds number v2f BL-v2/k turbulence model which is available in Code-Saturne used to simulate the 2D turbulent channel flow and the k- $\epsilon$  model was used to simulate 3D turbulent duct flow. This model solves two transport partial differential equations (PDE) for the turbulent kinetic energy,  $k$ , and turbulence dissipation rate,  $\epsilon$  (Saturne 2015).

### 2.2.2 Particles simulation

For two phases flow (fluid containing particles), an Eulerian-Lagrangian approach was used wherein individual particles are simulated based on a Probability Distribution Function (PDF) approach. Since particle volume fraction at the inlet was very low (less than  $5 \times 10^{-12}$  m<sup>3</sup> particle /m<sup>3</sup> of air for all of the scenarios), then one way coupling assumption is valid. This assumption means that particle-particle interactions and the influence of the particles on the fluid field can be neglected. With this assumption, particles do not affect the momentum of the fluid but the fluid affects the particle momentum (Dorogan 2012). Two-way coupling would have been required if the particle volume fraction was more than  $10^{-4}$  m<sup>3</sup> particle/m<sup>3</sup> of air (Reinhardt and Kleiser 2015). To simulate particle dispersion and deposition on solid surfaces, the fluid flow is first modeled with the Eulerian approach as described in section

2.2.2.1. Then, particles are injected into the frozen flow field and particle trajectories are tracked.

#### **2.2.2.1 Eulerian-Lagrangian approach**

To predict the particle dispersion due to turbulence, the stochastic tracking model or the particle cloud model can be used. In the stochastic tracking (random walk) model, the instantaneous turbulent velocity fluctuations, which have effect on the particle trajectories through the use of stochastic methods, are considered. In this model, the turbulent dispersion of particles is predicted by integrating the trajectory equations for individual particles. The trajectory equation includes the mean fluid phase velocity,  $\bar{u}$ ,  $\bar{v}$  and  $\bar{w}$ , and the instantaneous value of the fluctuating gas flow velocity,  $u'$ ,  $v'$  and  $w'$ , along the particle path during the integration. The trajectory in this way should be computed for a sufficient number of representative particles to account for the random effects of turbulence on the particle dispersion.

In the particle cloud model, the turbulent dispersion of particles will be tracked as a cloud of particles about a mean trajectory. To obtain the mean trajectory for all particles represented by the cloud, the ensemble-averaged equations of motion are solved. The cloud enters the domain and expands due to turbulent dispersion. The cloud is transported through the domain while expanding (due to turbulence dispersion) until it exits. In the cloud, the concentration of particles is defined by a Gaussian probability density function (PDF) based on their position in the cloud relative to the mean trajectory. The variance of the PDF is based on the degree of particle dispersion because of turbulent fluctuations (Baxter 1989, Litchford and Jeng 1991, Baxter and Smith 1993, Jain 1995).

### 2.2.2.2 Equation of motion

In the Lagrangian approach, the particle phase is split into a set of individual particles. Particles are tracked separately and equations of particle motion are solved for each particle. To obtain the equation of particle motion, these assumptions are used (Zhao, Zhang et al. 2004):

- there are no heat and mass transfer between the air and particles;
- particles do not rebound on solid surfaces;
- there is no particle coagulation;
- all particles in this process are in spherical solid shape.

According to Newton's second law, the motion equation of individual particle is:

$$\frac{du_{pi}}{dt} = F_i \quad (2.14)$$

where  $u_{pi}$  (m/s) is particle velocity in  $i$  direction and  $F_i$  (m/s<sup>2</sup>) is the external forces per unit particle mass applied on the particle in  $i$  direction. External forces exerted on the particle are given by (Zhao, Zhang et al. 2004):

$$F_i = F_D(u_i - u_{pi}) + g_i \left(1 - \frac{\rho}{\rho_p}\right) + F_{ai} \quad (2.15)$$

$u_i$  (m/s) is the air velocity in  $i$  direction,  $g_i$  (m/s<sup>2</sup>) is the gravitational acceleration in the  $i$  direction and  $\rho_p$  (kg/m<sup>3</sup>) is the particle density.  $F_{ai}$  (m/s<sup>2</sup>) is the additional forces applied on the particle. These forces, depending on the particle properties and flow condition, include pressure gradient force, Brownian force, virtual mass force, Basset force due to unsteady flow, lift force caused by shear (Saffman's lift force) and thermophoretic force due to temperature gradient. Because of the isothermal assumption for this study, the thermophoretic force is negligible. The first term in the right hand side of Equation (2.15) represents the drag force per unit of particle mass,  $F_{drag}$  (m/s<sup>2</sup>), which is defined as:



$$F_{drag} = F_D(u_i - u_{pi}) = \frac{18\mu}{\rho_p d_p^2} \frac{C_D Re_p}{24} (u_i - u_{pi}) \quad (2.16)$$

where  $d_p$  (m) is the particle diameter,  $C_D$  is the drag coefficient and  $Re_p$  is the particle Reynolds number which is calculated based on the particle relative velocity and particle diameter (Kulkarni, Baron et al. 2011):

$$Re_p = \frac{(u_i - u_{pi}) d_p \rho}{\mu} \quad (2.17)$$

and  $C_D$  is given by:

$$C_D = a_1 + \frac{a_2}{Re_p} + \frac{a_3}{Re_p^2} \quad (2.18)$$

For smooth spherical particles and a given Reynolds number,  $\alpha_1$ ,  $\alpha_2$  and  $\alpha_3$  are constant. The value of  $\alpha_1$ ,  $\alpha_2$  and  $\alpha_3$  vary with Reynolds number. Table 2.6 lists the values of these constants for different ranges of Reynolds number.

Table 2.6 Drag coefficient-Reynolds number relationship (Morsi and Alexander 1972)

| Range of Reynolds Number            | Expression of Drag Coefficient                                  |
|-------------------------------------|---|
| <b>Re &lt; 0.1</b>                  | 24/Re   |
| <b>0.1 &lt; Re &lt; 1.0</b>         | 22.73/Re + 0.0903/Re <sup>2</sup> + 3.69                        |
| <b>1.0 &lt; Re &lt; 10.0</b>        | 29.1667/Re - 3.8889/Re <sup>2</sup> + 1.222                     |
| <b>10.0 &lt; Re &lt; 100.0</b>      | 46.5/Re - 116.67/Re <sup>2</sup> + 0.6167                       |
| <b>100.0 &lt; Re &lt; 1000.0</b>    | 98.33/Re - 2778/Re <sup>2</sup> + 0.3644                        |
| <b>1000.0 &lt; Re &lt; 5000.0</b>   | 148.62/Re - 4.75 × 10 <sup>4</sup> /Re <sup>2</sup> + 0.357     |
| <b>5000.0 &lt; Re &lt; 10000.0</b>  | -490.546/Re + 57.87 × 10 <sup>4</sup> /Re <sup>2</sup> + 0.46   |
| <b>10000.0 &lt; Re &lt; 50000.0</b> | -1662.5/Re + 5.4167 × 10 <sup>6</sup> /Re <sup>2</sup> + 0.5191 |

The second term of Equation (2.15) represents the gravitational force minus the buoyancy force on the particle per unit of particle mass ( $m/s^2$ ). Since the ratio of the air density to the

particle density is very small in this study (0.0012), the buoyancy force will be very small compared with the gravitational force. The third term of Equation (2.15) is the additional forces that are applied on the particles. The magnitude of these forces is affected by the airflow condition and particle properties like particle density and particle size. Some of these forces are too small and could be neglected since the particle diameter and the ratio of air density per particle density are very small (see below).

**Pressure gradient force:** The ratio of the pressure gradient force,  $F_P$ , to the external force applied on the particle, can be written as (Wang 1989):

$$\frac{F_P}{F_i} \approx \frac{\rho a_a}{\rho_p a_p} \quad (2.19)$$

where  $a_p(m/s^2)$  is the acceleration of the particle and  $a_a(m/s^2)$  is the acceleration of the air. Since for our case of air-particle flow (particle diameter  $\leq 10 \mu m$ ), the acceleration rates of the particle and air are in the same order of magnitude, the ratio of pressure gradient force to the external force could be:

$$\frac{F_P}{F_i} \approx \frac{\rho}{\rho_p} \quad (2.20)$$

As mentioned, the ratio of the air density to the particle density is very small then the pressure gradient force is small enough compared to the external force for indoor air-particle flow and could be neglected.

**Virtual mass force:** Virtual mass force,  $F_m$ , is the force required to accelerate the mass of the surrounding continuous phase. The ratio of this force to the external force applied on the spherical particle is (Wang 1989):

$$\frac{F_m}{F_i} = \frac{\rho}{2\rho_p} \quad (2.21)$$

Again, since the ratio of the air density to the particle density is very small for indoor air-particle flow, compared to the external force applied on the particle, the virtual mass force is very small and could be neglected.

**Basset force:** This additional force is also caused by the unsteady flow. The ratio of the Basset force ( $F_{Ba}$ ) to the drag force for the uniform accelerated motion is (Wang 1989):

$$\frac{F_{Ba}}{F_D} = \left( \frac{18\rho\tau_p}{C_D\pi\rho_p t} \right)^{0.5} \quad (2.22)$$

As Basset force is caused by the unsteady flow, this force is dependent on the time. The relaxation time is given by:

$$\tau_p = \frac{\rho_p d_p^2 C_c}{18\mu} \quad (2.23)$$

where  $C_c$  is the Cunningham slip correction factor to Stokes' drag law (Ounis, Ahmadi et al. 1991). With the small air density to particle density ratio and the small particle size that implies a small response time, the Basset force also could be neglected.

**Brownian force:** Brownian force components,  $F_{bi}$ , are in the form of:

$$F_{bi} = G_i \sqrt{\pi S_0 / \Delta t} \quad (2.24)$$

$\Delta t$  is the time step,  $G_i$  are zero-mean, unit-variance independent Gaussian random numbers and  $S_0$  is the spectral intensity:

$$S_0 = \frac{216\nu\sigma T}{\pi^2 \rho d_p^5 (\rho_p/\rho) C_c} \quad (2.25)$$

where  $\nu$  ( $m^2/s$ ) is the kinematic viscosity of the air,  $\sigma$  is the Boltzmann constant and is equal to  $1.38 \times 10^{-23} N. m/ K$ ,  $T$  is the fluid absolute temperature in Kelvin (Ounis, Ahmadi et al. 1991).

**Saffman's lift force:** This additional force ( $F_{si}$ ) is defined by (Saffman 1965):

$$F_{si} = \frac{2K_C \nu^{0.5} \rho d_{ij}}{\rho_p d_p (d_{lk} d_{kl})^{0.25}} (u_i - u_{pi}) \quad (2.26)$$

where  $K_C$  is 2.594 and  $d_{ij}$  is the deformation tensor (Li and Ahmadi 1992).

Brownian force and Saffman's lift force are relatively large for the flow field and fine particles (Zhao, Zhang et al. 2004). So in this study, the additional force includes only Brownian force and Saffman's lift force, which can be important in sub-micron particle's motion near the walls. Near the walls because of the large velocity gradient, Saffman's lift force could be dominant compared to the Brownian force.

Code-Saturne considers the Saffman's lift force as an additional force in particle motion equation but we will not study the effect of this force on particle deposition behaviour by counting the gravity effect.

### 2.2.3 Numerical method

In this study, for the turbulent equations, a first order upwind discretization scheme is used. For the momentum equations a second order centered scheme is used (Saturne 2015). By integrating the equations of particles motion with a Runge-Kutta method, the trajectory of particles can be tracked (Saturne 2015).

### 2.3 Ventilation efficiency

Simulation results can be used to calculate the effectiveness of the ventilation duct in particle removal for different Reynolds number, duct aspect ratios and particle sizes. For evaluating the effectiveness of the ventilation system, the percentage of the deposited particles on the duct surfaces is calculated from the average concentration of particles at different duct lengths (different distances from the inlet). Average particle concentrations at different lengths are obtained by integration over the width and the height of the duct. Because of the turbulence effects, we see different behaviour of the particles near the inlet, then we decided to ignore the first one meter of the duct. Our effectiveness calculations are based on the rest of the duct length. Duct efficiency,  $\eta_{duct}$ , at each distance (L) (from the inlet) is calculated by:

$$\eta_{duct} = \frac{\bar{C}_{x=L}}{\bar{C}_{x=1}} \quad (2.27)$$

where  $\bar{C}_{x=L}$  is the averaged volumetric concentration of the particle at x equal to L meter from the inlet and  $\bar{C}_{x=1}$  is the averaged volumetric concentration of particle at x equal to 1 meter as an initial point.

Using Equation (2.28), the percentage of the particles deposited on the walls at each distance is then obtained:

$$\%Deposited\ particles = 100 \times (1 - \eta_{duct}) \quad (2.28)$$

### 2.4 Prediction of airflow pattern and particle deposition in 2D channel

In this section, it is explained how we validate the Code-Saturne capability to predict the airflow pattern in 2D laminar and turbulent channel flow, and 3D turbulent duct flow. The correlation used to validate the particle dispersion and deposition results in 2D turbulent channel flow is also presented.

## 2.4.1 Prediction of airflow pattern in 2D channel

### 2.4.1.1 Velocity profile

For 2D laminar channel flow, the velocity profile obtained near the exit (in fully developed region) by CFD simulation will be compared with the velocity profile obtained by the theoretical equation for laminar airflow (White 2003). For a 2D flow in horizontal direction with assumptions of steady state and fully developed flow, the Navier-Stokes equation in x direction (Equation (2.4)) reduces to Equation (2.29):

$$\frac{\partial p}{\partial x} = \mu \frac{d^2 u}{dy^2} \quad (2.29)$$

Integration of Equation (2.29) leads to:

$$\frac{du}{dy} = \frac{1}{\mu} \frac{dp}{dx} y + C_1 \quad (2.30)$$

$$u = \frac{1}{2\mu} \frac{dp}{dx} y^2 + C_1 y + C_2 \quad (2.31)$$

Because of the no slip boundary condition, the airflow velocity is zero at the wall surfaces.

Then:

$$\text{at } y = 0 \rightarrow u = 0 \rightarrow C_2 = 0$$

$$\text{at } y = W \rightarrow u = 0 \rightarrow \frac{1}{2\mu} \frac{dp}{dx} W^2 + C_1 W = 0 \rightarrow C_1 = -\frac{1}{2\mu} \frac{dp}{dx} W$$

If  $C_1$  and  $C_2$  are substituted into Equation (2.31), the velocity profile will be:

$$u = \frac{W^2}{2\mu} \frac{dp}{dx} \left( \left( \frac{y}{W} \right)^2 - \frac{y}{W} \right) \quad (2.32)$$

where  $W$  is the width of the channel. Average velocity is constant along the channel and is equal to  $U_0$ , which can be found by integrating the velocity profile over the width of the channel:

$$U_0 = \frac{\int_0^W u dy}{\int_0^W dy} = \frac{\int_0^W \frac{W^2}{2\mu} \left( \left( \frac{y}{W} \right)^2 - \frac{y}{W} \right) \frac{dp}{dx} dy}{\int_0^W dy} \quad (2.33)$$

Then, Equation (2.32) can be re-written as (White 2003):

$$u = 6U_0 \left( \frac{y}{W} - \left( \frac{y}{W} \right)^2 \right) \quad (2.34)$$

To study the accuracy of the simulation results, the error between the simulation results and the theoretical values (Equation (2.34)) at 100 points along the channel width is obtained by this equation:

$$Error = (U_{i \text{ exact}} - U_{i \text{ simulation}}) \quad (2.35)$$

The Mean Squared Error (MSE) is then obtained by Equation (2.36):

$$MSE = \frac{1}{n} \sum_{i=0}^n (U_{i \text{ exact}} - U_{i \text{ simulation}})^2 \quad (2.36)$$

where  $n$  is the number of points along the channel width (100).

For 2D turbulent airflow, the results obtained by CFD simulations will be compared with the numerical simulation available in the literature. The turbulent velocity profile, turbulent kinetic energy and turbulence dissipation rate profiles in fully developed region will be compared to the work of Tian and Ahmadi (Tian and Ahmadi 2007). The results of airflow pattern in 3D turbulent duct flow will be compared with the numerical results obtained by Yao et al (Yao, Fairweather et al. 2014).

#### 2.4.1.2 Entrance length

The entrance length is defined as the distance from the inlet where the centerline velocity reaches 99.9% of its fully developed value. The entrance length obtained from CFD simulation results by this definition will be compared with the empirical correlations available in the literature. The entrance length,  $L_e$ , for a laminar channel flow suggested by Muzychka (Muzychka and Yovanovich 2009) is calculated by Equation (2.37):

$$L_e = 0.011 Re_{D_H} D_H \quad (2.37)$$

For turbulent channel flow, the empirical relation (White 2003) can be used to compute the entrance length for the Reynolds number larger than 4000:

$$\frac{L_e}{D_H} = 4.4 \times Re_{D_H}^{1/6} \quad (2.38)$$

#### 2.4.1.3 Friction factor

Friction coefficient ( $C_f$ ) for developed laminar channel flow is calculated by Equation (2.39) (White 1991):

$$C_f = \frac{24}{Re_{D_H}} \quad (2.39)$$

For the turbulent flow, the friction factor at the wall can be obtained by (White 1991):

$$\frac{1}{\Lambda^{1/2}} = 2.0 \log \left( Re_{D_H} \times \Lambda^{\frac{1}{2}} \right) - 1.19 \quad (2.40)$$

where  $\Lambda = 4C_f$  is the Darcy friction factor at the wall. In order to compare the friction factors obtained by these empirical relations with the ones obtained by simulation, the wall shear stress ( $\tau_w$ ) calculated from simulation is converted to the friction factor by Equation (2.41) (White 1991):



$$C_f = \frac{\tau_w}{1/2\rho U_0^2} \quad (2.41)$$

## 2.4.2 Prediction of particle deposition in 2D turbulent channel flow

### 2.4.2.1 Particle deposition velocity

To validate the Code-Saturne capability to predict particle deposition, the simulations were done for two different conditions. First, the turbulent dispersion effect (Langevin effect) is considered and second, the turbulent dispersion effect on the particle trajectory is neglected. The non-dimensional deposition velocity ( $u_d^+$ ) of particles investigated by CFD simulation is compared with the non-dimensional deposition velocity obtained by an empirical equation provided by Wood (1981) which is valid for small particles with a diameter in the range of 0.01 to 50  $\mu\text{m}$  (Wood 1981):

$$u_d^+ = 0.057Sc^{-\frac{2}{3}} + 4.5 \times 10^{-4}\tau^{+2} + u_t^+ \quad (2.42)$$

where  $Sc$  is Schmidt number and is defined as the ratio of kinematic viscosity to diffusion coefficient:

$$Sc = \frac{\nu}{D} = \frac{\mu}{\rho D} \quad (2.43)$$

In Equation (2.43),  $D$  is the particle diffusion coefficient and will be estimated from Stokes-Einstein relation:

$$D = \frac{\sigma T C_c}{3\pi\mu d_p} \quad (2.44)$$

In Equation (2.42), the last term accounts for the contribution to particle deposition velocity by gravitational sedimentation in a 2D channel, which is defined as:

$$u_t^+ = \tau^+ g^+ \quad (2.45)$$

where  $g^+$  is expressed with the following form:

$$g^+ = \frac{\nu}{u^{*3}} g \quad (2.46)$$

$\tau^+$  is the non-dimensional particle relaxation time which is defined as:

$$\tau^+ = \frac{\tau_p u^{*2}}{\nu} = \frac{\rho_p d_p^2 C_c}{18\mu} \times \frac{u^{*2}}{\nu} \quad (2.47)$$

$u^*$  is the friction velocity of the fluid and calculated by Equation (2.48):

$$u^* = \sqrt{\tau_w / \rho} \quad (2.48)$$

The non-dimensional deposition velocity  $u_d^+$  for results computed by Code-Saturne is calculated by the following relationship:

$$u_d^+ = \frac{u_{deposition}}{u^*} \quad (2.49)$$

The deposition velocity of particles ( $u_{deposition}$ ) was calculated from CFD simulation results by averaging the particles velocity in gravity (y) direction over the width and the length of the channel. The particle velocity was averaged to take into account the small variability in deposition velocity due to possible errors in numerical solution. In addition, deposition velocity may change slightly over the channel width due to small variability in the diffusive deposition velocity. As it will be explained in detail in section 2.4.2.2, particle deposition in our simulation conditions occurs mainly by gravitational and diffusional deposition mechanisms. In most of our simulation conditions the gravitational deposition is predominant, but in some cases diffusional mechanism can also be important. In contrast

with the terminal settling velocity which is constant at all locations in the channel, diffusive deposition velocity can change over the channel width.

#### 2.4.2.2 Particle deposition

As particles move through the duct, some of them are lost by different deposition mechanisms. Among these deposition mechanisms, the common ones relevant to our duct geometry are: diffusional deposition and gravitational settling. The overall transport efficiency is the product of the transport efficiency of each mechanisms (Kulkarni, Baron et al. 2011). Thus, the efficiency of the channel ( $\eta_{duct}$ ) will be obtained by:

$$\eta_{duct} = \eta_{grav}\eta_{diff} \quad (2.50)$$

where  $\eta_{grav}$  is the transport efficiency for gravitational deposition and  $\eta_{diff}$  is the transport efficiency for diffusive particle deposition. These two mechanisms will be explained in detail. In the following relations, it is assumed that the cross section of the channel is circular (tube). So we will use the hydraulic diameter for our case of duct flow.

The duct efficiency from Equation (2.50) is then compared with the duct efficiency calculated from the simulation results obtained as the ratio of the average particle concentration at the duct outlet over average particle concentration at 1 m from the inlet. Average particle concentration at inlet and outlet is found by integration over the duct width.

##### 2.4.2.2.1 Gravitational Settling

During particle transportation, gravitational force causes particles to settle and deposit on the lower wall. For laminar flow in a horizontal tube,  $\eta_{grav}$  is (Kulkarni, Baron et al. 2011):

$$\eta_{grav} = 1 - \frac{2}{\pi} \left[ 2\varepsilon \sqrt{1 - \varepsilon^{\frac{2}{3}}} - \varepsilon^{\frac{1}{3}} \sqrt{1 - \varepsilon^{\frac{2}{3}}} + \arcsin\left(\varepsilon^{\frac{1}{3}}\right) \right] \quad (2.51)$$

$$\varepsilon = \frac{3}{4}Z = \frac{3}{4}\frac{L}{d}\frac{V_{ts}}{U_0} \quad (2.52)$$

where  $L$  and  $d$  are the length and the inside diameter of the tube, respectively, and  $Z$  is the gravitational deposition parameter. For the turbulent flow in a horizontal tube,  $\eta_{grav}$  is calculated by (Kulkarni, Baron et al. 2011):

$$\eta_{grav} = \exp\left[-\frac{4Z}{\pi}\right] = \exp\left[-\frac{dLV_{ts}}{Q}\right] \quad (2.53)$$

where  $Q$  is the volumetric fluid flow:

$$Q = \frac{\pi d^2 U_0}{4} \quad (2.54)$$

$V_{ts}$  is the terminal settling velocity of the particle which is calculated as below in the Stokes regime (Kulkarni, Baron et al. 2011):

$$V_{ts} = \frac{\rho_p d_p^2 g C_c}{18\mu} \quad (2.55)$$

Equation (2.55) is valid for  $Re_p < 0.1$ . The terminal settling velocity of particle could be rewritten as:

$$V_{ts} = \tau_p g \quad (2.56)$$

Drag force is calculated by the Stokes' law in continuum regime. In slip regime particles with diameter equal or less than the mean free path of the gas, settle faster than predicted by Stokes's law in continuum regime, due to the slip at the surface of the particle. So in slip condition, the relative velocity of the particle decreases and the drag force decreases compared to the one obtained by Stokes' law in continuum regime. Thus, in slip condition, the Cunningham correction factor is used in order to correct this difference. Thus for the slip

regime, the Cunningham slip correction factor ( $C_c$ ) is used to correct this difference (Allen and Raabe 1985):

$$C_c = 1 + Kn \left[ \alpha + \beta \exp \left( -\frac{\gamma}{Kn} \right) \right] \quad (2.57)$$

where for solid particles  $\alpha = 1.142$ ,  $\beta = 0.558$  and  $\gamma = 0.999$  which are consistent with mean free path in air at standard atmospheric pressure and temperature (Allen and Raabe 1985).  $Kn$  is Knudsen number, which is defined by the fraction of the gas molecular mean free path to the physical dimension of the particle. In continuum flow regime,  $Kn \ll 1$  and in free molecular flow regime,  $Kn \gg 1$ . In slip flow regime or the transition regime,  $Kn \cong 0.4$  to  $20$  (Kulkarni, Baron et al. 2011):

$$Kn = \frac{2\lambda}{d_p} \quad (2.58)$$

$\lambda$  is the mean free path of the molecule (the mean distance that a molecule travels before colliding with another molecule) which is calculated by Equation (2.59) for a given temperature ( $T$ ) and pressure ( $P$ ) (Willeke 1976):

$$\lambda = \frac{\lambda_r(101/P)(T/293)(1+110/293)}{1+(110/T)} \quad (2.59)$$

$\lambda_r$  is the mean free path in air at  $T = 293 \text{ K}$  and atmospheric pressure. The value of  $\lambda_r$  is  $0.0664 \text{ } \mu\text{m}$ . For our simulation conditions (constant temperature of  $288 \text{ K}$  and constant pressure of  $101 \text{ kPa}$ ), the mean free path will be equal to  $0.0649 \text{ } \mu\text{m}$ . Then in this study, Knudsen number ( $Kn$ ) is  $0.13$  for particle diameter of  $1 \text{ } \mu\text{m}$ ,  $0.026$  for particle diameter of  $5 \text{ } \mu\text{m}$  and  $0.013$  for particle diameter of  $10 \text{ } \mu\text{m}$ .

#### 2.4.2.2.2 Diffusional deposition

Diffusional deposition is caused by the particle concentration gradient between two points. Particle concentration at the wall is zero at the initial time, then particles diffuse from higher concentration regions toward the wall and deposit on the wall. Transport efficiency for diffusive particle deposition in tube ( $\eta_{diff}$ ) is calculated as below (Kulkarni, Baron et al. 2011):

$$\eta_{diff} = \exp\left[-\frac{\pi d L V_{diff}}{Q}\right] = \exp[-\xi Sh] \quad (2.60)$$

where  $V_{diff}$  is diffusive deposition velocity of particle and  $Sh$  is Sherwood number which is a dimensionless mass transfer coefficient:

$$Sh = \frac{V_{diff} \times d}{D} \quad (2.61)$$

The Sherwood number for laminar flow will be obtained by (Holman 1972):

$$Sh = 3.66 + \frac{0.0668 \frac{d}{L} Re_f Sc}{1 + 0.04 \left[\frac{d}{L} Re_f Sc\right]^{2/3}} = 3.66 + \frac{0.2672}{\xi + 0.10079 \xi^{1/3}} \quad (2.62)$$

and

$$\xi = \frac{\pi D L}{Q} \quad (2.63)$$

The Sherwood number for turbulent flow will be obtained by (Friedlander 1977):

$$Sh = 0.0118 Re_{DH}^{7/8} Sc^{1/3} \quad (2.64)$$

By increasing the Schmidt number, mass transfer due to convection will increase compared to the mass transfer caused by Brownian diffusion of the particles. Schmidt number is relatively independent of temperature and pressure near standard conditions (Kulkarni, Baron et al. 2011).

## **2.5 Summary**

In this chapter, the studied geometries and the meshes used for simulations were presented. For the geometries with the aspect ratio of 1, 2 and 4, the selected meshes have 160000, 320000 and 640000 hexahedral cells, respectively. Then, the applied boundary conditions and the selected ventilation scenarios were discussed. The mathematical model of airflow and particle simulations and the numerical methods used were presented to reach the first specific objective of this thesis. The Eulerian-Lagrangian approach were proposed as the appropriate mathematical model to simulate the airflow and aerosol particle behaviour in 3D duct flow. Thereafter, the percentage of the deposited particles on the duct surfaces was defined as a metric used to analyze the results in order to find the most effective ventilation scenario. Finally, it was explained how we validate the Code-Saturne capability in prediction of the airflow pattern and particle dispersion and deposition.





## **CHAPTER 3**

### **CODE-SATURNE VALIDATION**

For validation of Code-Saturne in single-phase flow simulations, laminar and turbulent fluid flows were simulated in a 2D channel. In this chapter, the channel geometry and the mesh used for both laminar and turbulent simulations will be presented first. Then, the boundary conditions applied in simulations will be defined. In the next part, the Code-Saturne results for laminar airflow pattern will be compared with the theoretical and empirical correlations (White 1991, Muzychka and Yovanovich 2009, White 2003). Then, the simulation results for turbulent channel flow (single-phase) will be compared with the empirical correlations (White 1991) and numerical simulation in literature (Tian and Ahmadi 2007). The results of airflow pattern in 3D turbulent duct flow will be compared with the numerical results obtained by Yao et al (Yao, Fairweather et al. 2014). In the last section of this chapter, the Code-Saturne results for particle deposition in a 2D channel will be presented and particle deposition velocity and the channel transport efficiency will be compared with results from literature (Wood 1981, Kulkarni, Baron et al. 2011).

#### **3.1 Geometry and mesh**

To validate the airflow field results, laminar and turbulent flows in a 2D channel were simulated. Figure 3.1 shows the geometry of the channel where  $L$  is the length and  $W$  is the width of the channel. For laminar airflow,  $L$  and  $W$  were 0.1 m and 0.005 m, respectively. The domain was discretized with structured elements. Three meshes were created to study the effect of the mesh size on the results.

- Coarse mesh with 12500 hexahedral cells;
- Moderately dense mesh with 25000 hexahedral cells;
- Dense mesh with 50000 hexahedral cells.

The dimension of each cell is 0.2 mm in the stream-wise direction and 0.2 mm in the lateral direction for coarse mesh, 0.1 mm for moderately dense mesh and 0.05 mm.

The turbulent airflow was simulated with the low Reynolds number  $v_2f$  BL- $v_2/k$  turbulence model which is available in Code-Saturne. For the turbulent airflow, the length and width of the channel were 5 m and 0.02 m, respectively. To investigate if the results are independent of the mesh size, three meshes with different number of cells were created for the channel geometry.

- Coarse mesh with 25000 hexahedral cells;
- Moderately dense mesh with 50000 hexahedral cells;
- Dense mesh with 75000 hexahedral cells.

For all meshes there were 500 cells in stream-wise direction and the dimension of each cell is 0.01 m in this direction. In lateral direction, element dimensions with a parabolic distribution with the growth rate of  $((\frac{y}{0.02}) - 0.5)^2$  were used to allow finer elements near the walls. This is necessary since the velocity gradient is steeper adjacent to the walls. In this direction, there were 50 cells for coarse mesh with  $y^+ = 3.24$ , 100 cells for moderately dense mesh with  $y^+ = 1.48$ , and 150 cells for dense mesh with  $y^+ = 0.962$ . Figure 3.2 shows a simplified representation of the computational mesh for turbulent channel flow.

For two-phase turbulent flow simulations, the geometry and the mesh structure are the same as the single-phase turbulent flow except the length of the channel which is 2m.

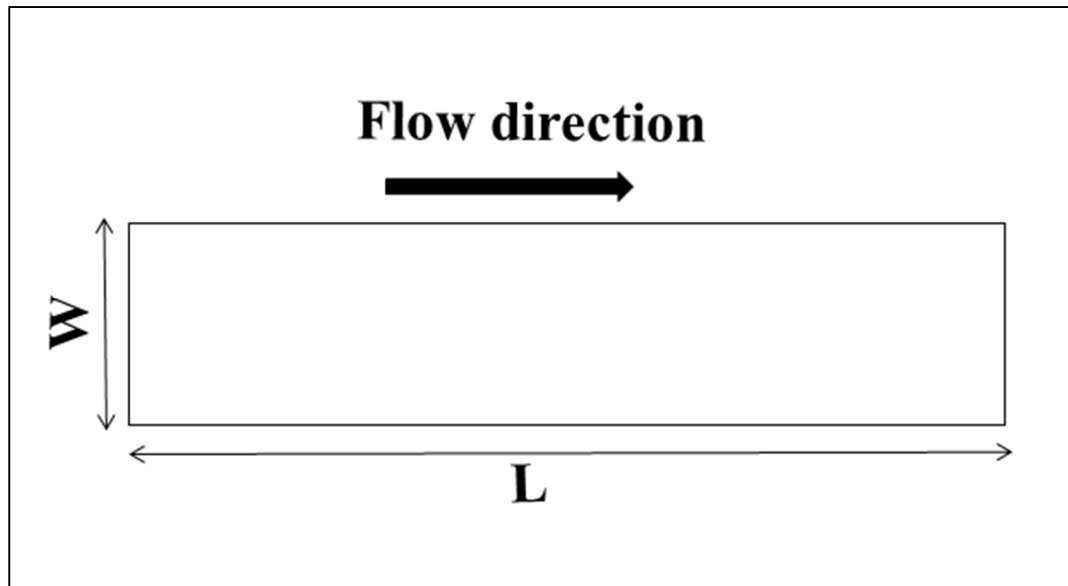


Figure 3.1 Schematic view of the channel geometry

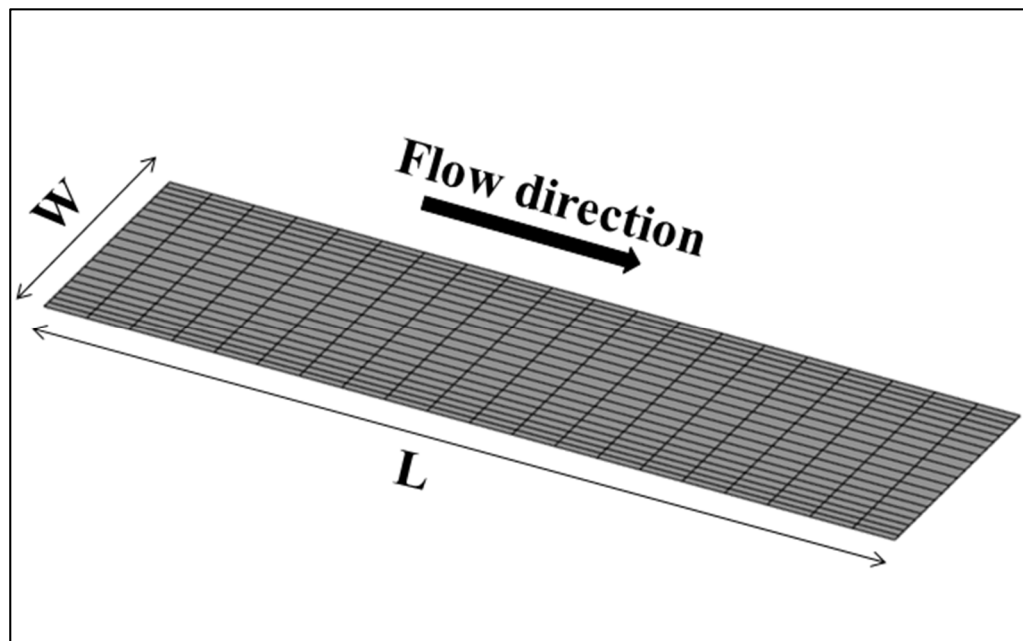


Figure 3.2 Simplified representation of the mesh for the turbulent channel flow

### 3.2 Fluid and particles properties

The air density and dynamic viscosity used in this study were  $\rho = 1.225 \text{ kg/m}^3$  and  $\mu = 1.84 \times 10^{-5} \text{ Ns/m}^2$ , respectively. In the simulation of deposition behaviour of particles, particles with a diameter ( $d_p$ ) in the range of 0.1 to 10  $\mu\text{m}$  with a constant density ( $\rho_p$ ) equal to 1000  $\text{kg/m}^3$  were considered.

### 3.3 Boundary conditions

For the laminar flow, a uniform initial velocity equal to 0.05 m/s was imposed at inlet. The Reynolds number for a channel flow is defined by Equation (2.1).  $D_H$  is equal to  $2W$  for a rectangular 2D channel. With our geometry, the Reynolds number at the inlet is 33.3, which is in the laminar flow regime. Flow is generally considered laminar if  $Re_{DH} < 2300$  (White 2003). For turbulent flow, the imposed uniform velocity at inlet was 5 m/s. The flow is in the turbulent flow regime since the Reynolds number based on the inlet velocity and channel width is  $1.33 \times 10^4$ . In both laminar and turbulent simulations, the walls are considered as smooth walls with no-slip boundary condition and at the outlet, there is the atmospheric pressure.

In two-phase flow simulations, particles were distributed evenly at the inlet with the same inlet velocity as the airflow. In all simulations, particle volume fraction at inlet was very low (between  $1.67 \times 10^{-15} \text{ m}^3 \text{ particle} / \text{m}^3 \text{ air}$  and  $1.53 \times 10^{-9} \text{ m}^3 \text{ particle} / \text{m}^3 \text{ air}$  for different particle diameters). Then, the one way coupling assumption is valid.

### 3.4 Airflow pattern

In this section the capability of Code-Saturne for the prediction of airflow patterns in a 2D channel (for both laminar and turbulent flow) and a 3D duct (for turbulent flow) were validated.

### 3.4.1 Laminar channel flow

For the 2D laminar channel flow, the simulations were done for three meshes to make sure the results are independent of the number of grid points. The results showed that for laminar flow there is no difference between the airflow results obtained on the three meshes. The velocity profile obtained near exit by CFD simulation was compared with the velocity profile obtained by the theoretical equation for laminar airflow (Equation (2.34)) (White 2003). The entrance length ( $L_e$ ) and the friction coefficient at the walls ( $C_f$ ) were calculated from the simulation results and then were compared with the correlations available in the literature (White 1991, Muzychka and Yovanovich 2009).

Figure 3.3 shows the airflow velocity profiles normalized by the mean flow velocity versus the dimensionless channel width for the CFD simulation and the theoretical equation. The Mean Squared Error between CFD and theoretical results (Equation (2.36)) was calculated to be  $1.55 \times 10^{-10}$ .

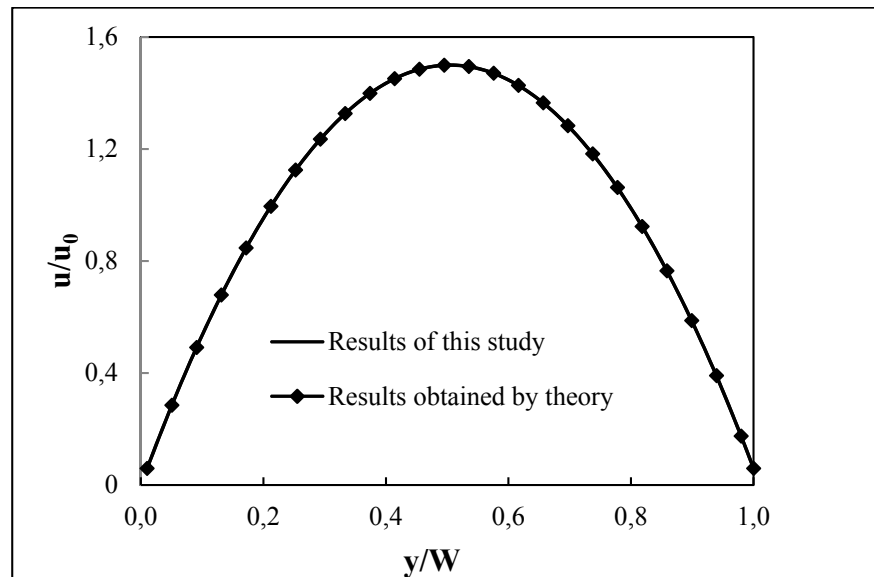


Figure 3.3 Normalized velocity profile obtained by CFD simulation with moderately dense mesh and theoretical equation along the dimensionless channel width for laminar airflow

The final asymptotic velocity value obtained by CFD simulations was 0.075 m/s where this value was calculated to be 0.074 m/s by the theoretical equation. The difference between the final velocities obtained by simulations and the theoretical equation was 1.3%. The simulation results showed that the velocity reached 99.9% of its final asymptotic value at an entrance length equal to 0.007 m (Figure 3.4). The entry length for laminar channel flow is calculated by Equation (2.37) and is equal to 0.004 m.

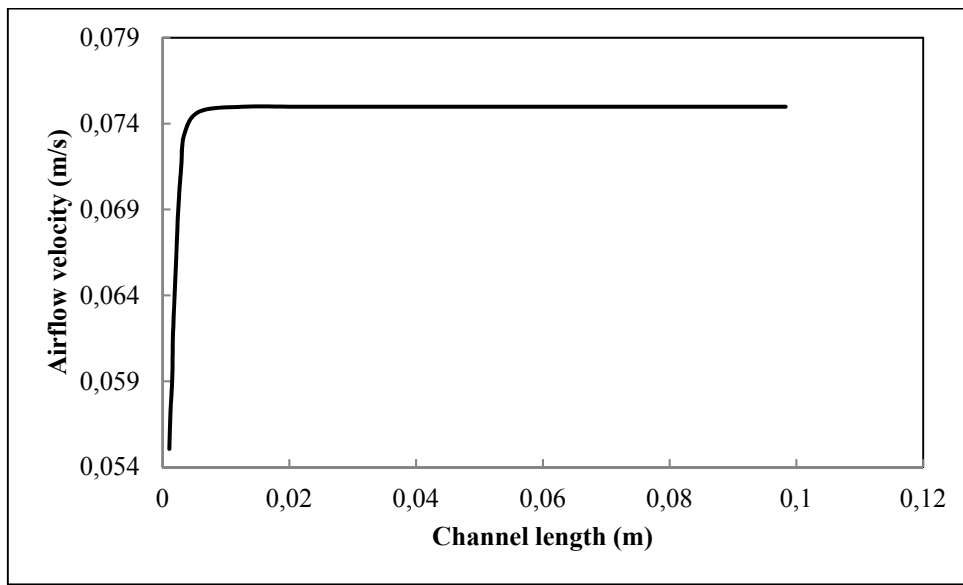


Figure 3.4 Velocity profile obtained by CFD simulation along the length of the channel at the middle of the channel for laminar airflow

The friction coefficient for developed laminar flow between parallel plates is calculated by Equation (2.39). The Reynolds number for laminar flow was calculated to be 33.3, which leads to a friction coefficient equal to 0.720. From the CFD results, the shear stress at the wall ( $\tau_w$ ) is 0.0011 N/m<sup>2</sup>. Equation (2.41) gives the friction coefficient at the walls for laminar flow. With the averaged velocity ( $U_0$ ) equal to 0.05 m/s, the value of the friction coefficient at the walls is calculated to be 0.717 which shows difference less than 0.5 % with the friction coefficient from Equation (2.41).

Comparison between friction factor values and velocity profile obtained by CFD simulation results of laminar airflow shows an excellent agreement with theory.

### 3.4.2 Turbulent channel flow

For turbulent channel flow, the simulations were done for three meshes to make sure the results are independent of the number of grid points. The results showed there are no changes between the airflow velocity results obtained by three meshes in the middle of the channel. However, there is a difference between the airflow velocity results obtained by the coarse mesh and moderately dense mesh near the walls. This difference is very small for the moderately dense and dense meshes. The computation time for the dense mesh was about 1.5 times longer than the one for the moderately dense mesh. Then, the moderately dense mesh (with 50000 cells) was selected between these three meshes Figure 3.5 shows the airflow velocity profiles obtained by the three meshes in the vicinity of the walls.

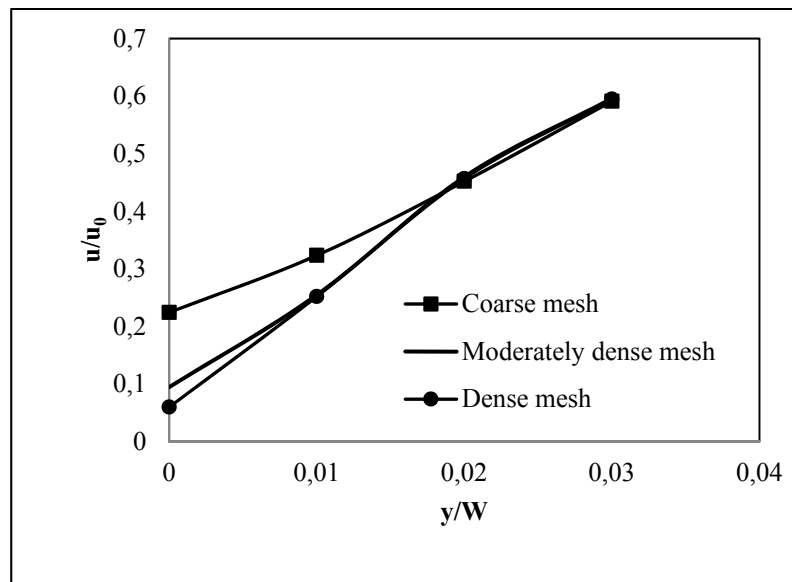


Figure 3.5 Normalized turbulent velocity profile in the vicinity of the wall obtained by three mesh sizes

Figures 3.6, 3.7 and 3.8 compare turbulent velocity profile, turbulent kinetic energy and turbulence dissipation rate profile obtained by the  $v2f$  BL- $v2/k$  turbulence model in fully developed region with the work of Tian & Ahmadi which were obtained by the  $k-\epsilon$  turbulence model (Tian and Ahmadi 2007). Our simulations were done with different levels of turbulence (1% - 10%) at the entrance to see its effect on the results. It was seen the

turbulence level has no effect on the CFD simulation results. The Mean Squared Error obtained for the velocity results of our simulations and the work of Tian & Ahmadi (Tian and Ahmadi 2007) is  $2.22 \times 10^{-3}$ . The maximum velocity at the center was obtained 5.84 m/s in this work and 5.71 m/s by the work of Tian & Ahmadi (Tian and Ahmadi 2007).

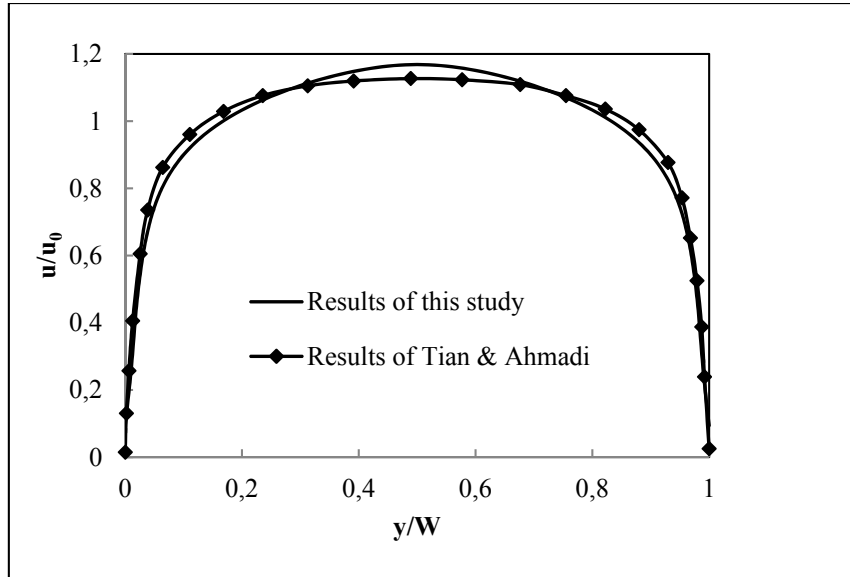


Figure 3.6 Normalized turbulent velocity profile obtained by this study and the results of Tian & Ahmadi in fully developed region versus the dimensionless channel width

The turbulence model that was used in this study predicts a lower turbulent kinetic energy and hence a lower turbulence intensity at the center of the channel. Turbulent kinetic energy at  $y = 0.01$  m is 0.073 J/kg, where in the work of Tian & Ahmadi (Tian and Ahmadi 2007) it was predicted to be 0.161 J/kg for the same Reynolds number (Figure 3.7).



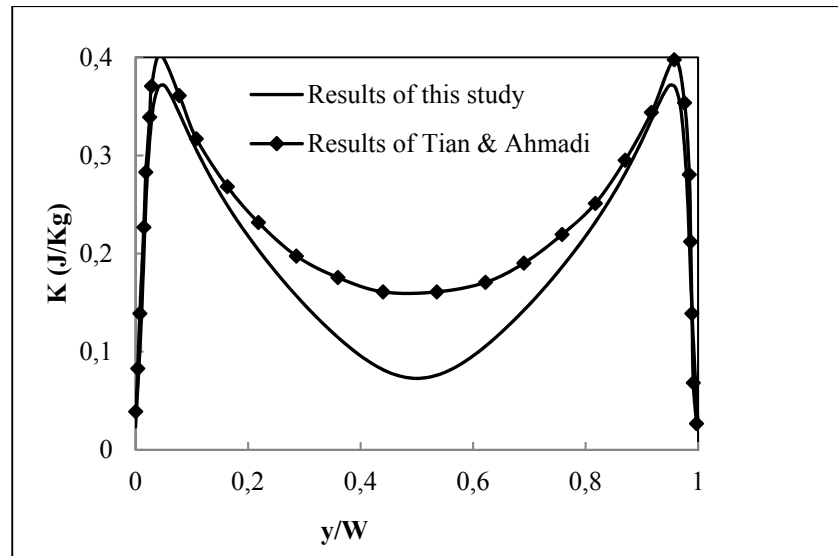


Figure 3.7 Turbulent kinetic energy obtained by this study and the results of Tian & Ahmadi in fully developed region

There is a difference between our study and the work of Tian & Ahmadi in the turbulent dissipation rate at the regions close to the walls (Figure 3.8). In this study, the maximum turbulence dissipation rate was predicted to be  $94.5 \text{ m}^2/\text{s}^3$  at  $y = 0.0006$  and  $0.0194 \text{ m}$ , while the maximum turbulence dissipation rate predicted by Tian & Ahmadi was equal to  $179.4 \text{ m}^2/\text{s}^3$  at  $y = 0.0003$  and  $0.0193 \text{ m}$  (Tian and Ahmadi 2007). The difference between the turbulent kinetic energy profiles in the center of the channel and between turbulence dissipation rate profiles near the walls could be due to the different turbulence model used for simulations.

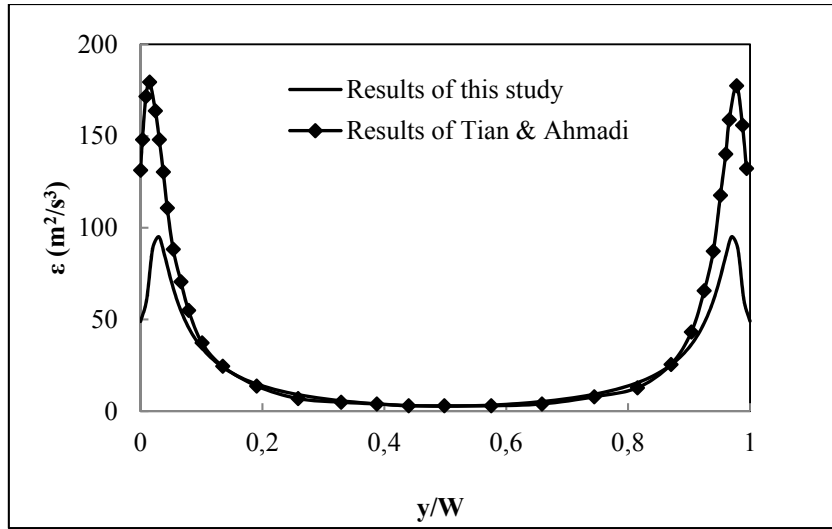


Figure 3.8 Turbulence dissipation rate profiles obtained by this study and the results of Tian & Ahmadi in fully developed region

The entrance length for turbulent flow calculated by Equation (2.38) (valid for the Reynolds number larger than 4000) is equal to 0.86 m. The simulation results showed that the entrance length is equal to 1.0 m (centerline velocity reaches 99.9% of the asymptotic value, 5.84 m/s, Figure 3.9). The predicted entrance length from the simulations is close enough to the value obtained by the empirical relation.

For the turbulent flow, the Darcy friction factor at the wall is 0.0323 (calculated by Equation (2.40)). From the CFD results, the shear stress at the wall ( $\tau_w$ ) is 0.1245 N/m<sup>2</sup>. The friction coefficient at the wall determined by Equation (2.41) with an average velocity ( $U_0$ ) of 5 m/s, is  $8.13 \times 10^{-3}$ . Then, the simulation results gave the Darcy friction factor equal to 0.0325 at the wall, which is comparable to the Darcy friction factor obtained by Equation (2.40).

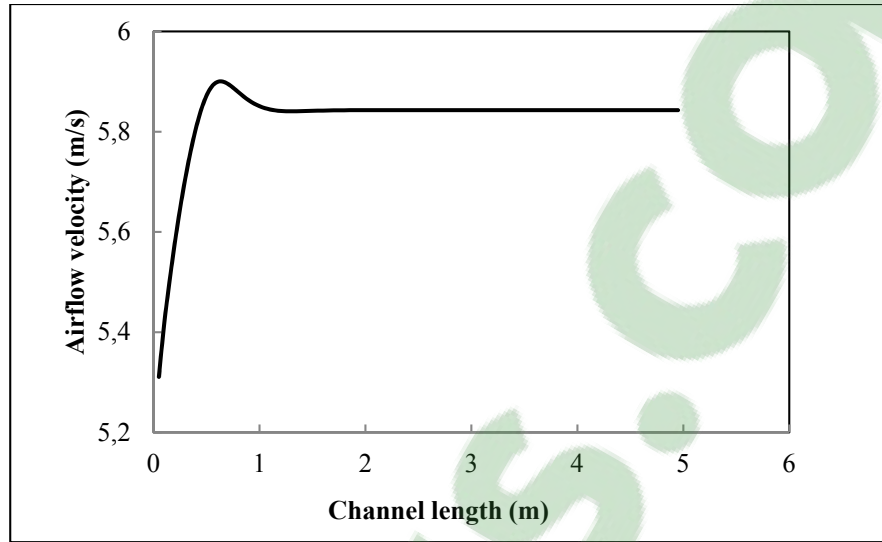


Figure 3.9 Turbulent velocity profile obtained by CFD simulation along the length of the channel at the middle of the channel

### 3.4.3 Turbulent 3D duct flow

To validate the results obtained by the  $k-\epsilon$  turbulence model for 3D duct flow, the airflow velocity profile along the middle of the duct was compared with the numerical results obtained by Yao et al (Yao, Fairweather et al. 2014). Figure 3.10 shows the airflow velocities normalized by the mean flow velocity versus the dimensionless duct width. The results of our work and the work of Yao et al. (Yao, Fairweather et al. 2014) obtained by  $k-\epsilon$  turbulence model and the Reynolds number is  $83 \times 10^3$  for both. The Mean Squared Error (MSE) obtained for the velocity results of our simulations and the work of Yao et al. (Yao, Fairweather et al. 2014) is  $2.1 \times 10^{-3}$  which is in the same order of magnitude as of the MSE calculated for 2D turbulent channel flow.

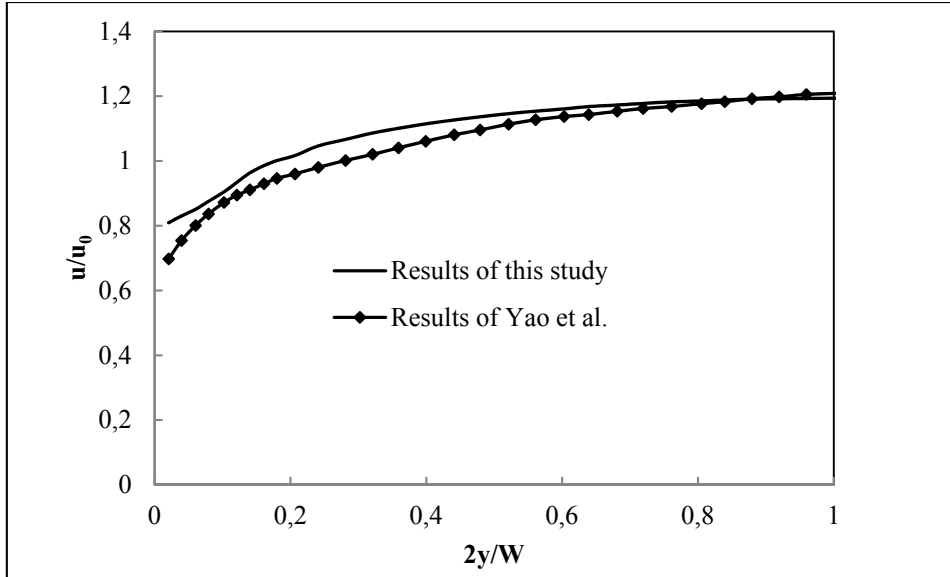


Figure 3.10 Dimensionless turbulent velocity profile obtained by this study and the results of Yao et al. versus the dimensionless duct width

### 3.5 Particle deposition

To validate the Code-Saturne capability to predict particle deposition, the non-dimensional deposition velocity ( $u_d^+$ ) of particles was compared with the empirical results of Wood (Wood 1981). Also the percentage of injected particles deposited on the channel walls for different particle diameter in the range of 0.1 to 10  $\mu\text{m}$  calculated from CFD simulation results was compared with the one obtained by an available correlation in the literature (Kulkarni, Baron et al. 2011).

#### 3.5.1 Particle deposition velocity

In this section, the non-dimensional deposition velocity ( $u_d^+$ ) of particles computed by CFD simulation is compared with the non-dimensional deposition velocity obtained by Wood equation (Wood 1981). In this study, the simulations were done for particle diameter in the range of 0.1 to 10  $\mu\text{m}$  ( $0.000634 \leq \tau^+ \leq 2.28$ ) and for two different conditions. First, the turbulent dispersion effect (Langevin effect) is considered and second, the turbulent dispersion effect on the particle trajectory is neglected.

With the shear stress at the walls ( $\tau_w$ ) obtained from CFD results and Equation (2.47), the non-dimensional particle relaxation time ( $\tau^+$ ) was calculated. Table 3.1 shows these values for each particle diameter in the range of 0.1 to 10  $\mu\text{m}$ .

Table 3.1 Calculated amount of non-dimensional particle relaxation time  $\tau^+$  for each particle diameter in the range of 0.1 to 10  $\mu\text{m}$

| Particle diameter ( $\mu\text{m}$ ) | $\tau^+$ |
|-------------------------------------|----------|
| 10                                  | 2.28     |
| 5                                   | 0.578    |
| 3                                   | 0.212    |
| 1                                   | 0.0258   |
| 0.5                                 | 0.00731  |
| 0.1                                 | 0.000634 |

The particle deposition velocity was calculated from CFD simulation results by averaging the particles velocity in gravity (y) direction over the width and the length of the channel. Non-dimensional particle deposition velocity ( $u_d^+$ ) was calculated with Equation (2.49) for each particle diameter. Figure 3.11 compares the non-dimensional particle deposition velocity versus the non-dimensional particle relaxation time which were obtained by CFD simulation results for both conditions of particle simulation (1. considering the turbulent dispersion effect and 2. neglecting the turbulent dispersion effect) with the one obtained by Wood equation (Equation (2.42)) (Wood 1981).

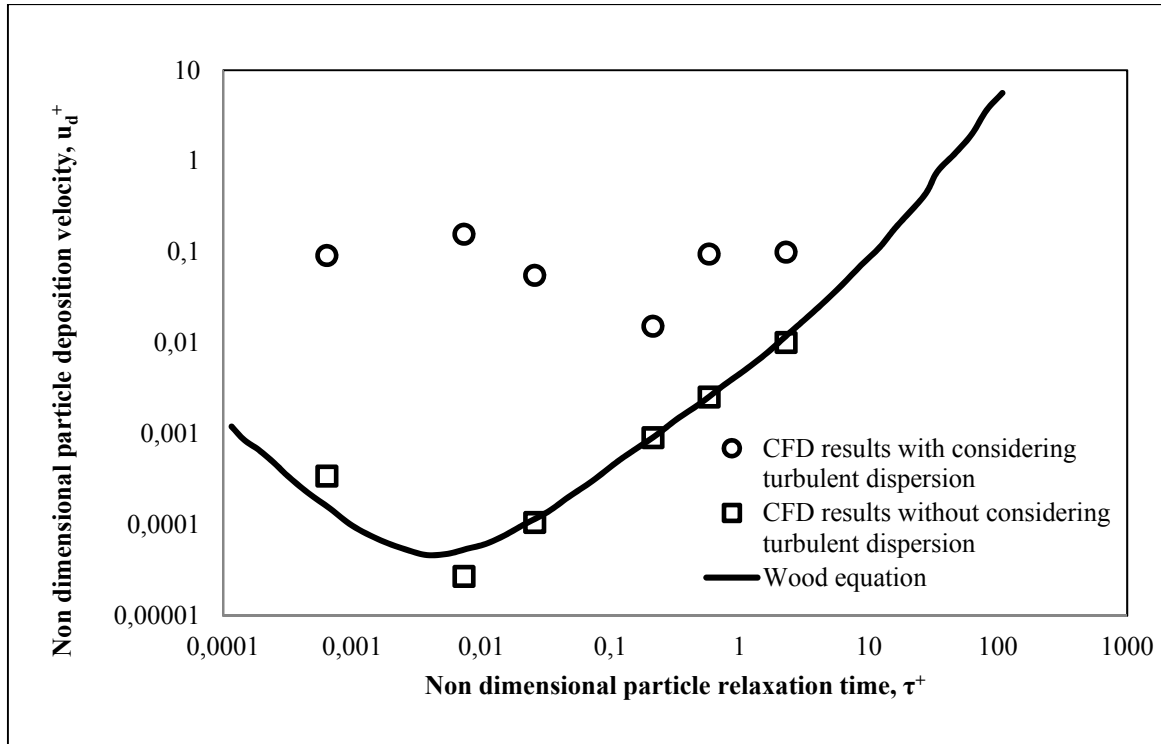


Figure 3.11 Non-dimensional particle deposition velocity versus non-dimensional particle relaxation time for particles with a diameter of 0.1 to 10  $\mu\text{m}$

Figure 3.11 shows that for this range of particle size, there is a good agreement between CFD simulation results and the results obtained by Wood (Wood 1981) when the turbulent dispersion effect is neglected. However, by considering the turbulent dispersion effect Code-Saturne overestimates the non-dimensional particle deposition velocity. It is then concluded that for Code-Saturne to obtain the acceptable results for the simulation of particles behaviour with a diameter in the range of 0.1 to 10  $\mu\text{m}$ , the turbulent dispersion effect should be neglected. Chibbaro and Minier (Chibbaro and Minier 2008) also found that for heavy particles ( $\tau^+ > 10$ ), by considering the turbulent dispersion effect, the predicted results with the CFD simulations agree very well with the experiments. While for light particles ( $\tau^+ < 10$ ), the deposition velocity is overestimated by the CFD.

### 3.5.2 Particle deposition

The percentage of the injected particles deposited on the channel surfaces was calculated from CFD simulation results for particles in the range of 0.1 to 10  $\mu\text{m}$  by neglecting the turbulent dispersion effect. The simulation results were compared with the results obtained to the available correlation for circular channels (Kulkarni, Baron et al. 2011) which predict the percentage of deposited particles on the channel surfaces as:

$$\text{Percentage of deposited particles} = 1 - (\eta_{\text{grav}}\eta_{\text{diff}}) \quad (3.1)$$

where  $\eta_{\text{grav}}$  and  $\eta_{\text{diff}}$  are obtained by Equations (2.40) and (2.50), respectively. Figure 3.12 shows the comparison results.

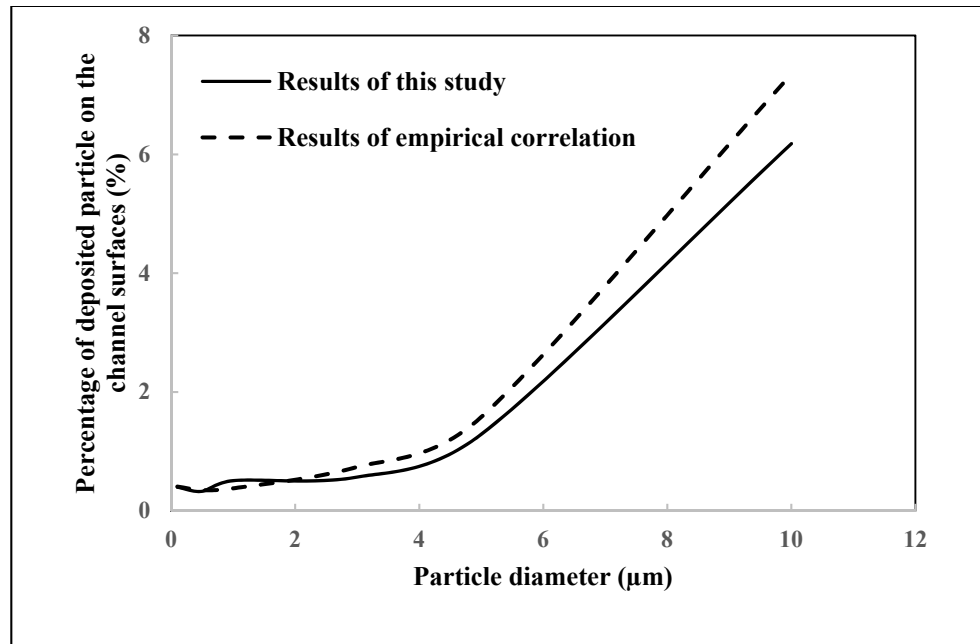


Figure 3.12 Percentage of the injected particles deposited on the channel surfaces versus the particle diameter while neglecting the Langevin effect

On Figure 3.12, the graphs show the percentage of injected particles deposited. The difference between our results and the results obtained by empirical correlation is small especially when the particle diameter is less than 3  $\mu\text{m}$ . The difference between the curves

could be due to the fact that the empirical correlations were developed for circular channel while our case is a rectangular channel.

### **3.6 Summary**

This chapter validated Code-Saturne for predicting airflow pattern and particle dispersion and deposition in a 2D channel flow. The laminar and turbulent airflow patterns predicted using Code-Saturne had an acceptable agreement with the literature. Also, by comparing the particle dispersion results, the capability of Code-Saturne in predicting the particle dispersion was validated. It is concluded that for particle diameters in the range of 0.1 to 10  $\mu\text{m}$ , the turbulent dispersion effects must be neglected and then the simulation results are in good agreement with experimental and numerical results from literatures (Wood 1981, Chibbaro and Minier 2008).



## **CHAPTER 4**

### **RESULTS AND DISCUSSION**

The objective of this chapter is to present and analyze the results obtained by our numerical simulations in order to find the most effective ventilation scenario to reduce the deposition of aerosol particles. To reach this goal, the effects of duct aspect ratio, Reynolds number and particle diameter on the deposition of particles in the ventilation duct are investigated.

First, the results of different mesh sizes are presented to choose the appropriate mesh size. Then, the airflow velocity profiles are shown. Thereafter, the particle concentration and particle velocity distributions in the duct cross section are described to better understand how particles behave in the duct system. Then, the results of particle deposition for different ventilation scenarios are presented and discussed to find the most effective ventilation scenario.

#### **4.1 The effect of the mesh size on the simulation accuracy**

As mentioned in section 2.1.2, it is important to ensure that the results are not dependent on the selected mesh since the number of grid points influences the results. On the other hand, by increasing the number of grid points, the computational time increases. The effect of the number of grid points on the results was investigated and then the coarser mesh which does not significantly affect the simulation results was selected. The mesh is considered not to affect the results if the difference between the results of particle velocity at a specific location and particle deposition of two different meshes is less than 5% (Chen, Yu et al. 2006).

In this study three meshes (coarse, moderately dense, and dense) with different number of cells were created for the duct geometry with an aspect ratio of 1. Simulations were done with these meshes for one selected scenario in which the airflow Reynolds number is  $7.36 \times 10^3$  and the particle diameter is 10  $\mu\text{m}$ . Table 4.1 shows the three mesh which were defined for the mesh study:

Table 4.1 Simulations for the mesh study

| <b>Simulations</b>  | <b>Aspect ratio</b> | <b>Reynolds number</b> | <b>Particle diameter (<math>\mu\text{m}</math>)</b> | <b>Mesh</b>  |
|---------------------|---------------------|------------------------|---|--------------|
| <b>Simulation1</b>  | 1                   | $7.36 \times 10^3$     | 10 $\mu\text{m}$                                    | 80000 cells  |
| <b>Simulation 2</b> | 1                   | $7.36 \times 10^3$     | 10 $\mu\text{m}$                                    | 160000 cells |
| <b>Simulation 3</b> | 1                   | $7.36 \times 10^3$     | 10 $\mu\text{m}$                                    | 240000 cells |

The results showed that among these three meshes, the mesh with 160000 cells was accurate enough for our study simulations (for the duct with the aspect ratio of 1). For the particle velocity comparisons, the particle velocities at three randomly selected points (point 1:  $x = 1$  m,  $y = 0.05$  m,  $z = 0.15$  m, point 2:  $x = 4$  m,  $y = 0.15$  m,  $z = 0.02$  m and point 3:  $x = 8$  m,  $y = 0.2$  m,  $z = 0.25$  m) in the duct were compared between the three meshes. The particle velocities obtained by the three meshes were the same considering 7 digits. For the deposition comparisons, the particle deposition at the duct outlet was compared between the three meshes. Figure 4.1 shows the values of the particle deposition for the three meshes. The difference in the particle deposition at the outlet between the coarse mesh and moderately dense mesh was 9.66 % while this difference between the moderately dense and dense mesh was 2.69 %. The computation time for the dense mesh was about 2 times longer than the one for the moderately dense mesh. Then, the moderately dense mesh (with 160000 cells) was selected between these three meshes.

For the aspect ratios of 2 and 4, more cells were used because of the larger widths in these two aspect ratios. The mesh used for the duct with the aspect ratio of 2 had 320000 hexahedral cells and the mesh used for the duct with the aspect ratio of 4 had 640000 hexahedral cells. Although element dimensions with a parabolic distribution were used in the width direction. The differences in the element size between the three aspect ratios both near walls and in the center of the duct were small ( $< 0.3$  %).

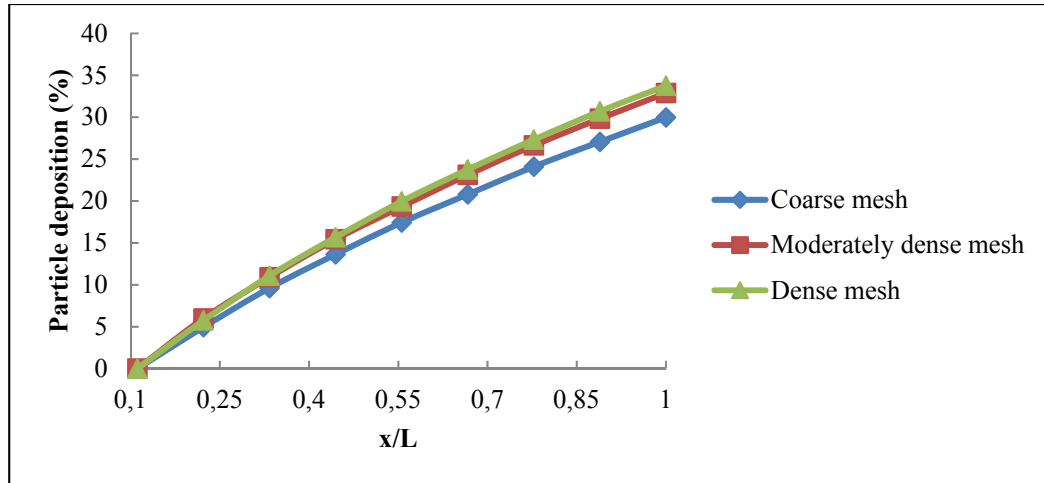


Figure 4.1 Particle deposition versus the dimensionless duct length for three different mesh size (duct aspect ratio = 1,  $Re = 7.36 \times 10^3$  and  $d_p = 10 \mu m$ )

## 4.2 Air flow pattern in the duct ventilation system

As mentioned in section 2.1.3, the fully developed airflow velocity profile was imposed at the inlet of the ventilation duct. Figures 4.2, 4.3 and 4.4 show the inserted fully developed airflow velocity profiles for the Reynolds numbers of  $7.36 \times 10^3$ ,  $15.4 \times 10^4$ , and  $36.3 \times 10^4$  for ducts with the aspect ratio of 1, 2 and 4, respectively. The equations correspond to these airflow velocity profiles are presented in appendix I.

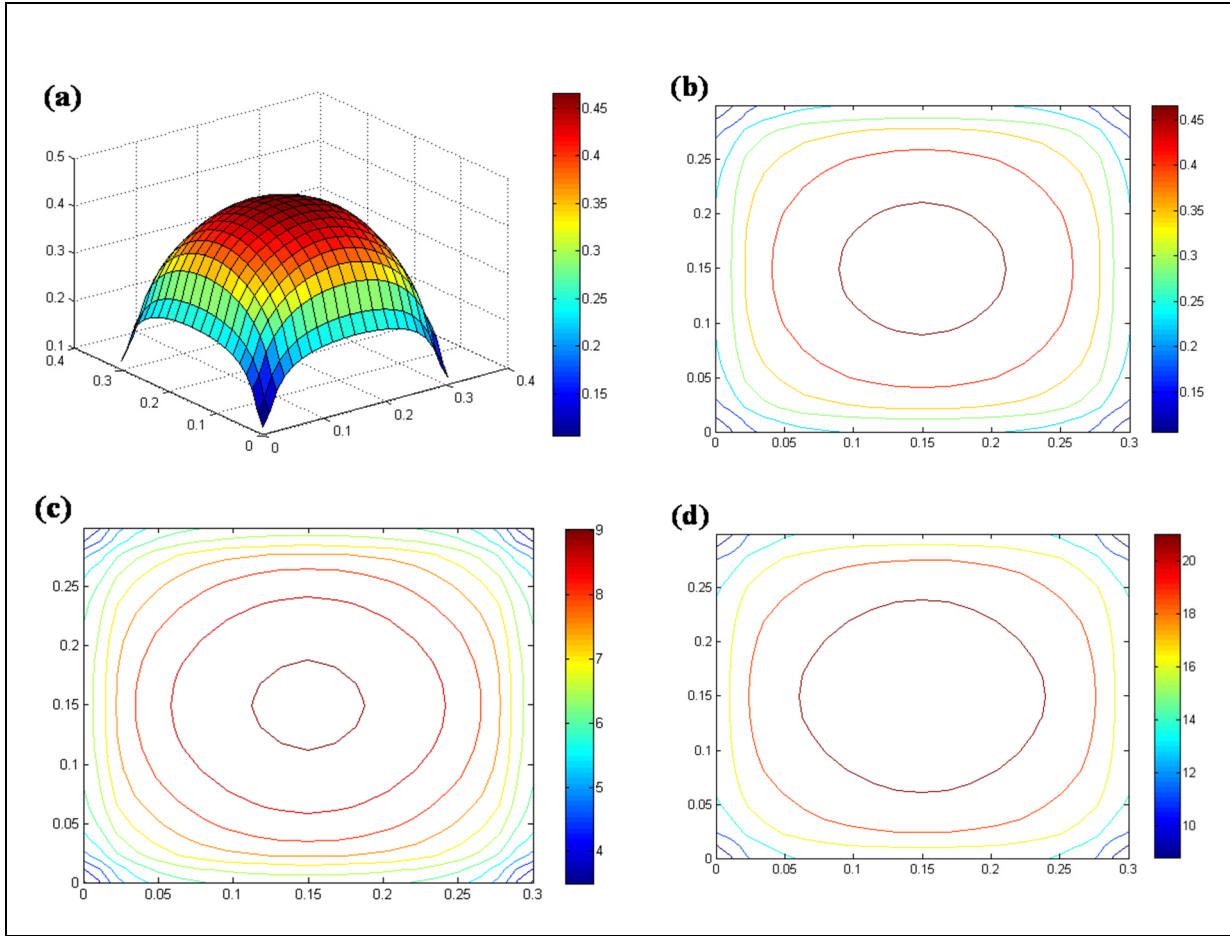


Figure 4.2 Fully developed airflow velocity profiles for the Reynolds number of  $7.36 \times 10^3$  presented as a surface plot (a) and for the Reynolds numbers of  $7.36 \times 10^3$  (b),  $15.4 \times 10^4$  (c) and  $36.3 \times 10^4$  (d) presented as contour plots for the duct with the aspect ratio of 1. The colour bars represent velocity in m/s.

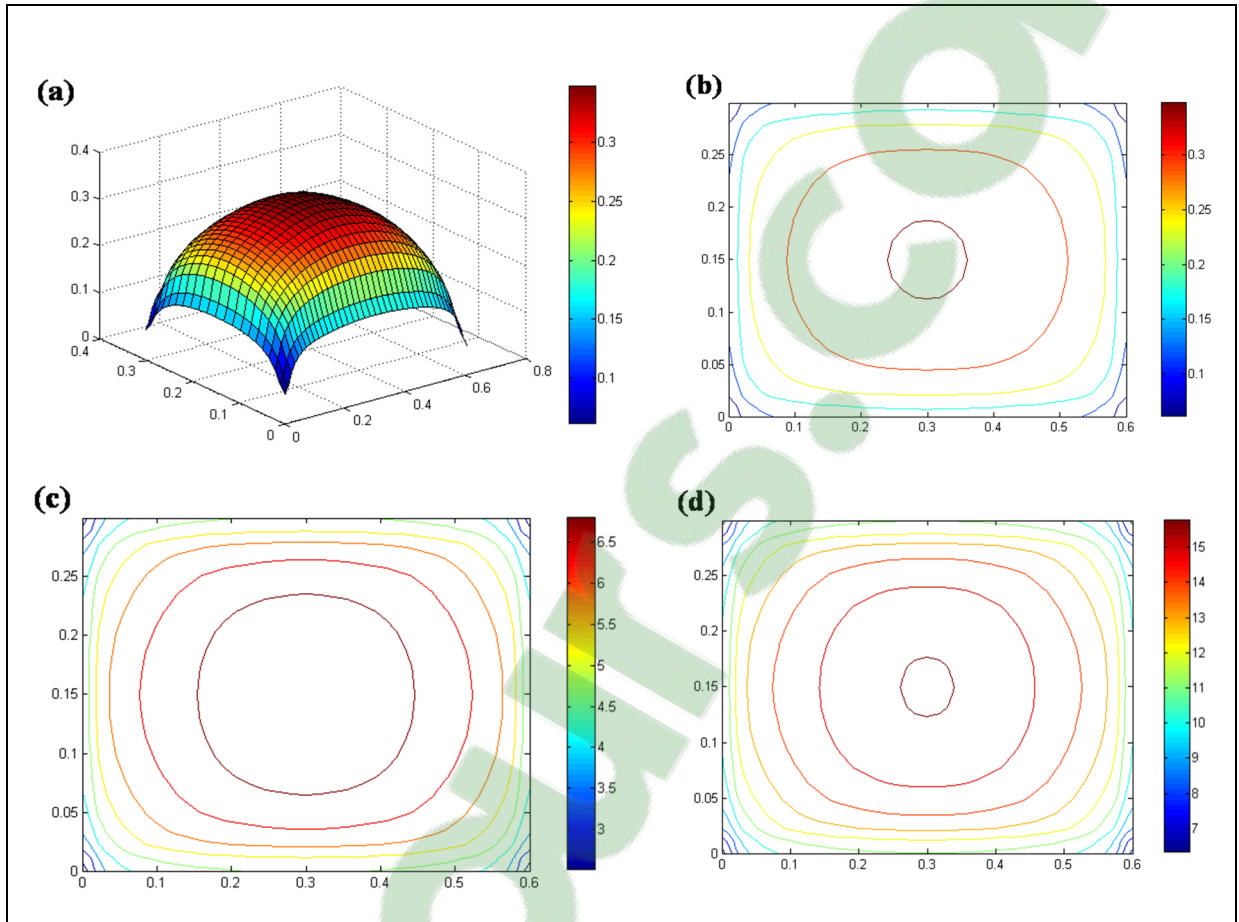


Figure 4.3 Fully developed airflow velocity profiles for the Reynolds number of  $7.36 \times 10^3$  presented as a surface plot (a) and for the Reynolds numbers of  $7.36 \times 10^3$  (b),  $15.4 \times 10^4$  (c) and  $36.3 \times 10^4$  (d) presented as contour plots for the duct with the aspect ratio of 2. The colour bars represent velocity in m/s.

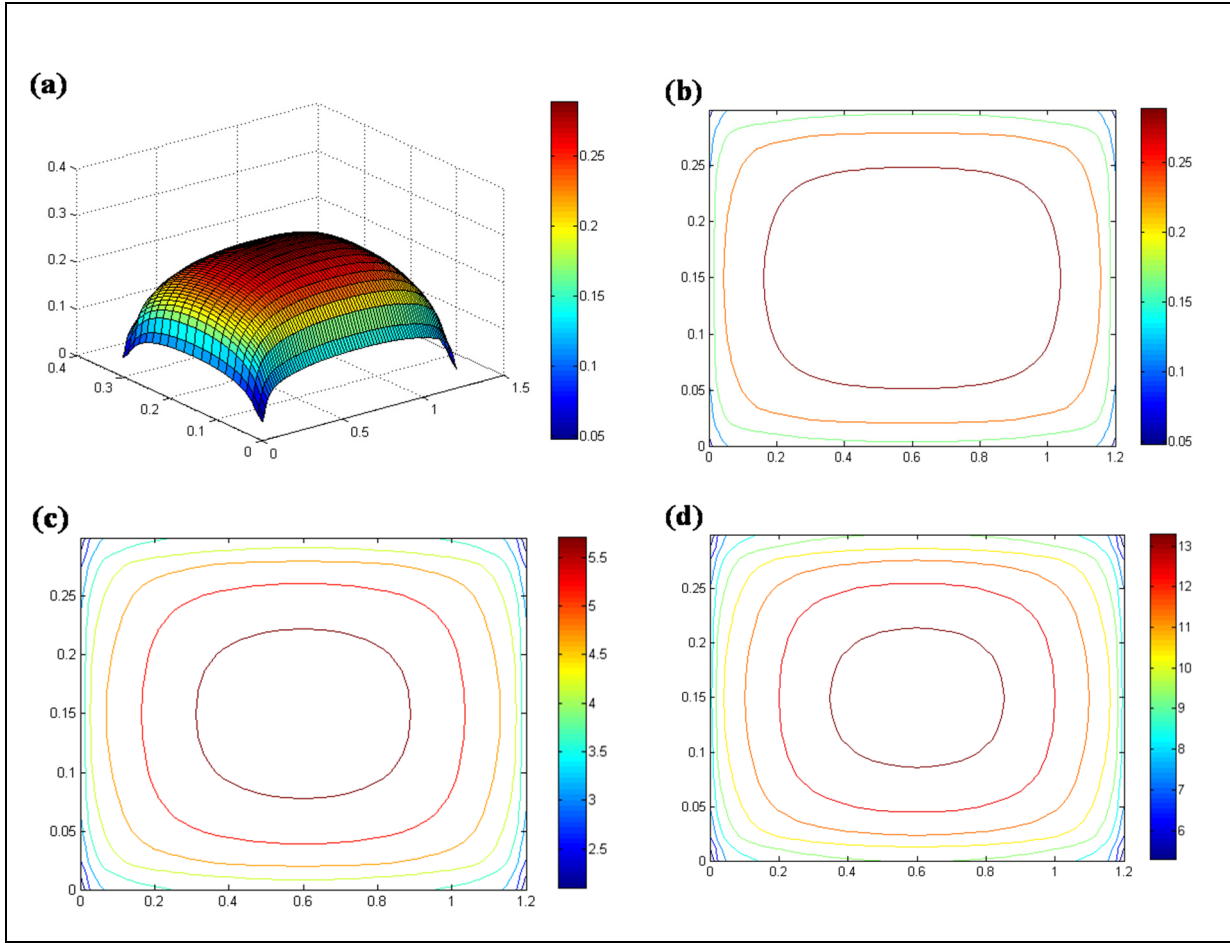


Figure 4.4 Fully developed airflow velocity profiles for the Reynolds number of  $7.36 \times 10^3$  presented as a surface plot (a) and for the Reynolds numbers of  $7.36 \times 10^3$  (b),  $15.4 \times 10^4$  (c) and  $36.3 \times 10^4$  (d) presented as contour plots for the duct with the aspect ratio of 4. The colour bars represent velocity in m/s.

### 4.3 Aerosol distribution

As mentioned in section 2.1.3, to simulate the particle deposition behaviour in the duct ventilation system,  $1.4 \times 10^5$  particles were injected from the inlet in each scenario. As particles move with the airflow, they deposit on the four walls by the diffusional deposition and on the bottom wall in the gravity direction ( $y = 0$ ) by the gravitational deposition mechanism. To better understand how particles behave in the duct system, we investigated the particle concentration and particle velocity profiles in the duct cross section at a

representative distance from the inlet for the ducts with the aspect ratios of 1 (Figures 4.5 and 4.8), 2 (Figures 4.6 and 4.9) and 4 (Figures 4.7 and 4.10) as examples.

#### 4.3.1 Particles concentration

Figures 4.5, 4.6 and 4.7 show the particle volume concentration in a representative cross section of the duct (at  $x = 8$  m) for the Reynolds number of  $7.36 \times 10^3$  and particle diameters of 1, 5 and 10  $\mu\text{m}$  for the aspect ratio of 1 (Scenarios 1, 2 and 3, Figure 4.5), 2 (Scenarios 10, 11 and 12, Figure 4.6) and 4 (Scenarios 19, 20 and 21, Figure 4.7). For all aspect ratios, when the particle diameter is 1  $\mu\text{m}$ , particle concentration is higher at the four corners of the duct (because of lower velocity close to the walls especially at four corners, there is an accumulation of particles at these corners), while particle concentration was uniform at the inlet (Figures 4.5a, 4.6a, and 4.7a). Because of the very small particle size, gravity has no significant effect on the deposition of the particles. However, by increasing the particle size to 5  $\mu\text{m}$  (Figures 4.5b, 4.6b, and 4.7b), it is seen that because of the gravity particles tend to move toward the bottom and in a small area in the upper side (in  $y$  direction) particle concentration is zero. The size of this zero particle concentration area increases when the particle diameter is 10  $\mu\text{m}$  (Figures 4.5c, 4.6c, and 4.7c). In addition, for these particle sizes the particle volume concentration is higher near the vertical walls and at the border of the zero-concentration zone and lower at the central parts of the duct and near the bottom surface.

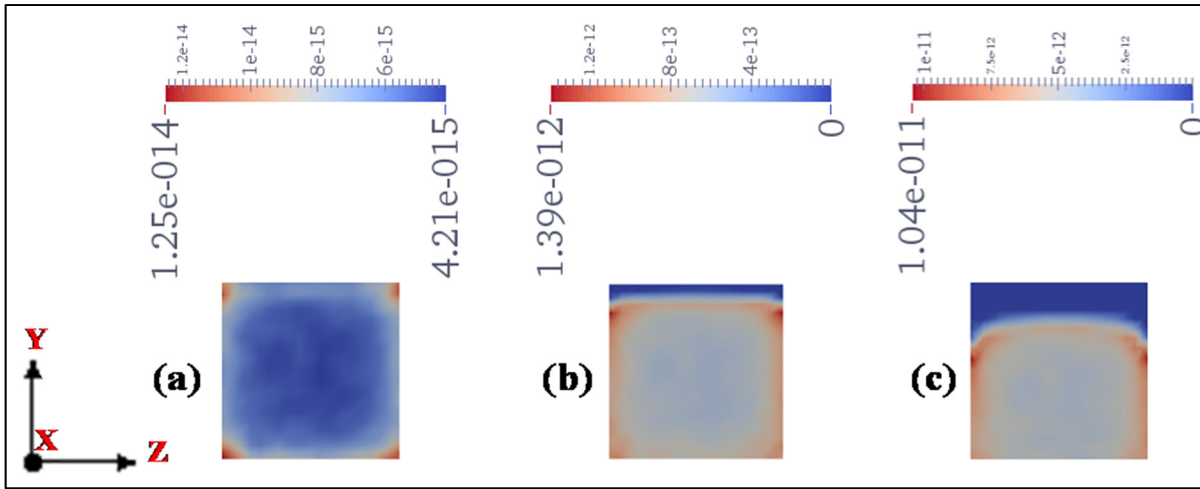


Figure 4.5 Particle volume concentrations at a cross section of the duct with the aspect ratio of 1 and Reynolds number of  $7.36 \times 10^3$  for particle diameter of 1  $\mu\text{m}$  (a), 5  $\mu\text{m}$  (b) and 10  $\mu\text{m}$  (c)

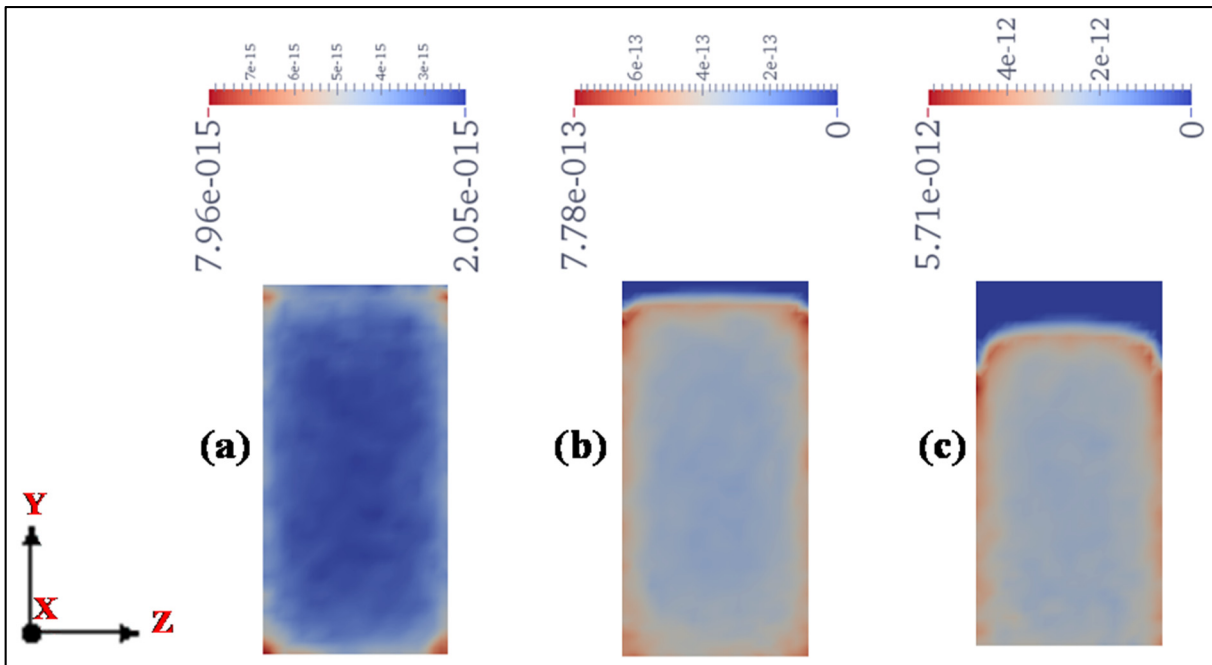


Figure 4.6 Particle volume concentrations at a cross section of the duct with the aspect ratio of 2 and Reynolds number of  $7.36 \times 10^3$  for particle diameter of 1  $\mu\text{m}$  (a), 5  $\mu\text{m}$  (b) and 10  $\mu\text{m}$  (c)



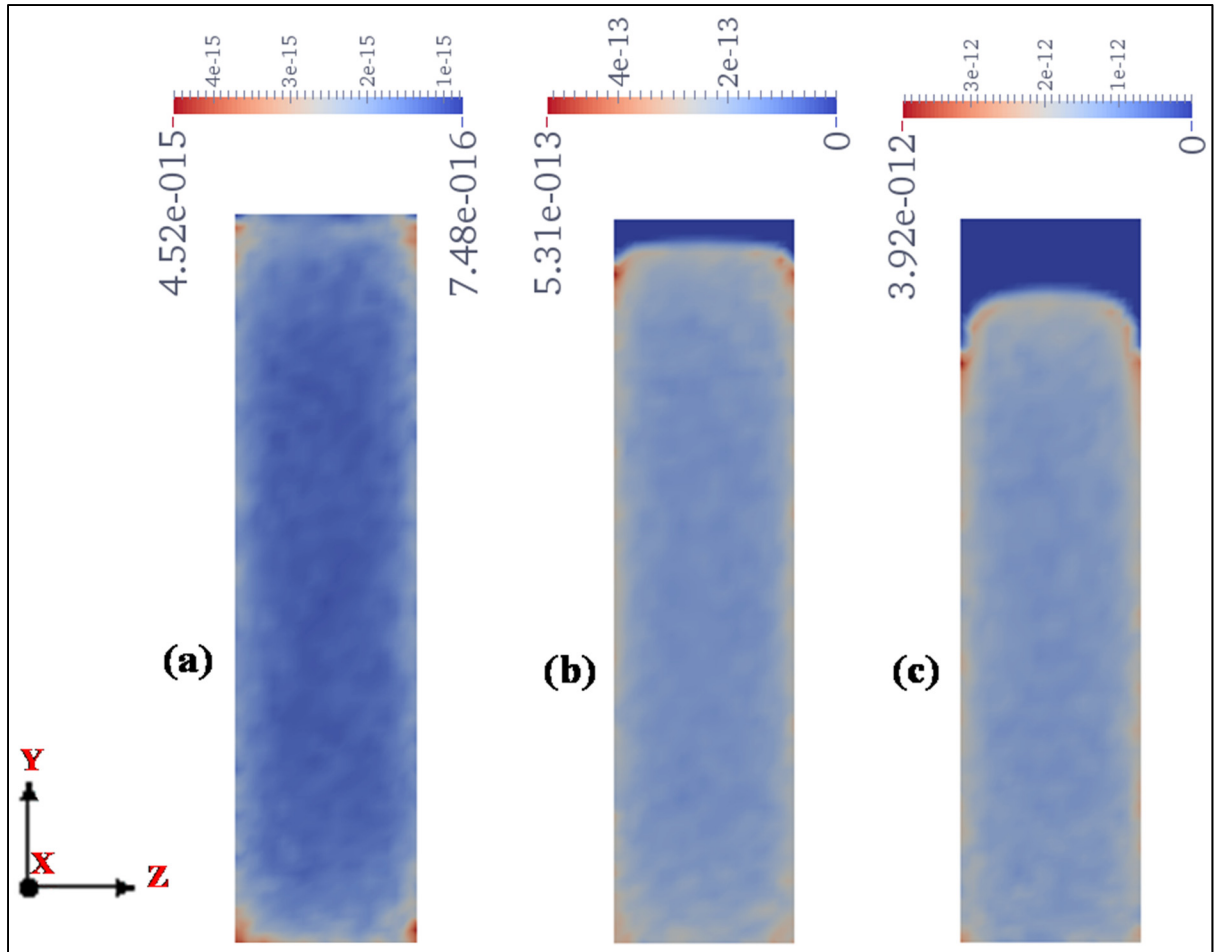


Figure 4.7 Particle volume concentrations at a cross section of the duct with the aspect ratio of 4 and Reynolds number of  $7.36 \times 10^3$  for particle diameter of 1  $\mu\text{m}$  (a), 5  $\mu\text{m}$  (b) and 10  $\mu\text{m}$  (c)

#### 4.3.2 Particles velocity

Figures 4.8, 4.9 and 4.10 show the particle velocity (in x direction) distribution in a representative cross section of the duct (at  $x = 8 \text{ m}$ ) for the Reynolds number of  $7.36 \times 10^3$  and particle diameters of 1, 5 and 10  $\mu\text{m}$  for the aspects ratio of 1 (Scenarios 1, 2 and 3, Figure 4.8), 2 (Scenarios 10, 11 and 12, Figure 4.9) and 4 (Scenarios 19, 20 and 21, Figure 4.10). For all aspect ratios, particle velocity is highest at the middle of the duct and decreases by moving toward the duct walls. In the area close to the walls, especially at four corners, particles have smaller velocity. This observation is in line with the airflow patterns (Figures

4.2, 4.3 and 4.4); for the fluid phase, we also see that velocity is maximal at the center of the channel and decreases towards walls. As particles are transported by the airflow and since we assume one-way coupling, these observations were expected. Similar to particle concentration profiles (Figures 4.5, 4.6 and 4.7), by increasing the particle diameter the effect of the gravity increases and in a small area close to the upper wall in gravity direction, particle velocity becomes zero since there is no particle in this area. This zero-velocity region increases in size with increase in the particle size.

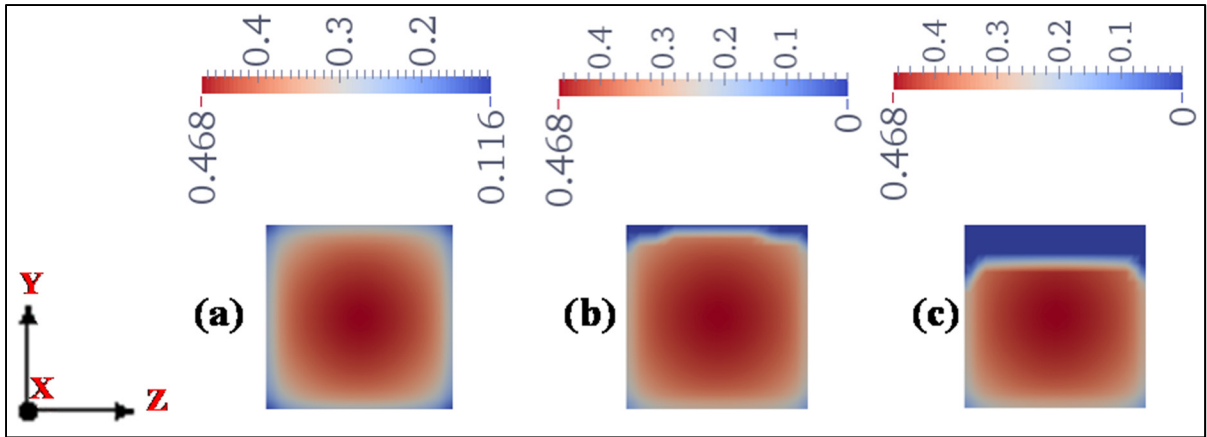


Figure 4.8 Particle velocity profile at a representative cross section of the duct with the aspect ratio of 1 and Reynolds number of  $7.36 \times 10^3$  for particle diameter of 1  $\mu\text{m}$  (a), 5  $\mu\text{m}$  (b) and 10  $\mu\text{m}$  (c)

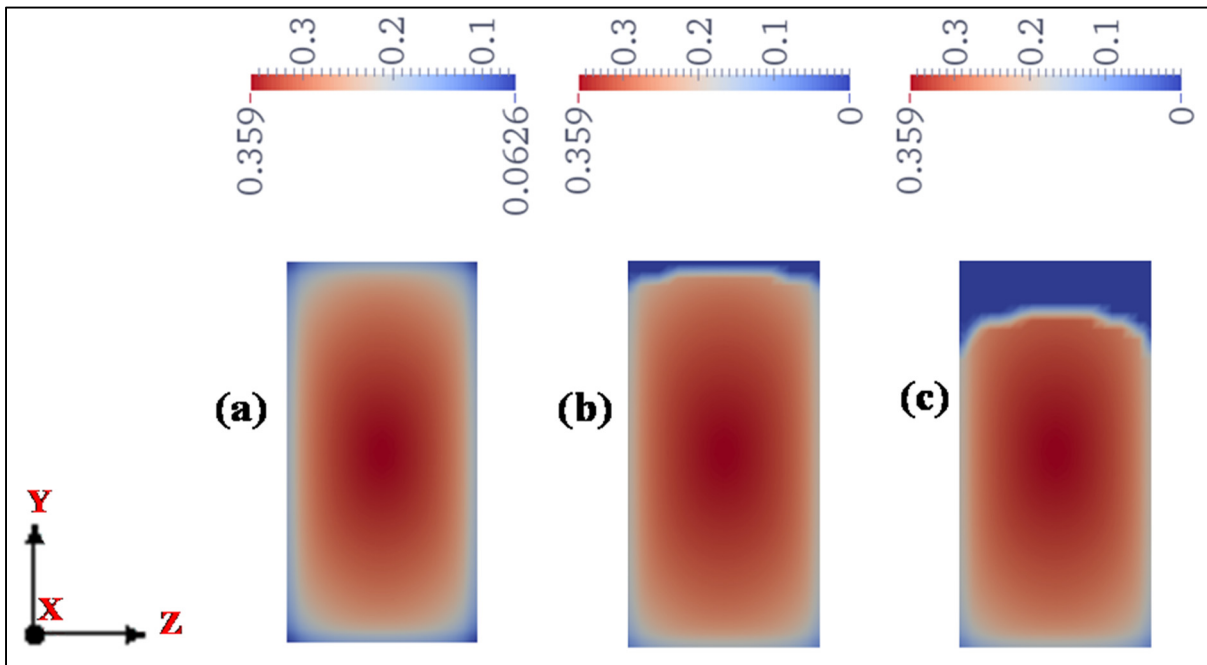


Figure 4.9 Particle velocity profile at a representative cross section of the duct with the aspect ratio of 2 and Reynolds number of  $7.36 \times 10^3$  for particle diameter of 1  $\mu\text{m}$  (a), 5  $\mu\text{m}$  (b) and 10  $\mu\text{m}$  (c)

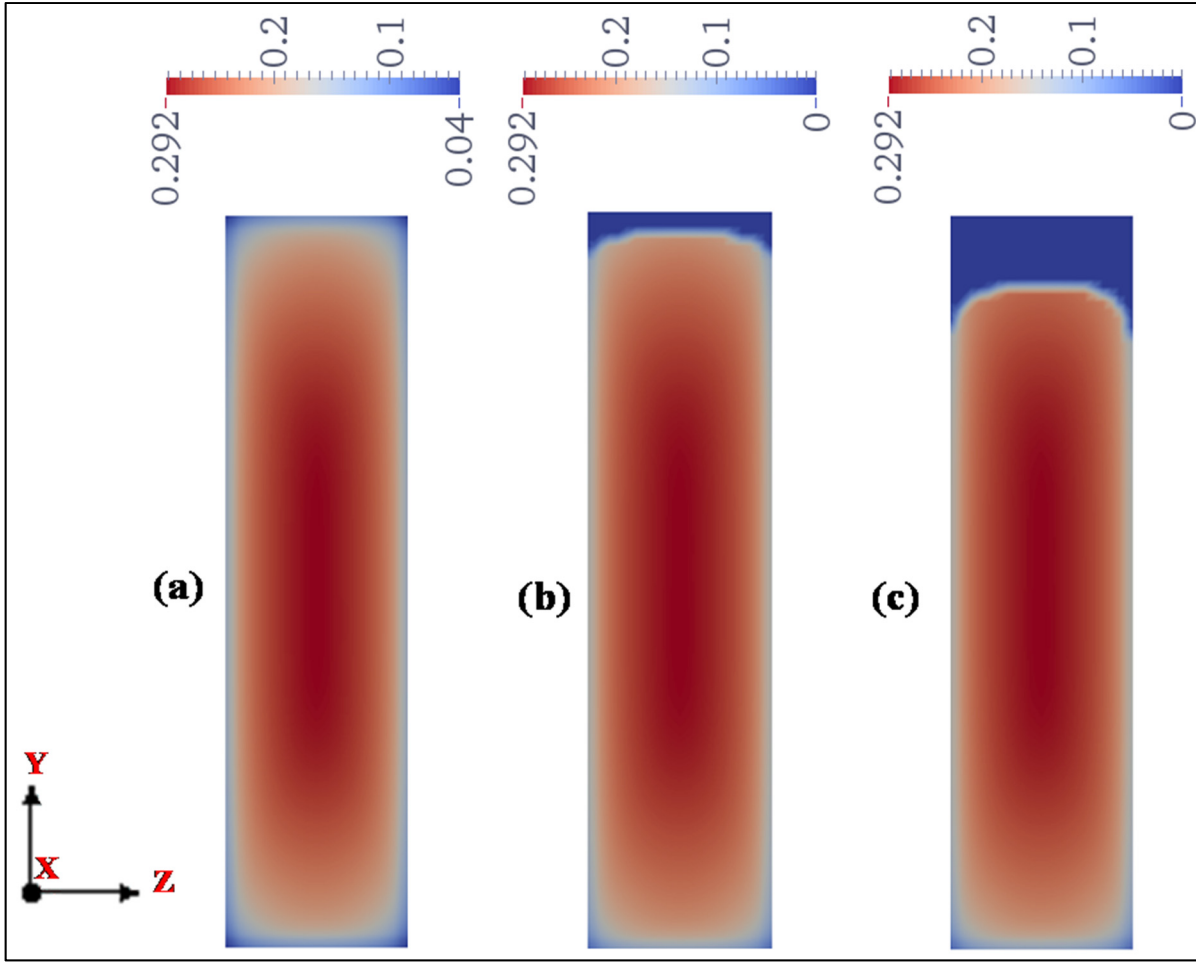


Figure 4.10 Particle velocity profile at a representative cross section of the duct with the aspect ratio of 4 and Reynolds number of  $7.36 \times 10^3$  for particle diameter of 1  $\mu\text{m}$  (a), 5  $\mu\text{m}$  (b) and 10  $\mu\text{m}$  (c)

#### 4.4 Ventilation effectiveness

The percentage of the particle that are deposited ( $100 \times (1 - \frac{\bar{c}_{x=L}}{\bar{c}_{x=1}})$ ) along the dimensionless duct length ( $x/L$ ) for different particle diameters for the Reynolds numbers of  $7.36 \times 10^3$ ,  $15.4 \times 10^4$  and  $36.3 \times 10^4$  are shown in Figures 4.11, 4.12 and 4.13, respectively. These results are presented for a duct with an aspect ratio of 1. Same behaviour is seen for the two other ducts with the aspect ratios of 2 and 4 (data not shown). For other aspect ratios, only the total deposition in the duct (obtained from the particle concentrations at inlet and outlet) is

reported and the effects of the Reynolds number, particle size, and duct aspect ratio is investigated based on the total deposition.

It is seen in Figures 4.11, 4.12, and 4.13 that as we move to the end of the duct the deposition increases because of the increased residence time of the particles in the duct. It is also observed that increasing the particle diameter increases particle deposition, and the effect is more significant at low Reynolds numbers (Figure 4.11). On the other hand, increasing the Reynolds number reduces the deposition. The effect of various parameters on the deposition rate is discussed in detail later in this chapter.

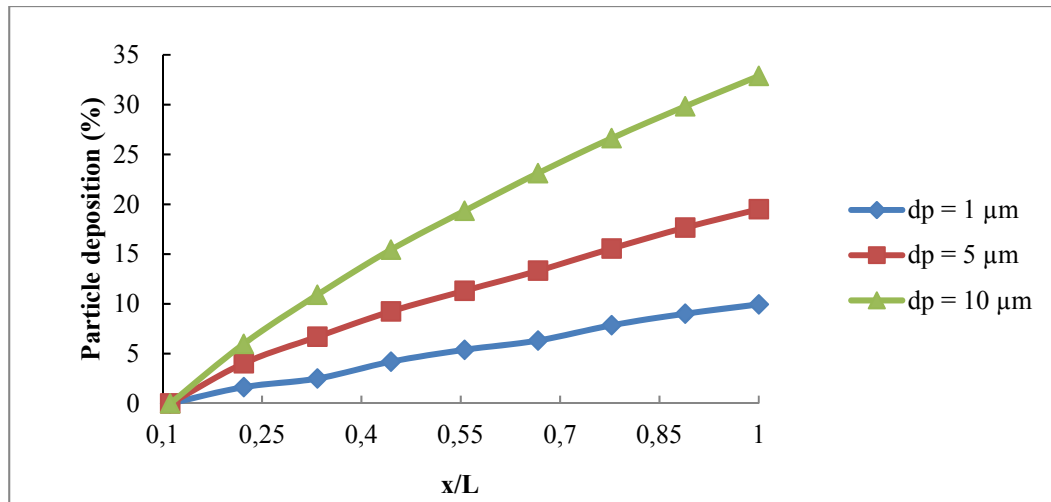


Figure 4.11 Particle deposition versus the dimensionless duct length,  
 $Re = 7.36 \times 10^3$  (duct aspect ratio = 1)

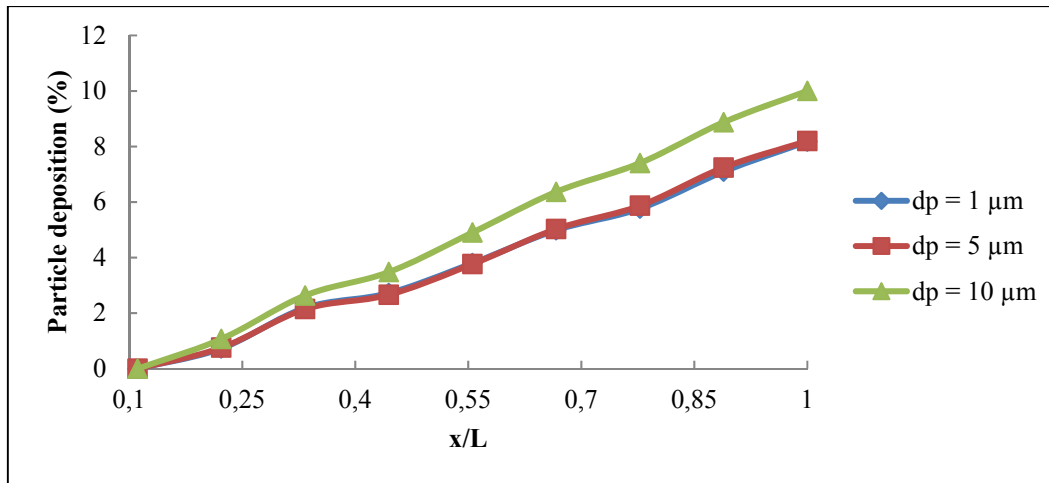


Figure 4.12 Particle deposition versus the dimensionless duct length,  
 $Re = 15.4 \times 10^4$  (duct aspect ratio = 1)

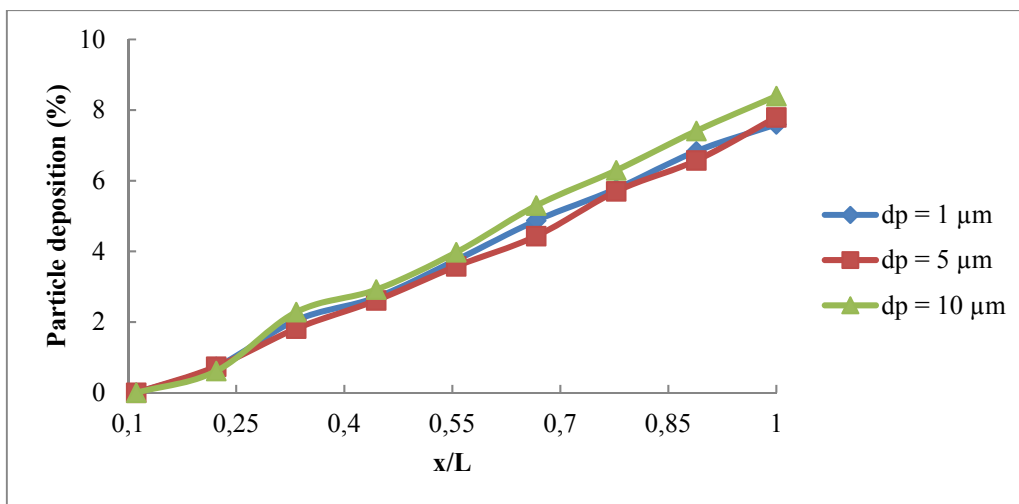


Figure 4.13 Particle deposition versus the dimensionless duct length,  
 $Re = 36.3 \times 10^4$  (duct aspect ratio = 1)

Tables 4.2, 4.3 and 4.4 show the percentage of the particles that are deposited in the duct at the end of the duct ( $100 \times (1 - \frac{\bar{c}_{x=9}}{\bar{c}_{x=1}})$ ), which is equivalent to the total deposition in the duct, for different Reynolds numbers and particle sizes for the aspect ratios of 1, 2, and 4, respectively.

From these tables, it is seen that we have the highest particle deposition (32.9 %) at a Reynolds number equal to  $7.36 \times 10^3$  and a particle diameter of  $10 \mu\text{m}$  for the aspect ratio of 1 (Scenario 3). In addition, for each aspect ratio, we have the highest deposition for the lowest Reynolds number ( $7.36 \times 10^3$ ) and largest particle diameter ( $d_p = 10 \mu\text{m}$ ). We also see general trends of increased deposition with increasing particle diameter and decreasing Reynolds number.

In the following sections, we first discuss the dominant deposition mechanisms for different Reynolds numbers and particle sizes and then investigate in detail how particle deposition is affected by the Reynolds number, particle size and duct aspect ratio.

Table 4.2 Particle deposition (%) of duct with the aspect ratio of 1

|   | $d_p = 1 \mu\text{m}$ | $d_p = 5 \mu\text{m}$ | $d_p = 10 \mu\text{m}$ |
|---|-----------------------|-----------------------|------------------------|
| <b>Re = <math>7.36 \times 10^3</math></b> | 9.95 %                | 19.5 %                | 32.9 %                 |
| <b>Re = <math>15.4 \times 10^4</math></b> | 8.17 %                | 8.21 %                | 10.1 %                 |
| <b>Re = <math>36.3 \times 10^4</math></b> | 7.59 %                | 7.79 %                | 8.39 %                 |

Table 4.3 Particle deposition (%) of duct with the aspect ratio of 2

|   | $d_p = 1 \mu\text{m}$ | $d_p = 5 \mu\text{m}$ | $d_p = 10 \mu\text{m}$ |
|---|-----------------------|-----------------------|------------------------|
| <b>Re = <math>7.36 \times 10^3</math></b> | 9.01 %                | 16.2%                 | 26.3 %                 |
| <b>Re = <math>15.4 \times 10^4</math></b> | 7.61 %                | 7.73 %                | 9.07 %                 |
| <b>Re = <math>36.3 \times 10^4</math></b> | 7.60 %                | 7.70 %                | 8.09 %                 |

Table 4.4 Particle deposition (%) of duct with the aspect ratio of 4

|   | $d_p = 1 \mu\text{m}$ | $d_p = 5 \mu\text{m}$ | $d_p = 10 \mu\text{m}$ |
|---|-----------------------|-----------------------|------------------------|
| <b>Re = <math>7.36 \times 10^3</math></b> | 9.08 %                | 14.1 %                | 21.7 %                 |
| <b>Re = <math>15.4 \times 10^4</math></b> | 7.53 %                | 7.70 %                | 8.22 %                 |
| <b>Re = <math>36.3 \times 10^4</math></b> | 7.56 %                | 7.61 %                | 7.96 %                 |

#### 4.4.1 Deposition mechanisms

As it was mentioned in section 2.4.2.2, particles deposit on the duct surfaces with two deposition mechanisms: gravitational settling and diffusional deposition. In this section we try to understand which mechanism is dominant for different Reynolds numbers and particle sizes.

Figures 4.14, 4.15 and 4.16, show the fractional contribution of each deposition mechanism in total deposition for three different particle diameters. The values of the deposition for each deposition mechanism are obtained from the theoretical equations (Equations (2.53) and (2.60)) based on our Reynolds numbers and the duct geometry with the aspect ratio of 1. From these figures, it is found that the deposition by gravity is the dominant deposition mechanism for all particle sizes and Reynolds numbers. However, it should be noticed that for the particle diameter of  $1 \mu\text{m}$  and Reynolds number of  $15.4 \times 10^4$  and  $36.3 \times 10^4$ , diffusional deposition also becomes important (still gravitational deposition is dominant), while for other particle size – Reynolds number combinations the diffusional deposition is less than 0.1% and is negligible.

Increased Reynolds number decreases the gravitational deposition because of the decreased in the residence time of the particles in the duct while settling velocity is unchanged (Equations (2.53) and (2.55)). But diffusional deposition does not significantly change with Reynolds number because with increased airflow velocity in one hand the residence time of the particles in the duct decreases but on the other hand the diffusive deposition velocity



increases (Equation (2.60)). Then, for the small particle size (diameter = 1  $\mu\text{m}$ ), in which the gravitational deposition is relatively small and comparable to the diffusional deposition (especially at high Reynolds numbers), increased Reynolds number increases the fractional contribution of the diffusional deposition (Figure 4.14), although gravitational deposition is still dominant. On the other hand, for large particle sizes (Figures 4.15 and 4.16) since diffusional deposition is already very low at all Reynolds numbers, fractional contributions of the gravitational and diffusional depositions in total deposition are not significantly affected by the Reynolds number.

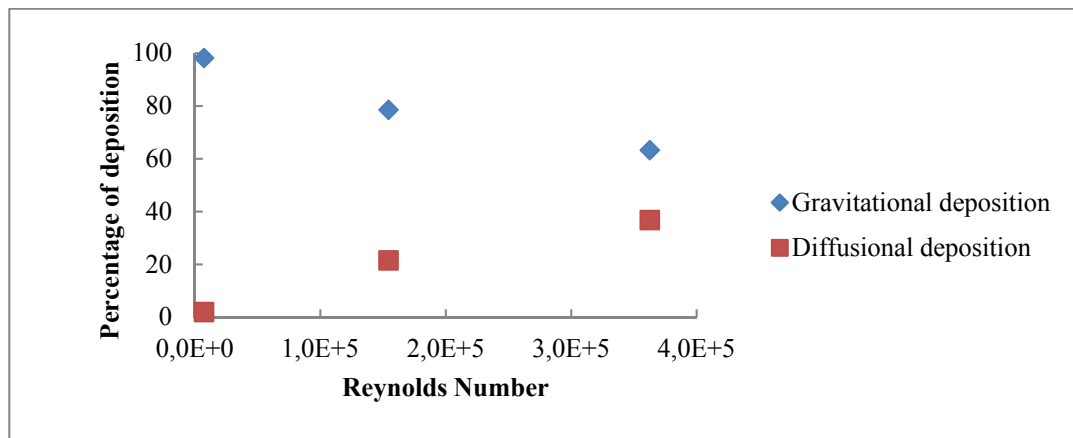


Figure 4.14 Percentage of particle deposition versus the Reynolds number for particle diameter of 1  $\mu\text{m}$  (duct aspect ratio = 1)

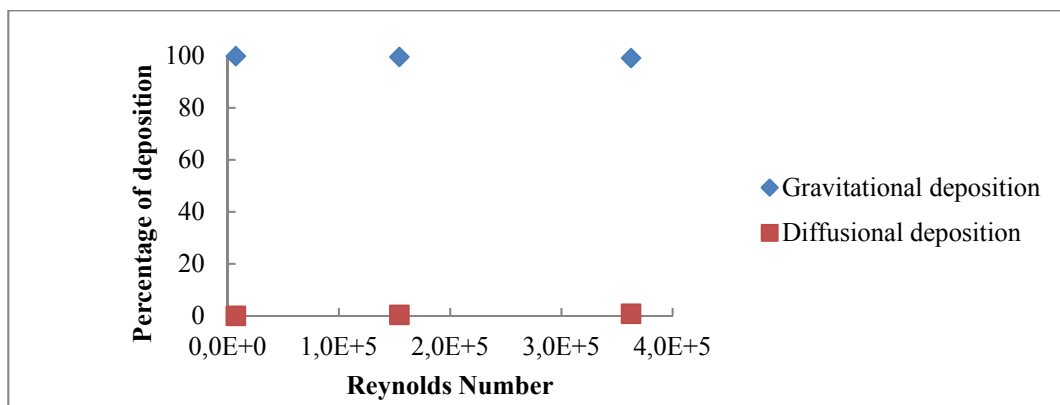


Figure 4.15 Percentage of particle deposition versus the Reynolds number for particle diameter of 5  $\mu\text{m}$  (duct aspect ratio = 1)

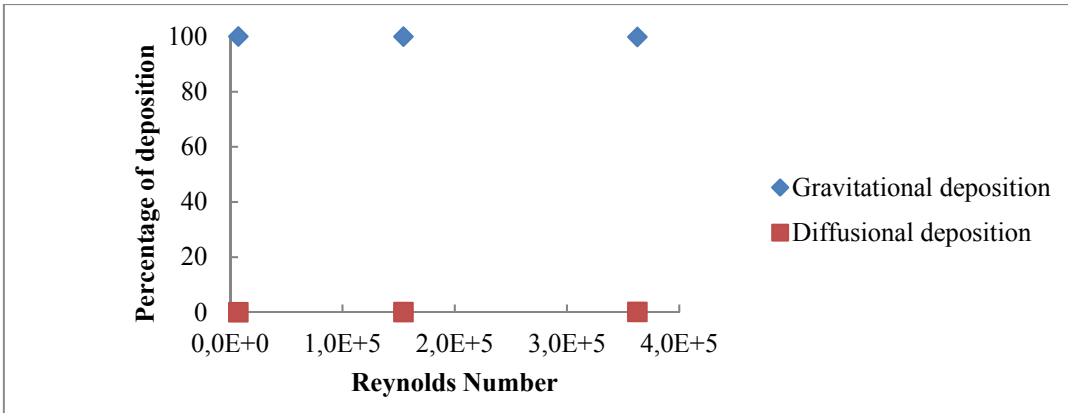


Figure 4.16 Percentage of particle deposition versus the Reynolds number for particle diameter of 10  $\mu\text{m}$  (duct aspect ratio = 1)

#### 4.4.2 The effect of the particle diameter on the particle deposition

Figures 4.17, 4.18 and 4.19 show the particle deposition in the ducts for three Reynolds numbers versus the particle diameter for ducts with different aspect ratios. For low Reynolds number ( $\text{Re} = 7.36 \times 10^3$ , Figure 4.17), it is observed that deposition increases with particle diameter for all aspect ratios, however the amount of increase becomes more significant as aspect ratio decreases (from 4 to 1). For higher Reynolds numbers ( $\text{Re} = 15.4 \times 10^4$  and  $\text{Re} = 36.3 \times 10^4$ , Figures 4.18 and 4.19), increase in particle diameter from 1  $\mu\text{m}$  to 5  $\mu\text{m}$  does not significantly change the deposition, but a further increase in diameter from 5  $\mu\text{m}$  to 10  $\mu\text{m}$  increases the deposition. Again like low Reynolds number, the effect of particle diameter is stronger for lower aspect ratios. In addition, it is observed that with increased Reynolds number, the changes in deposition with particle size become smaller, because of low deposition rates at high Reynolds numbers.

As it was mentioned in the previous section, for the Reynolds number of  $7.36 \times 10^3$ , diffusional deposition is negligible compared with the gravitational deposition for all particle sizes (Figures 4.14, 4.15, and 4.16). From Equation (2.55), it is obtained that the settling velocity is proportional to the square of the particle diameter. So increased particle diameter increases the particle deposition rate (Figure 4.17). For the Reynolds numbers of  $15.4 \times 10^4$  and  $36.3 \times 10^4$ , on the other hand, for the particle diameters of 5  $\mu\text{m}$  and 10  $\mu\text{m}$  the

diffusional deposition is negligible compared with the gravitational deposition, but for the particle diameter of  $1\text{ }\mu\text{m}$  diffusional deposition becomes comparable to the gravitational deposition and cannot be neglected anymore (although the gravitational deposition is still dominant). As already mentioned, gravitational deposition increases with the particle size because the settling velocity is larger for larger particles. But diffusional deposition decreases with particle size because an increase in the particle size decreases the particle diffusion coefficient (Equation (2.44)) and therefore the diffusive deposition velocity (Equation (2.61)). As a result, for the Reynolds numbers of  $15.4 \times 10^4$  and  $36.3 \times 10^4$  and from the particle diameter of  $1\text{ }\mu\text{m}$  to  $5\text{ }\mu\text{m}$ , since diffusional and gravitational depositions are both important and they change in opposite directions with increased particle size, the net effect is no change in total deposition with particle size (Figures 4.18 and 4.19).

For the ducts with larger aspect ratios, the width of the duct remains the same, but the height (in gravity direction) increases. As a result, the transit time of the particles until they settle at the bottom of the duct increases. Therefore, smaller fraction of the particles has enough time to settle in a duct with a larger aspect ratio, leading to lower deposition rate. This explains the lower depositions and also stronger effect of the particle diameter on deposition in ducts with larger aspect ratios (Figures 4.17, 4.18, and 4.19).

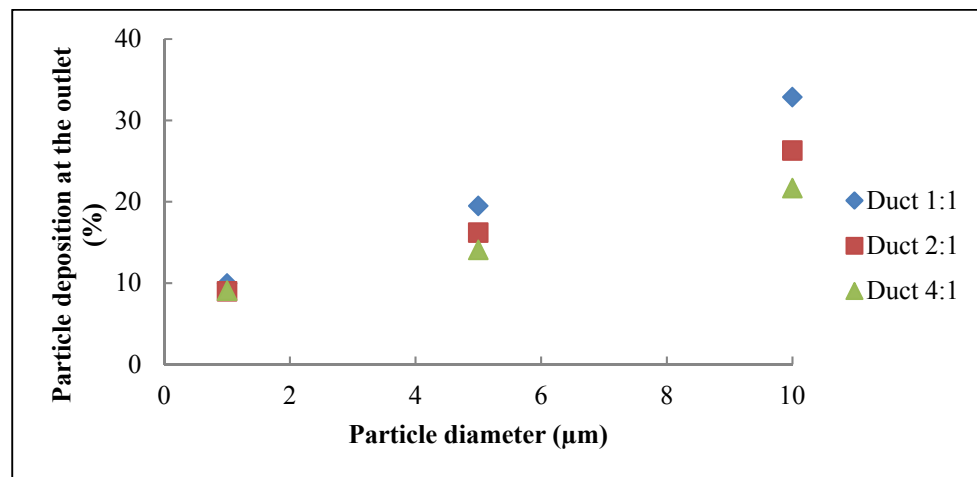


Figure 4.17 Particle deposition at the outlet versus the particle diameter for different ducts ( $\text{Re} = 7.36 \times 10^3$ )

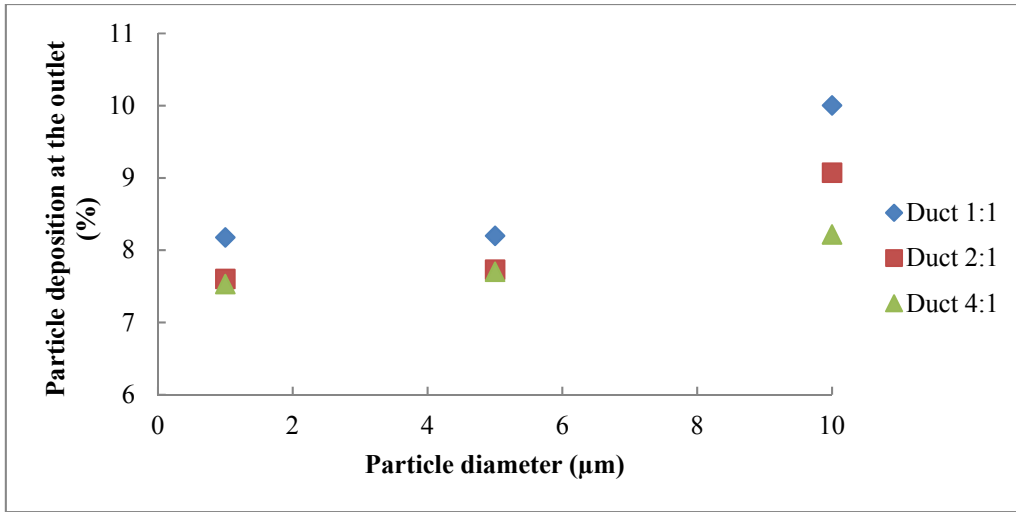


Figure 4.18 Particle deposition at the outlet versus the particle diameter for different ducts ( $Re = 15.4 \times 10^4$ )

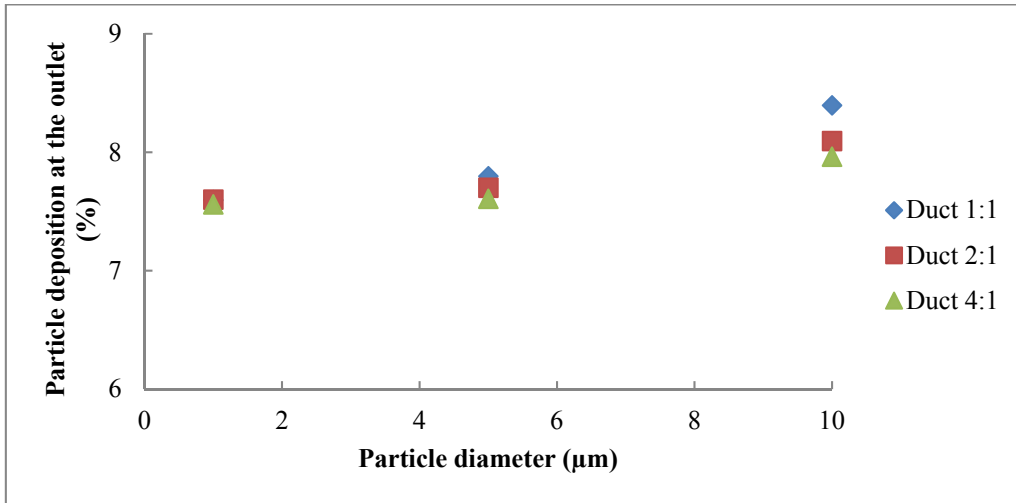


Figure 4.19 Particle deposition at the outlet versus the particle diameter for different ducts ( $Re = 36.3 \times 10^4$ )

#### 4.4.3 The effect of the Reynolds number on the particle deposition

Figures 4.20, 4.21 and 4.22, show the particle deposition at the end of the duct versus the Reynolds number for three different duct geometries. It is seen that by increasing the Reynolds number from  $7.36 \times 10^3$  to  $15.4 \times 10^4$ , particle deposition decreases significantly for all duct geometries and particle sizes. However, further increase in the Reynolds number

to  $36.3 \times 10^4$  does not significantly affect the deposition. As it was mentioned earlier, increased Reynolds number decreases the deposition by gravity mechanism because of the decreased residence time of the particles in the duct, while diffusional deposition is not significantly changed. The fact that we see a significant decrease in deposition until the Reynolds number of  $15.4 \times 10^4$ , but not afterwards is due to the exponential nature of the relationship between the gravitational deposition and airflow velocity (Equation (2.53)).

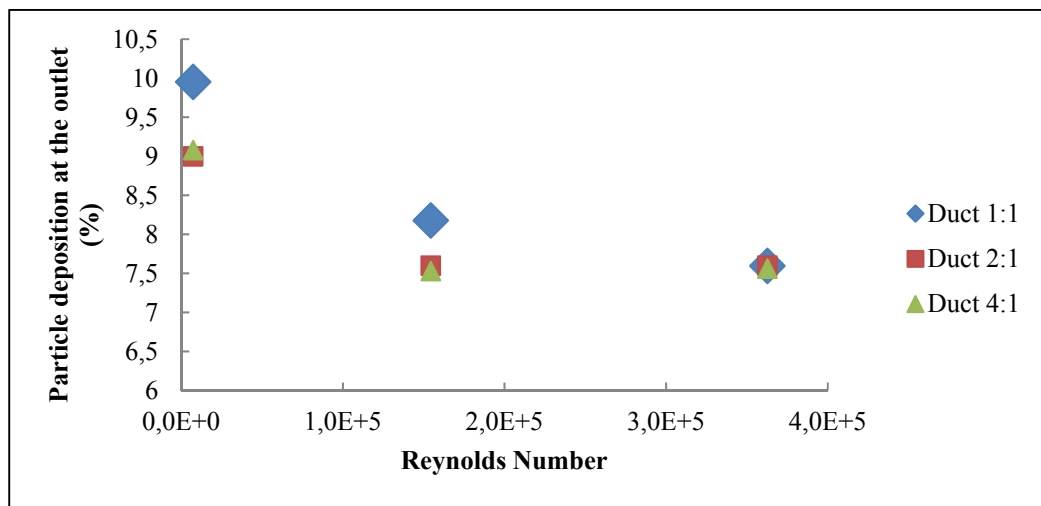


Figure 4.20 Particle deposition at the outlet versus the Reynolds number for different ducts ( $d_p = 1 \mu\text{m}$ )

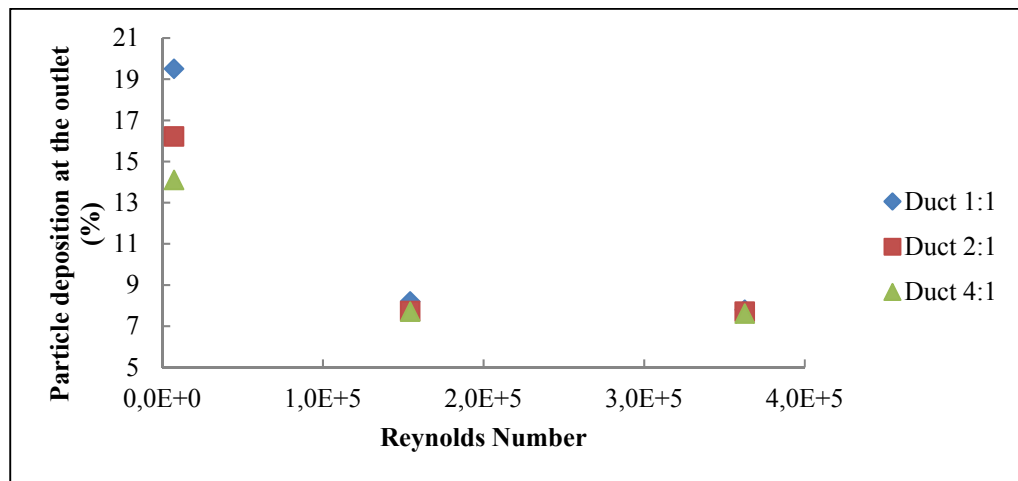


Figure 4.21 Particle deposition at the outlet versus the Reynolds number for different ducts ( $d_p = 5 \mu\text{m}$ )

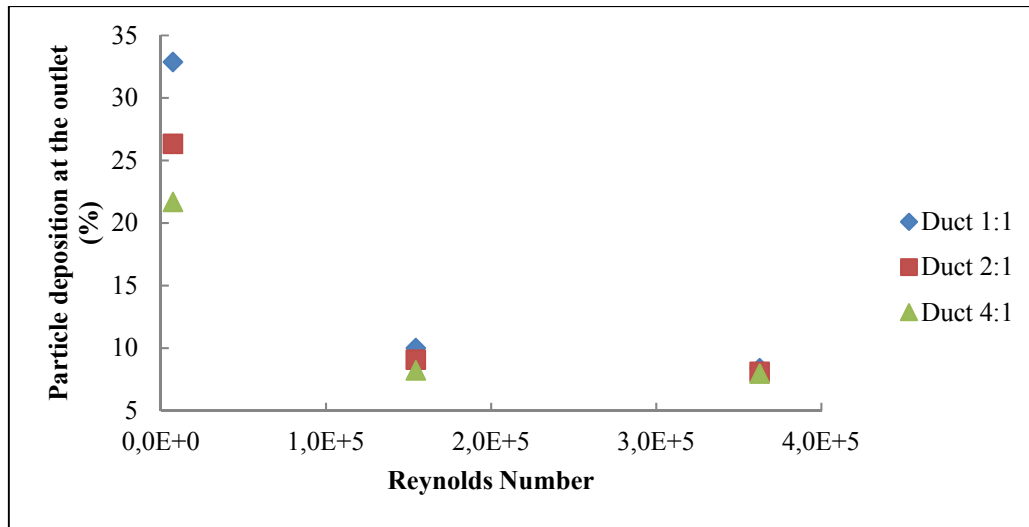


Figure 4.22 Particle deposition at the outlet versus the Reynolds number for different ducts ( $d_p = 10 \mu\text{m}$ )

#### 4.4.4 The effect of the duct geometry on the particle deposition

Figures 4.23, 4.24 and 4.25 compare the results of particle deposition for different ducts. As it is shown, increasing the duct aspect ratio (increasing the dimension of the duct in gravity direction), reduces the particle deposition. Since most of the deposition is due to the gravity, when the aspect ratio is higher, particles have to travel a longer distance to deposit on the bottom wall, leading to decreased deposition for a fixed Reynolds number and particle size.

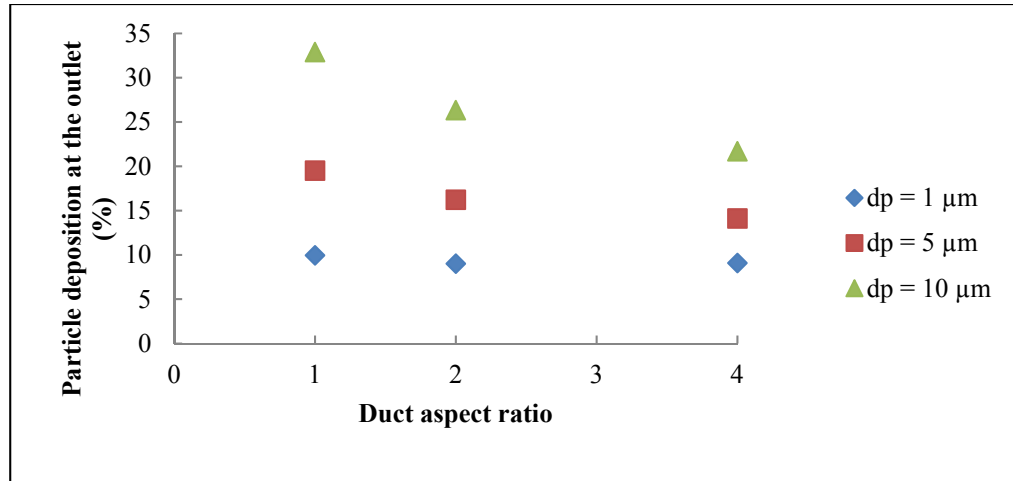


Figure 4.23 Particle deposition at the outlet versus the duct aspect ratio for different particle diameter ( $\text{Re} = 7.36 \times 10^3$ )

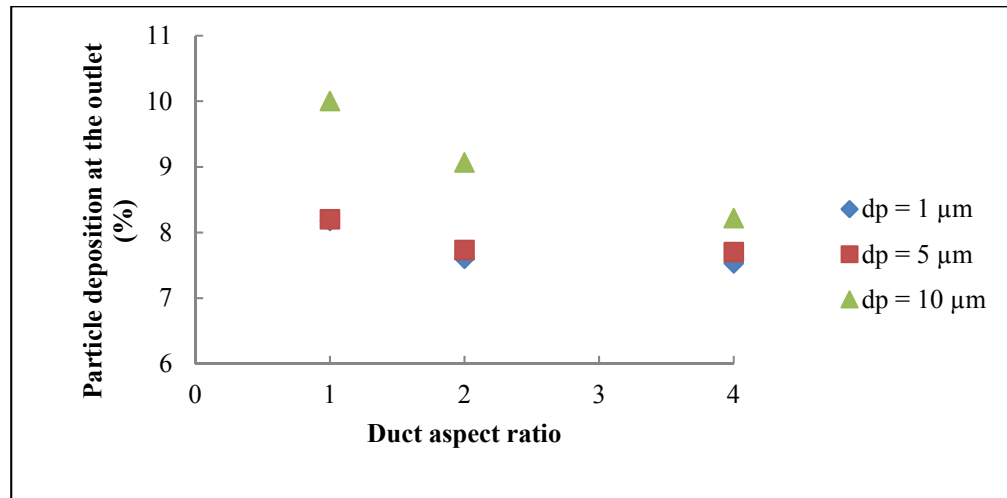


Figure 4.24 Particle deposition at the outlet versus the duct aspect ratio for different particle diameter ( $\text{Re} = 15.4 \times 10^4$ )

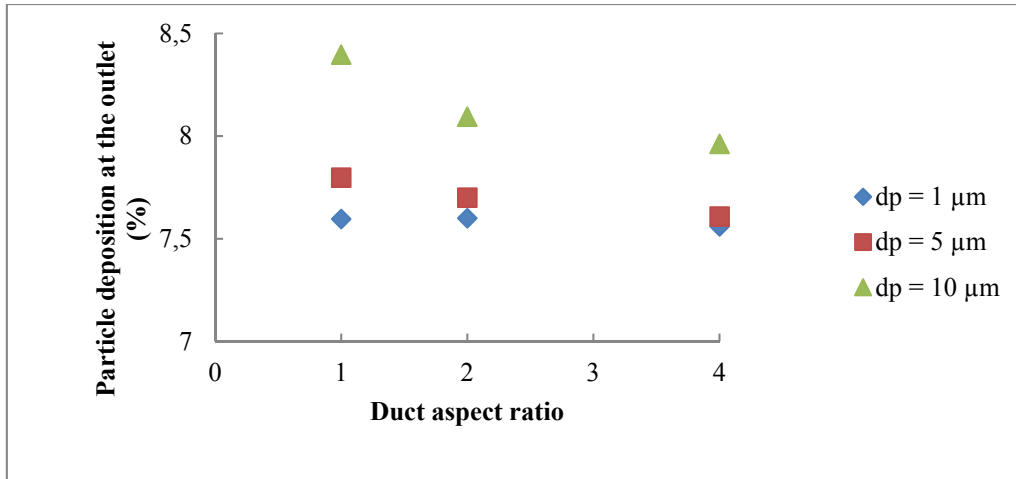


Figure 4.25 Particle deposition at the outlet versus the duct aspect ratio for different particle diameter ( $Re = 36.3 \times 10^4$ )

#### 4.5 Summary

From these simulations, it is concluded that for a given particle size, deposition can be reduced by increasing the Reynolds number (or equivalently increasing airflow as for a given duct with a specific aspect ratio, the airflow properties are constant and the Reynolds number only changes with the airflow velocity). However, while increased Reynolds number significantly decreases the deposition, after a point it does not reduce the deposition further but increases the energy cost. It is also beneficial to use a duct with larger aspect ratio (larger height, in gravity direction). In addition, when dealing with larger particles, since deposition is higher, the optimization of the ventilation system to minimize the deposition becomes more important.

For all particle diameters, the scenario with  $\alpha = 4$  and  $Re = 15.4 \times 10^4$  was found to be the most effective ventilation duct. Among the 27 defined ventilation scenarios with different duct aspect ratios, Reynolds number and particle diameter, the scenario with  $\alpha = 4$ ,  $Re = 15.4 \times 10^4$  and  $d_p = 1 \mu m$  had less particle deposition.



## CONCLUSION

Increasing use of aerosol particles in industrial applications exposes more workers to aerosol particles with potential health effects. To avoid or mitigate the health issues associated with aerosol particle dispersion in the workplace, a ventilation system is usually used to remove the contaminants from the workplace. However, the accumulation of deposited aerosol particles on the ventilation duct surfaces decreases the efficiency of the ventilation system in contaminant removal. The main objective of this study was to investigate the aerosol particles behaviour and their deposition on the surfaces of different ventilation ducts to select the most effective ventilation scenario. To achieve this goal, the effect of the duct aspect ratio, the Reynolds number and the particle diameter were investigated in order to improve the efficiency of the ventilation duct system.

The literature review (chapter 1) discussed the aerosol particles health effects and the consequence of exposure to these particles. The literature helped us to select an appropriate mathematical model together with a numerical method to simulate the particle behaviour and deposition in a ventilation duct to find the most effective ventilation scenario for the defined duct ventilation.

In chapter 2, the studied geometries, the meshes used for the simulations and the applied boundary conditions were defined. 27 ventilation scenarios were selected to study the effects of three parameters (duct aspect ratio, Reynolds number and particle diameter) on the deposition behaviour of the particles. The mathematical model for our numerical investigation was presented. The k- $\epsilon$  turbulent model and the Eulerian-Lagrangian approach were proposed as the appropriate mathematical model to simulate the airflow and aerosol particle behaviour in 3D duct flow.

In chapter 3, Code-Saturne was validated for predicting the airflow pattern in 2D laminar and turbulent channel flow by comparison with empirical correlations and numerical simulations in the literature for the velocity profile, the Darcy friction factor and the entry length. The

laminar and turbulent airflow patterns predicted using Code-Saturne had an acceptable agreement with the literature data. Also, by comparing the particle dispersion results, the capability of Code-Saturne in predicting the particle dispersion was validated. It was concluded that for small particles (particle diameters in the range of 0.1 to 10  $\mu\text{m}$ ), the turbulent dispersion effects must be neglected and then the simulation results were in good agreement with experimental and numerical results from literature.

In chapter 4, the numerical simulation results of the particle dispersion and deposition study in 3D duct flows were presented to find the most effective ventilation scenario in removing the contaminant from the room. First, the results of different mesh sizes were presented and the appropriate mesh size was selected. Then, the particle concentration and particle velocity distributions in the duct cross section were described to better understand how particles behave in the duct system. The results of particle deposition for different ventilation scenarios were also presented and discussed to find the most effective ventilation scenario.

It was concluded that for a given particle size, particle deposition can be reduced by increasing the Reynolds number. For example, for the aspect ratio of 1 increased Reynolds number from  $7.36 \times 10^3$  to  $15.4 \times 10^4$  reduced the particle deposition by 17.8%, 57.9% and 69.5% for particle diameters of 1  $\mu\text{m}$ , 5  $\mu\text{m}$  and 10  $\mu\text{m}$ , respectively, while increased Reynolds number from  $15.4 \times 10^4$  to  $36.3 \times 10^4$  reduced the particle deposition only by 7.21%, 4.88% and 16.0% for particle diameters of 1  $\mu\text{m}$ , 5  $\mu\text{m}$  and 10  $\mu\text{m}$ , respectively. However, while increased airflow Reynolds number significantly decreases the deposition, after a point it does not reduce the deposition further while increasing the cost. It was also found that it is beneficial to use a duct with larger aspect ratio (larger height, in gravity direction) to reduce the particle deposition. In addition, when dealing with larger particles, since deposition is higher, the selection of a ventilation system to minimize the deposition becomes more important. For example, for  $\text{Re} = 7.36 \times 10^3$  and  $d_p = 10 \mu\text{m}$ , the duct with the aspect ratio of 4 reduced the particle deposition by 34.0% compare to the aspect ratio of 1. Among the 27 defined ventilation scenarios with different  $\alpha$ ,  $\text{Re}$  and  $d_p$ , the scenario with  $\alpha = 4$ ,  $\text{Re} = 15.4 \times 10^4$  and  $d_p = 1 \mu\text{m}$  was found to have less particle deposition.

## APPENDIX I

### FULLY DEVELOPED INLET VELOCITY PROFILES FOR 3D TURBULENT DUCT FLOW

1. Duct aspect ratio of 1 and Reynolds number of  $7.36 \times 10^3$ :

$$0 \leq y \leq 0.3 \text{ m} \ \& \ 0 \leq z \leq 0.3 \text{ m},$$

$$u \text{ (m/s)} = 0.1064 + 3.874 \times y + 3.874 \times z - 37.85 \times y^2 + 10.47 \times y \times z - 37.85 \times z^2 + 166.5 \times y^3 - 34.93 \times y^2 \times z - 34.93 \times y \times z^2 + 166.5 \times z^3 - 278.6 \times y^4 + 0.08596 \times y^3 \times z + 116.5 \times y^2 \times z^2 + 0.07594 \times y \times z^3 - 278.6 \times z^4 + 2.784 \times y^5 - 0.01664 \times y^4 \times z - 0.2475 \times y^3 \times z^2 - 0.2449 \times y^2 \times z^3 - 0.00191 \times y \times z^4 + 2.786 \times z^5$$

2. Duct aspect ratio of 1 and Reynolds number of  $15.4 \times 10^4$ :

$$0 \leq y \leq 0.3 \text{ m} \ \& \ 0 \leq z \leq 0.3 \text{ m},$$

$$u \text{ (m/s)} = 3.499 + 62.95 \times y + 62.95 \times z - 566.7 \times y^2 + 17.06 \times y \times z - 566.7 \times z^2 + 2382 \times y^3 - 57.02 \times y^2 \times z - 57.02 \times y \times z^2 + 2382 \times z^3 - 3985 \times y^4 - 0.2026 \times y^3 \times z + 192.1 \times y^2 \times z^2 - 0.2026 \times y \times z^3 - 3985 \times z^4 + 36.01 \times y^5 + 2.445 \times y^4 \times z - 4.285 \times y^3 \times z^2 - 4.285 \times y^2 \times z^3 + 2.445 \times y \times z^4 + 36.01 \times z^5$$

3. Duct aspect ratio of 1 and Reynolds number of  $36.3 \times 10^4$ :

$$0 \leq y \leq 0.3 \text{ m} \ \& \ 0 \leq z \leq 0.3 \text{ m},$$

$$u \text{ (m/s)} = 8.81 + 141.2 \times y + 141.2 \times z - 1253 \times y^2 - 26.03 \times y \times z - 1253 \times z^2 + 5220 \times y^3 + 86.28 \times y^2 \times z + 86.28 \times y \times z^2 + 5220 \times z^3 - 8735 \times y^4 + 1.075 \times y^3 \times z - 284.5 \times y^2 \times z^2 + 1.075 \times y \times z^3 - 8735 \times z^4 + 83.8 \times y^5 + 2.785 \times y^4 \times z - 8.758 \times y^3 \times z^2 - 8.758 \times y^2 \times z^3 + 2.785 \times y \times z^4 + 83.8 \times z^5$$

4. Duct aspect ratio of 2 and Reynolds number of  $7.36 \times 10^3$ :

$$0 \leq y \leq 0.6 \text{ m} \ \& \ 0 \leq z \leq 0.3 \text{ m},$$

$$u \text{ (m/s)} = 0.06184 + 1.776 \times y + 3.032 \times z - 9.73 \times y^2 + 5.496 \times y \times z - 30.92 \times z^2 + 22.59 \times y^3 - 9.167 \times y^2 \times z - 18.33 \times y \times z^2 + 138.9 \times z^3 - 18.91 \times y^4 + 0.01358 \times y^3 \times z + 30.56 \times y^2 \times z^2 + 0.02534 \times y \times z^3 - 232.4 \times z^4 + 0.09923 \times y^5 - 0.002622 \times y^4 \times z - 0.03401 \times y^3 \times z^2 - 0.0364 \times y^2 \times z^3 - 0.003169 \times y \times z^4 + 2.357 \times z^5$$

5. Duct aspect ratio of 2 and Reynolds number of  $15.4 \times 10^4$ :

$$0 \leq y \leq 0.6 \text{ m} \ \& \ 0 \leq z \leq 0.3 \text{ m},$$

$$u \text{ (m/s)} = 2.518 + 27.59 \times y + 45.23 \times z - 139.7 \times y^2 + 39.68 \times y \times z - 431.4 \times z^2 + 312.7 \times y^3 - 66.16 \times y^2 \times z - 132.4 \times y \times z^2 + 1873 \times z^3 - 261.3 \times y^4 + 0.03136 \times y^3 \times z + 220.9 \times y^2 \times z^2 + 0.7782 \times y \times z^3 - 3134 \times z^4 + 0.8731 \times y^5 + 0.0789 \times y^4 \times z - 0.41 \times y^3 \times z^2 - 0.866 \times y^2 \times z^3 - 0.4317 \times y \times z^4 + 29.52 \times z^5$$

6. Duct aspect ratio of 2 and Reynolds number of  $36.3 \times 10^4$ :

$$0 \leq y \leq 0.6 \text{ m} \ \& \ 0 \leq z \leq 0.3 \text{ m},$$

$$u \text{ (m/s)} = 6.348 + 61.65 \times y + 100.2 \times z - 308.9 \times y^2 + 66.48 \times y \times z - 943.9 \times z^2 + 687.6 \times y^3 - 110.9 \times y^2 \times z - 221.9 \times y \times z^2 + 4071 \times z^3 - 574.5 \times y^4 + 0.02881 \times y^3 \times z + 370.3 \times y^2 \times z^2 + 1.399 \times y \times z^3 - 6812 \times z^4 + 1.836 \times y^5 + 0.2531 \times y^4 \times z - 1.13 \times y^3 \times z^2 - 1.49 \times y^2 \times z^3 - 0.7203 \times y \times z^4 + 62.69 \times z^5$$

7. Duct aspect ratio of 4 and Reynolds number of  $7.36 \times 10^3$ :

$$0 \leq y \leq 1.2 \text{ m} \ \& \ 0 \leq z \leq 0.3 \text{ m},$$

$$u \text{ (m/s)} = 0.04815 + 0.7941 \times y + 2.62 \times z - 2.377 \times y^2 + 2.73 \times y \times z - 26.78 \times z^2 + 2.864 \times y^3 - 2.28 \times y^2 \times z - 9.117 \times y \times z^2 + 120.5 \times z^3 - 1.202 \times y^4 + 0.006964 \times y^3 \times z + 7.602 \times y^2 \times z^2 + 0.1066 \times y \times z^3 - 201.7 \times z^4 + 0.005056 \times y^5 - 0.0006172 \times y^4 \times z - 0.01821 \times y^3 \times z^2 - 0.01869 \times y^2 \times z^3 - 0.14 \times y \times z^4 + 2.221 \times z^5$$

8. Duct aspect ratio of 4 and Reynolds number of  $15.4 \times 10^4$ :

$$0 \leq y \leq 1.2 \text{ m} \ \& \ 0 \leq z \leq 0.3 \text{ m},$$

$$u \text{ (m/s)} = 2.099 + 11.95 \times y + 35.62 \times z - 32.5 \times y^2 + 30.59 \times y \times z - 350.9 \times z^2 + 37.63 \times y^3 - 25.52 \times y^2 \times z - 102 \times y \times z^2 + 1550 \times z^3 - 15.77 \times y^4 + 0.03268 \times y^3 \times z + 85.09 \times y^2 \times z^2 + 0.01061 \times y \times z^3 - 2593 \times z^4 + 0.05764 \times y^5 - 0.003051 \times y^4 \times z - 0.08348 \times y^3 \times z^2 - 0.1485 \times y^2 \times z^3 + 0.2814 \times y \times z^4 + 24.4 \times z^5$$

9. Duct aspect ratio of 4 and Reynolds number of  $36.3 \times 10^4$ :

$$0 \leq y \leq 1.2 \text{ m} \ \& \ 0 \leq z \leq 0.3 \text{ m},$$

$$u \text{ (m/s)} = 5.3 + 26.53 \times y + 78.16 \times z - 70.67 \times y^2 + 62.01 \times y \times z - 766.2 \times z^2 + 81.08 \times y^3 - 51.73 \times y^2 \times z - 206.7 \times y \times z^2 + 3375 \times z^3 - 33.99 \times y^4 + 0.03559 \times y^3 \times z + 172.5 \times y^2 \times z^2 - 0.281 \times y \times z^3$$

$$- 5647xz^4 + 0.1263y^5 + 0.002391xy^4z - 0.141y^3z^2 - 0.2921y^2z^3 + 1.034yz^4 + 52.29z^5$$



## LIST OF REFERENCES

- Aitken, R., K. Creely and C. Tran (2004). Nanoparticles: An occupational hygiene review, Institute of Occupational Medicine.
- Allen, M. D. and O. G. Raabe (1985). "Slip correction measurements of spherical solid aerosol particles in an improved Millikan apparatus." Aerosol Sci. Tech **4**: 18.
- Baxter, L. L. (1989). Turbulent Transport of Particles. PhD thesis, Brigham Young University, Provo, Utah.
- Baxter, L. L. and P. J. Smith (1993). "Turbulent dispersion of particles: the STP model." Energy Fuels **7**(6): 8.
- Beauchêne, C., N. Laudinet, F. Choukri, J. Rousset, S. Benhamadouche, J. Larbre, M. Chaouat, M. Benbunan, M. Mimoun, J. P. Lajonchère, V. Bergeron and F. Derouin (2011). "Accumulation and transport of microbial-size particles in a pressure protected model burn unit: CFD simulations and experimental evidence." BMC Infectious Diseases **11**(1): 9.
- Béghein, C., Y. Jiang and Q. Y. Chen (2005). "Using large eddy simulation to study particle motions in a room." Indoor Air **15**: 10.
- Brooke, J. W., T. J. Hanratty and J. B. McLaughlin (1994). "Free-flight mixing and deposition of aerosols." Phys. Fluids **6**: 12.
- Brooke, J. W., K. Kontomaris, T. J. Hanratty and J. B. McLaughlin (1992). "Turbulent deposition and trapping of aerosols at a wall." Phys. Fluids **4**: 10.
- Chen, F., S. Yu and A. Lai (2006). "Modeling particle distribution and deposition in indoor environments with a new drift-flux model." atmospheric Environment **40**(2): 11.
- Cheong, K. W. (1997). "Deposition of Aerosol particles in ductwork." Applied Energy **57**(4): 9.

- Chibbaro, S. and J.-P. Minier (2008). "Langevin PDF simulation of particle deposition in a turbulent pipe flow" Journal of Aerosol Science **39**(7): 17.
- Chiou, M.C., C.H. Chiu and H.S. Chen (2011). "Modelling particle deposition from fully developed turbulent flow" Journal of Applied Mathematical Modelling **35**: 17.
- Dorogan, K. (2012). Numerical schemes for the hybrid modelling of gas-particle turbulent flows. PhD Dissertation, Aix Marseille University.
- Farrance, K. and J. Wilkinson (1990). "Dusting down suspended particles." Building services **12**.
- Faux, S., C. Tran, B. Miller, A. Jones, C. Monteiller and K. Donaldson (2003). "In vitro determinants of particulate toxicity: The dose-metric for poorly soluble dusts" Research Report 154, Norwich: Health and Safety Executive.
- Friedlander, S. and D. Pui (2004). "Emerging Issues in Nanoparticle Aerosol Science and Technology." Journal of Nanoparticle Research **6**: 8.
- Friedlander, S. K. (1977). Smoke, Dust, and Haze. New York: John Wiley & Sons.
- Fuzzi, S., U. Baltensperger, K. Carslaw, S. Decesari, H. D. v. d. Gon, M. C. Facchini, D. Fowler, I. Koren, B. Langford, U. Lohmann, E. Nemitz, S. Pandis, I. Riipinen, Y. Rudich, M. Schaap, J. G. Slowik, D. V. Spracklen, E. Vignati, M. Wild, M. Williams and S. Gilardoni (2015). "Particulate matter, air quality and climate: lessons learned and future needs." Atmospheric Chemistry and Physics **15**(14): 83.
- Hinds, W. C. (1999). Aerosol Technology: Properties, Behavior, and Measurement of Airborne Particles. Los Angeles, California, Wiley.
- Holman, J. P. (1972). Heat Transfer. New York: McGraw-Hill.
- Husseina, T., A. Wierzbickac, J. Löndahlc, M. Lazaridis and O. Hänninene (2015). "Indoor aerosol modeling for assessment of exposure and respiratory tract deposited dose." Atmospheric Environment **106**: 10.



- Jain, S. (1995). Three-Dimensional Simulation of Turbulent Particle Dispersion. PhD thesis, University of Utah, Utah.
- Kulkarni, P., P. A. Baron and K. Willeke (2011). Aerosol measurement: Principles, techniques and applications, John Wiley & sons.
- Laatikainen, T., P. Pasanen, L. Korhonen, A. Nevalainen and J. Ruuskanen (1992). "Methods for evaluating dust accumulation in ventilation ducts." Indoor Air Quality **92**: 4.
- Lakhout, A. (2011). Modélisation de la qualité de l'air dans une unité de bronchoscopie influence des stratégies de ventilation. Master's thesis, École de technologie supérieure, University of Quebec.
- Li, A. and G. Ahmadi (1992). "Dispersion and deposition of spherical particles from point sources in a turbulent channel flow." Aerosol Science and Technology **16**(4): 18.
- Litchford, R. J. and S. M. Jeng (1991). "Efficient Statistical Transport Model for Turbulent Particle Dispersion in Sprays." AIAA Journal **29**(9): 9.
- Lu, W., A. Howarth, N. Adam and S. Rifat (1996). "Modelling and measurement of airflow and aerosol particle distribution in a ventilated two-zone chamber." Building and Environment **31**(5): 7.
- McLaughlin, J. B. (1989). "Aerosol particle deposition in numerically simulated channel flow." Phys. Fluids **1**: 14.
- Méndez, C., J. S. Jose, J. Villafruela and F. Castro (2008). "Optimization of a hospital room by means of CFD for more efficient ventilation." Energy & Buildings **40**(5): 6.
- Morsi, S. A. and A. J. Alexander (1972). "An Investigation of Particle Trajectories in Two-Phase Flow Systems." Fluid Mech **55**(2): 16.
- Mörters, P. and Y. Peres (2010). Brownian Motion. Cambridge University Press, New York.

- Murakami, S., S. Kato, S. Nagano and S. Tanaka (1992). "Diffusion characteristics of airborne particles with gravitational settling in a convection-dominant indoor flow field." ASHRAE Transactions **98**(1): 16.
- Muzychka, Y. S. and M. M. Yovanovich (2009). "Pressure drop in laminar developing flow in noncircular ducts: a scaling and modeling approach." Journal of fluid engineering **131**(11): 11.
- Ounis, H., G. Ahmadi and J. McLaughlin (1991). "Brownian diffusion of submicrometer particles in the viscous sublayer." Journal of Colloid and Interface Science **143**(1): 12.
- Ounis, H., G. Ahmadi and J. B. McLaughlin (1993). "Brownian particle deposition in a directly simulated turbulent channel flow." Phys. Fluids **5**.
- Phuong, N. L. and K. Ito (2013). "Experimental and numerical study of airflow pattern and particle dispersion in a vertical ventilation duct." Building and Environment **59**: 16.
- Reinhardt, Y. and L. Kleiser (2015). "Validation of particle-laden turbulent flow simulations including turbulence modulation." Journal of fluid engineering **137**(7): 9.
- Saffman, P. (1965). "The lift on a small sphere in a slow shear flow." Journal of Fluid Mechanics **22**: 16.
- Saturne (2015). Code Saturne 4.0.0 Theory Guide, online. <http://code-saturne.org/cms/documentation>
- Schneider, T., J. Cherrie, R. Vermeulen and H. Kromhout (2000). "Dermal Exposure Assessment." Annals of Occupational Hygiene **44**: 7.
- Sen, D., H. Wolfson and M. Dilworth (2002). "Lead exposure in scaffolders during refurbishment construction activity-an observational study." Occupational Medicine **52**(1): 6.

- Sivier, S., E. Loth, J. Baum and R. Löhner (2005). "Eulerian-Eulerian and Eulerian-Lagrangian methods in two phase flow." Lecture Notes in Physics **414**: 5.
- Stanley, N. J. (2010). The Fate of Airborne Nanoparticles Released from a Leak in a Nanoparticle Production Process into a Simulated Workplace Environment, Degree of Doctor of Philosophy, University of Minnesota.
- Tang, Y. and B. Guo (2011). "Computational fluid dynamics simulation of aerosol transport and deposition." Frontiers of Environmental Science & Engineering **5**(3): 16.
- Tian, L. and G. Ahmadi (2007). "Particle deposition in turbulent duct flows-comparisons of different model predictions." Journal of Aerosol Science **38**(4): 211.
- Tran, C., D. Buchanan, R. Cullen, A. Searl, A. Jones and K. Donaldson (2000). "Inhalation of poorly soluble particles II. Influence of particle surface area on inflammation and clearance." Inhalation Toxicology **12**(12): 14.
- Turiel, I. (1985). Indoor Air Quality and Human Health. Stanford University Press, Stanford, California.
- Uijtewaal, W. S. J. and R. V. A. Oliemans (1996). "Particle dispersion and deposition in direct numerical and large eddy simulations of vertical pipe flows." Phys. Fluids **8**: 15.
- Wang, Q. and K. D. Squires (1996a). "Large eddy simulation of particle-laden turbulent channel flow." Phys. Fluids **8**: 17.
- Wang, Q. and K. D. Squires (1996b). "Large eddy simulation of particle deposition in a vertical turbulent channel flow." International Journal of Multiphase Flow **22**(4): 17.
- Wang, W. (1989). "Two phase flow. Beijing: Press of Water Conservancy and Electric Power." China Water & Power Press.
- White, F. M. (1991). Viscous Fluid Flow. New York: McGraw-Hill.

White, F. M. (2003). Fluid Mechanics. Boston: McGraw-Hill.

Willeke, K. (1976). "Temperature dependence of particle slip in a gaseous medium." Journal of Aerosol Science **7**: 7.

Wood, N. B. (1981). "A simple method for the calculation of turbulent deposition to smooth and rough surfaces." Journal of Aerosol Science **12**(3): 16.

Yao, J., M. Fairweather and Y. L. Zhao (2014). "Numerical Simulation of Particle Deposition in Turbulent Duct Flows." Industrial & Engineering Chemistry Research **53**: 13.

Zhang, H. and G. Ahmadi (2000). "Aerosol particle transport and deposition in vertical and horizontal turbulent duct flows." Journal of Fluid Mechanics **406**: 26.

Zhang, J. and A. Li (2008). "CFD simulation of particle deposition in a horizontal turbulent duct flow." Chemical Engineering Research and Design **86**(1): 12.

Zhang, Z. and Q. Chen (2004). "Numerical analysis of particle behaviors in indoor air using Lagrangian method." Roomvent Proceedings 2004, Coimbra, Portugal.

Zhang, Z. and Q. Chen (2007). "Comparison of the Eulerian and Lagrangian methods for predicting particle transport in enclosed spaces." Atmospheric Environment **41**(25): 13.

Zhao, B., C. Chen and Z. Tan (2009). "Modelling of ultrafine particle dispersion in indoor environments with an improved drift flux model." Aerosol Science **40**(1): 15.

Zhao, B., Y. Zhang, X. Lia, X. Yanga and D. Huangb (2004). "Comparison of indoor aerosol particle concentration and deposition in different ventilated rooms by numerical method." Building and Environment **39**: 8.

Zhao, B., Z. Zhang and X. Li (2005). "Numerical study of the transport of droplets or particles generated by respiratory system indoors." Building and Environment **40**(8): 8.

Zhao, B., Z. Zhang, X. Li and D. Huang (2004). "Comparison of diffusion characteristics of aerosol particles in different ventilated rooms by numerical method." ASHRAE Transactions **110**(1): 8.